



**ΕΘΝΙΚΟ ΚΑΙ ΚΑΠΟΔΙΣΤΡΙΑΚΟ ΠΑΝΕΠΙΣΤΗΜΙΟ ΑΘΗΝΩΝ**

**ΣΧΟΛΗ ΘΕΤΙΚΩΝ ΕΠΙΣΤΗΜΩΝ**

**ΔΙΑΤΜΗΜΑΤΙΚΟ ΠΡΟΓΡΑΜΜΑ ΜΕΤΑΠΤΥΧΙΑΚΩΝ ΣΠΟΥΔΩΝ**

**ΩΚΕΑΝΟΓΡΑΦΙΑΣ ΚΑΙ ΔΙΑΧΕΙΡΙΣΗΣ ΘΑΛΑΣΣΙΟΥ ΠΕΡΙΒΑΛΛΟΝΤΟΣ**

**ΔΙΠΛΩΜΑΤΙΚΗ ΕΡΓΑΣΙΑ**

**First CTD Measurements in the active hydrothermal vent  
field of Kolumbo submarine volcano, NE of Santorini**

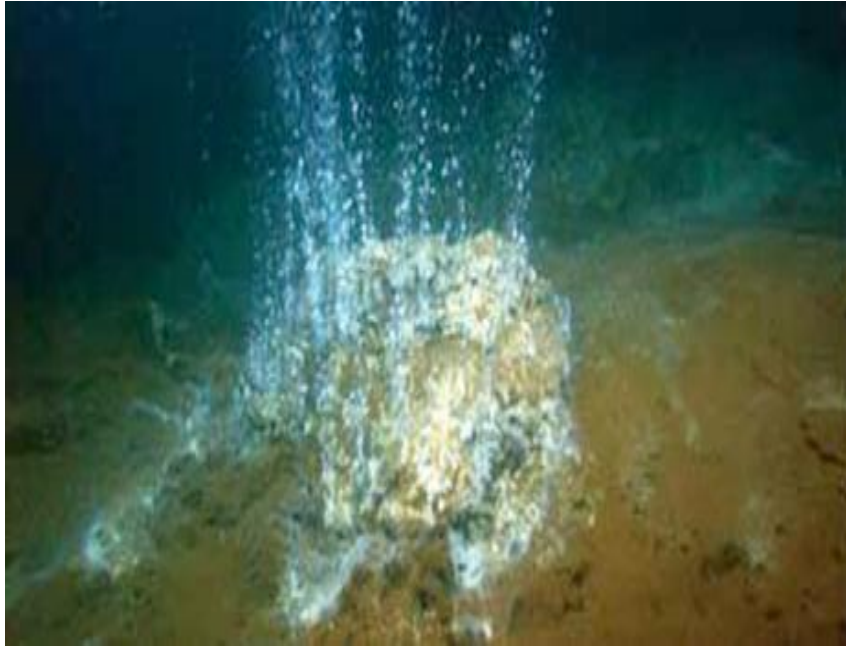
**Χριστοπούλου Μαρία Ελένη**

**ΑΘΗΝΑ**

**ΑΠΡΙΛΙΟΣ 2014**

## **ΔΙΠΛΩΜΑΤΙΚΗ ΕΡΓΑΣΙΑ**

First CTD Measurements in the active hydrothermal vent field of Kolumbo  
submarine volcano, NE of Santorini



**ΧΡΙΣΤΟΠΟΥΛΟΥ ΜΑΡΙΑ ΕΛΕΝΗ**

A.M. 22012

**ΕΠΙΒΛΕΠΩΝ:**

**Δημήτριος Παπανικολάου, Καθηγητής ΕΚΠΑ**

**ΕΞΕΤΑΣΤΙΚΗ ΕΠΙΤΡΟΠΗ:**

**Θεόδωρος Μερτζιμέκης, Επίκουρος καθηγητής ΕΚΠΑ**

**Νομικού Παρασκευή, Λέκτορας ΕΚΠΑ**

10/04/2014

# ACKNOWLEDGEMENTS

I would like to express my gratitude to my supervisor, Professor Dimitris Papanikolaou for the useful comments, remarks and engagement through the learning process of this master thesis. Furthermore I would like to thank Assistant Professor Theo Mertzimekis for his support and for his useful comments and suggestions throughout the process and Lecturer Paraskevi Nomikou for the assistance and dedicated involvement over this past year. I would, also, like to thank Prof. Steven Carey and Dr. Kate Croff Bell for giving me the opportunity to engage with this topic.

This work was supported by Institute for Exploration (IFE-USA) and the collaborative projects “New Frontiers in the Ocean Exploration 2010-2011” between the Graduate School of Oceanography at the University of Rhode Island (URI-USA), the Dept. of Geology and Geoenvironment of University of Athens (NKUA-GREECE), and the Institute of Geology and Mineral Exploration (IGME-GREECE). The officers and the crew of the E/V NAUTILUS are gratefully acknowledged for their important and effective contribution to the field work and sampling.

Getting through my dissertation required more than academic support, and I want to express gratefulness to my family who offered their encouragement and love. Special thanks to my friends for supporting me. Nothing would be the same without them.



## Contents

INTRODUCTION.....	1
1.1 HYDROTHERMAL VENT FIELDS.....	1
1.2 CTD MEASUREMENTS ON HYDROTHERMAL VENT FIELDS.....	4
1.3 CTD PARAMETERS.....	8
GEODYNAMIC SETTING.....	14
2.1 THE HELLENIC VOLCANIC ARC.....	14
2.2 THE SANTORINI VOLCANIC FIELD.....	19
KOLUMBO.....	29
3.1 HISTORICAL REFERENCES.....	29
3.2 GEOLOGY-MORPHOLOGY.....	33
3.3 HYDROTHERMAL VENT FIELD.....	45
CTD MEASUREMENTS.....	51
4.1 THE CRUISES.....	51
4.2 METHODOLOGY.....	59
RESULTS.....	65
5.1 NA007 RESULTS.....	66
5.2 NA011 RESULTS.....	95
5.3 NA014 RESULTS.....	98
5.4 CORRELATION MORPHOLOGY-VERTICAL PARAMETERS DISTRIBUTION.....	101
5.6 GENERAL REMARKS.....	103
5.7 IN COMPARISON WITH OTHER HYDROTHERMAL VENT FIELDS.....	105
5.8 FUTURE WORK.....	107
REFERENCES.....	109

## ABBREVIATIONS LIST

C: Conductivity

T: Temperature

S: Salinity

D:Depth

V: Sound Velocity

E/V : Exploration Vessel

R/V : Research Vessel

ROV: Remotely Operated Vehicle

## ABSTRACT

Kolumbo volcano NE of Santorini is a natural laboratory to study both geological processes and the recently discovered active hydrothermal field. The crater floor of Kolumbo volcano has been recently explored by E/V Nautilus (Nomikou et al., 2012a). An extensive hydrothermal vent field was found at the depth of 505 m at the NNE part of the crater floor. Conductivity-Temperature-Depth measurements (see 1.2 below) have been conducted by instruments aboard ROV Hercules. Gas discharges have been found to be 99% rich in CO<sub>2</sub> (Carey et al., 2013a). CTD data can be used to trace anomalies in temperature, salinity, conductivity or sound velocity with the depth. This information can be exploited to extensively map the active hydrothermal vent field. By comparing CTD measurements inside and outside the cone (where no activity is known to exist) potentially different physicochemical characteristics in the water column can be studied. Hydrothermal activity has been exclusively studied in the past by means of visual observation (Sigurdsson et al., 2006). In this thesis the hydrothermal vent activity is mapped by CTD measurements for the first time. In addition, CTD profiles can be correlated with the cone's morphology in terms of physicochemical properties in the water column.

## ΠΕΡΙΛΗΨΗ

Το ηφαίστειο Κολούμπο, ΒΑ της Σαντορίνης είναι ένα φυσικό εργαστήριο για τη μελέτη τόσο των γεωλογικών διεργασιών, όσο και του πρόσφατα ανακαλυφθέντος ενεργού υδροθερμικού πεδίου. Ο βυθός του κρατήρα τού ηφαιστείου Κολούμπο έχει εξερευνηθεί πρόσφατα από το E/V Nautilus (Nomikou et al., 2012a). Εντοπίστηκε εκτενές υδροθερμικό πεδίο σε βάθος 505 μέτρων στο ΒΒΑ τμήμα του βυθού του κρατήρα. Μετρήσεις αγωγιμότητας-θερμοκρασίας-βάθους (βλ. 1.2 παρακάτω) διενεργήθηκαν από όργανα ενσωματωμένα στο ROV Hercules. Βρέθηκαν εκλύσεις αερίων πλούσιων σε CO<sub>2</sub> κατά 99% (Carey et al., 2013a). Τα δεδομένα CTD μπορούν να χρησιμοποιηθούν για την ανίχνευση ανωμαλιών στη θερμοκρασία, την αλατότητα, την αγωγιμότητα ή την ταχύτητα του ήχου με το βάθος. Οι πληροφορίες αυτές μπορούν να συνεισφέρουν στην εκτενή χαρτογράφηση του ενεργού υδροθερμικού πεδίου. Συγκρίνοντας τις μετρήσεις CTD εντός κι εκτός του κώνου (όπου δεν έχει παρατηρηθεί δραστηριότητα) είναι δυνατόν να μελετηθούν διάφορα φυσικοχημικά χαρακτηριστικά της στήλης του νερού. Η υδροθερμική δραστηριότητα έχει μελετηθεί αποκλειστικά στο παρελθόν μέσω οπτικών παρατηρήσεων (Sigurdsson et al., 2006). Στην παρούσα διατριβή, η δραστηριότητα του υδροθερμικού πεδίου χαρτογραφήθηκε μέσω μετρήσεων CTD για πρώτη φορά. Επιπροσθέτως, οι κατακόρυφες κατανομές CTD συσχετίζονται με τη μορφολογία του κώνου ως συνάρτηση των φυσικοχημικών ιδιοτήτων στη στήλη του νερού.

# Chapter 1

## INTRODUCTION

### 1.1 HYDROTHERMAL VENT FIELDS

Hydrothermal systems act as a bridge from the earth's mantle to the ocean, cooling the mantle by supplying heat from the earth's interior to the deep ocean, transferring chemical species like metals or gases from the crust to the water column, and, by allocating energy in form of sulfur, methane or hydrogen molecules, the sustain oases of life for a variety of deep-sea chemosynthetic life forms from bacteria to mussels and shrimps (Walter et al., 2010).

More than 300 sites of hydrothermal activity and sea-floor mineralization are known on the ocean floor. About 100 of these are sites of high temperature venting and polymetallic sulfide deposits. They occur at mid-ocean ridges (65%), in back-arc basins (22%), and on submarine volcanic arcs (12%) and on intraplate volcanoes (1%), (Baker & German, 2004; Hannington 2005). Although high-temperature (350 °C) black smoker

vents are the most recognizable features of sea-floor hydrothermal activity, a wide range of different styles of mineralization has been found (Hannington et al., 2005).

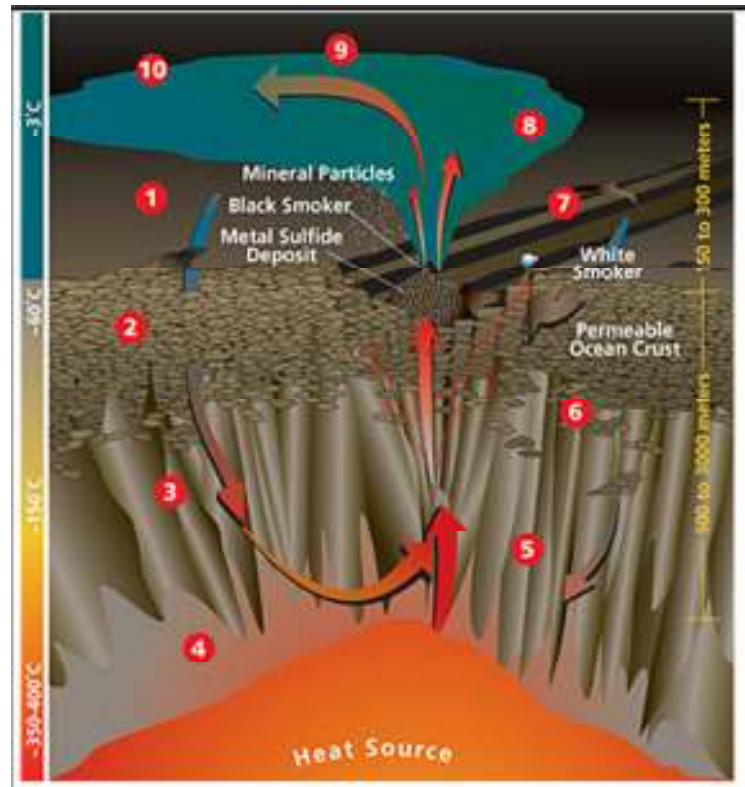


*Fig. 1.1 Hydrothermal circulation (courtesy of Woods Hole Oceanographic Institution)*

Sea floor hydrothermal venting is one of the oldest and most important ore-forming processes on Earth and has produced some of the largest and most valuable ore deposits mined to date. Volcanic-associated and sedimentary-exhalative massive sulfide deposits have accounted for more than half of the past global production of zinc and lead, 7% of the copper, 18% of the silver and a significant amount of gold and other byproduct metals (Singer, 1995; Hannington, 2005).

Large-scale, systematic searches for undiscovered vent sites have been organized with increasing frequency since early 1990s (Baker et al., 1995; German et al., 1995; Baker & German 2004) and now span the global range of spreading rates. The practical difficulty of comprehensively imaging vent fields means that the most efficient searches rely on inferring their presence from water column observations, a technique that

carries varying levels of uncertainty. The enrichment of hydrothermal fluids in several key chemical tracers (e.g. Mn, Fe, CH<sub>4</sub>, H<sub>2</sub>, <sup>3</sup>He) relative to deep ocean waters offers an unambiguous method for detecting hydrothermal discharge even kilometers away from seafloor vent sites (Baker & German, 2004).

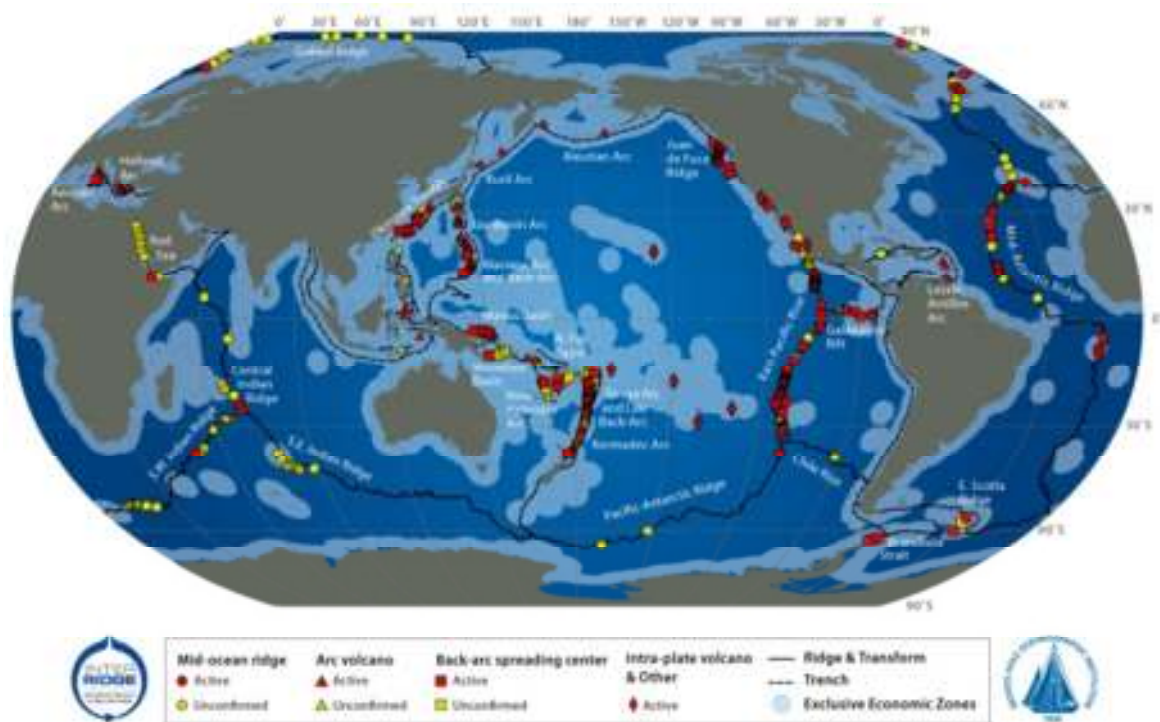


Fig. 1.2 Global distribution of hydrothermal vent field (courtesy of Woods Hole Oceanographic Institution).

Almost all sea-floor hydrothermal activity occurs at the plate margins, where a strong spatial and temporal correlation exists between magmatism, seismicity and high-temperature venting (Hannington et al., 2005). Confirmed vent sites range from isolated patches of low-temperature diffuse flow to enormous sulfide constructs hosting multiple high-temperature chimneys. Vent sites inferred from plume observations range from plumes unequivocally identified as hydrothermal from a combination of optical, hydrographic and diagnostic chemical measurements, to minor optical anomalies that may ultimately prove unrelated to hydrothermal discharge (Baker & German, 2004).

## 1.2 CTD MEASUREMENTS ON HYDROTHERMAL VENT FIELDS

CTD is the abbreviated name for an instrument package that includes sensors for measuring the Conductivity, Temperature and Depth of seawater. The instrument is usually mounted within a frame, which also holds several bottles for sampling seawater but also physicochemical parameters such as O<sub>2</sub> level and sound velocity along with a mechanism (usually called a “rosette” or “carousel”) that allows scientists on board the ship to control when individual bottles are closed (Fig 1.3). The CTD is connected to the ship by means of a conducting cable and data are sent electronically through this cable, in real-time, to the scientists on the ship. The scientists closely monitor the data, looking for temperature and particle anomalies that identify hydrothermal plumes (NOAA, 2014).

CTDs can provide vertical profiles of chemical and physical parameters through the entire water column. A CTD device’s primary task is to record conductivity and temperature changes relative to depth. Conductivity is a measure of how well a solution conducts electricity. Conductivity is directly related to salinity, which is the concentration of salt and other inorganic compounds in seawater (Millero, 1996). Salinity is one of the most basic measurements can be used to determine seawater density which is a primary driving force for major ocean currents (Stewart, 2008).

Ocean explorers often use CTD measurements to detect evidence of volcanoes, hydrothermal fields and other deep-sea features that cause changes to the physical and chemical properties of seawater. Sudden changes, or “anomalies”, in one or more of the properties being measured may be signs of an unusual occurrence, such as an active hydrothermal field (NOAA, 2014).



*Fig. 1.3 A CTD rosette is lowered into the water to measure the salinity, temperature, depth and concentration of particles in the water column (courtesy of NOAA Okeanos Explorer Program, INDEX-SATAL 2010).*

One standard oceanographic sampling technique is the *vertical CTD cast*. First, a location of interest is selected. The ship then travels to that position and stay as close to the same spot as possible (depending on the weather and the ship's basic capabilities) as the CTD package is lowered through the water, usually to within a few meters of the bottom, then raised back to the ship. The ship can then move to a different position and repeat the process (NOAA, 2014).

Hydrothermal plumes are typically located a few hundred meters above the ocean bottom, which over most of the world mid ocean ridge system averages 3000 meters deep. Therefore, much of the water overlying the hydrothermal vent fields is of little interest to the plume-hunting scientists. By lowering the CTD package near the bottom, then moving the ship while cycling the package up and down only through the bottom few hundred meters, a far greater density of data can be obtained. This technique was dubbed a CTD tow-yo and has proven to be an efficient and effective method for mapping and sampling hydrothermal plumes (NOAA, 2014).

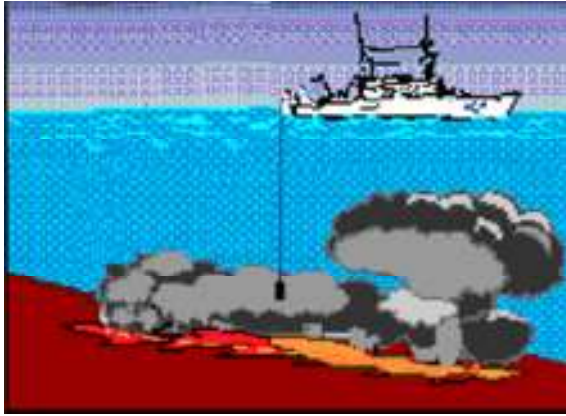


*Fig. 1.4 Vertical CTD cast (yo-yo)*

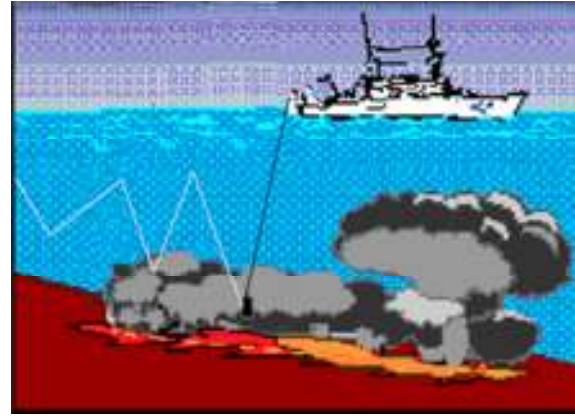


*Fig. 1.5 CTD "Tow yo"*

CTD measurements on hydrothermal vent fields are of highly importance because it's the most reliable method to identify the activity of it. An alternative method is the visual observation of water column and seafloor by camera, a technique that carries varying levels of uncertainty (Baker & German, 2004). By estimating physical and chemical parameters of these areas, certain conclusions come out such as the activity of the area and the anomalies of the measurements.

Several CTD measurements have been recently carried out in locations with a specific interest and hydrothermal activity such as Kermadec Arc in New Zealand (Baker et al., 2012), Aeolian Arc (Aliani et al., 2010), North Pacific Ocean (Ono et al., 2013), Lakes Nyos and Monoon in Cameroon (Kusakabe et al., 2000). In November 2002, gas bursts occurred at sea in the caldera within the islets eastward of Panarea (Aeolian Islands; Aliani et al., 2010) with degassing of CO<sub>2</sub> lasting several months from a depth of ~14 m. CTD data from summer 2003 and spring 2004 recorded pH anomalies with values as low as 6.3 located on main emissions. In November 2002 maximum sediment temperature in the area was 49 °C while values of seawater were not higher than 17-18 °C. Time series depict the peak of fluid temperatures in 2004 and the trend of increasing temperatures since 2007 contrary to the reduction of gas flow (Aliani et al., 2010). CTD

measurements in 2011 showed that in Enarete volcano at the Aeolian Arc venting fluids existed with temperatures up to 5 °C above ambient water.

CTD measurements have been conducted in Lake Nyos and Monoon in Cameroon as well (Kusakabe et al., 2000, Schmid et al., 2006). Temperature in Lake Nyos decreased significantly with time after the gas explosion suggesting increasing inflow of cold meteoric water into surface layers. More recent profiles indicate that temperature increases gradually at depths 40 and 175 m and rises sharply below 175 m. Temperatures between 80 and 110 m have shown less than a 0.1 °C change, but below 120 m temperature at a given depth has increased with time. The rate of temperature rises, however it appears to have slowed down, especially after 1993 (Kusakabe et al., 2000).

Conductivity in surface water lake Nyos has drastically decreased in recent years. The upper chemocline, characterized by a sharp rise in conductivity has deepened with time and has stabilized at a depth of 44-45 m since November 1993. Another chemocline has developed below 180 m. between the upper and deeper chemocline the conductivity shows very little change. It is noted that the maximum conductivity recorded in 1988 in the deepest water (below 200 m) has steadily decreased in recent years. Continuous pH profiles were obtained only after November 1993 and are the same since then. The pH values decrease significantly from high surface values (pH>8) to a pH 5.4 at a depth of 45 m, where is the upper chemocline located. Below this chemocline the pH values decrease sharply to pH 5.2 to a depth of 180 m. Under this depth the values show a peculiar pattern; sharp decrease to minimum values close to pH 5.0 at depths between 190 and 200, followed by a sharp rise toward the bottom to pH > 5.2. The minimum of pH is likely caused by the intrusion of warm CO<sub>2</sub> rich water in the lake water and the sharp rise toward the lake water-sediment interface may be explained by mixing of low pH bottom water with relatively high pH pore water in contact with sediments rich in clay minerals (Kusakabe et al., 2000).

Temperature and conductivity profiles of Lake Monoon are basically similar to those at Lake Nyos suggested by measurements taken in 1995 and 1996. There is an upper chemocline at 15–28 m, a gradual increase at mid-depth down to ca. 60 m, minimal increase in deep water (60–95 m) and a sharp increase toward the bottom (>95 m), forming the deeper chemocline. The conductivity in Monoon is significantly

greater than in Nyos due to the abundance of  $\text{Fe}^{+2}$ . The pH values are generally greater than those at Lake Nyos. They decrease to a depth of 60 m and stay constant down to 95 m with a slight increase toward the bottom (Kusakabe et al., 2000).

### 1.3 CTD PARAMETERS

Heat fluxes, evaporation, rain, river inflow, and freezing and melting of sea ice all influence the distribution of temperature and salinity at the ocean's surface. Changes in temperature and salinity can have an impact on the density of water at the surface, which can lead to convection. If water from the surface sinks into the deeper ocean, it retains a distinctive relationship between temperature and salinity which helps oceanographers track the movement of deep water. In addition, temperature, salinity, and pressure are used to calculate density. The distribution of density inside the ocean is directly related to the distribution of horizontal pressure gradients and ocean currents. For all these reasons, we need to know the distribution of temperature, salinity, and density in the ocean.

#### *1.3.1 SALINITY*

At the simplest level, salinity is the total amount of dissolved material in grams in one kilogram of sea water (Stewart, 2008). Thus salinity is a dimensionless quantity. The variability of dissolved salt is very small, and one must be very careful to define salinity in ways that are accurate and practical. Notice that the range of salinity for most of the ocean's water is from 34.60 to 34.80 parts per thousand [o/oo], which is 200 parts per million (ppm). The variability in the deep North Pacific is even smaller, about 20 ppm. If one wants to classify water with different salinity, definitions and instruments accurate to about one part per million are required. A simple definition of salinity is that the "Total amount of dissolved material in grams in one kilogram of sea water" (Stewart, 2008). This is not useful because the dissolved material is almost impossible to measure in practice. For example, materials like gases can't be measured nor can seawater be evaporated to dryness due to loss of chlorides in the last stages of drying (Sverdrup, Johnson, and Fleming, 1942; Stewart, 2008).

To avoid these difficulties, the International Council for the Exploration of the Sea set up a commission in 1889, which recommended that salinity be defined as the “Total amount of solid materials in grams dissolved in one kilogram of sea water when all the carbonate has been converted to oxide, the bromine and iodine replaced by chlorine and all organic matter completely oxidized.” The definition was published in 1902 (Stewart, 2008). This is useful but difficult to use routinely.

Initially, salinity was measured based on Chlorinity, but at the same time oceanographers had begun using conductivity meters to measure salinity. The meters were very precise and relatively easy to use compared with the chemical techniques used to measure chlorinity. As a result, the Joint Panel in 1966 recommended that salinity be related to conductivity of sea water using:

$$S = -0.08996 + 28.29729 R_{15} + 12.80832 R_{15}^2 - 10.67869 R_{15}^3 + 5.98624 R_{15}^4 - 1.32311 R_{15}^5 \quad (1a)$$

$$R_{15} = C(S, 15, 0) / C(35, 15, 0) \quad (1b)$$

where  $C(S, 15, 0)$  is the conductivity of the sea-water sample at 15 °C and atmospheric pressure, having a salinity  $S$  derived from (2a, 2b), and  $C(35, 15, 0)$  is the conductivity of standard “Copenhagen” sea water, an artificial seawater manufactured to serve as a world standard (Millero, 1996). Millero (Millero, 1996) points out that salinity based on chlorinity is not a new definition of salinity, it merely gives chlorinity as a function of conductivity of seawater relative to standard seawater.

By the early 1970s, accurate conductivity meters could be deployed from ships to measure conductivity at depth. The need to re-evaluate the salinity scale led the Joint Panel to recommend in 1981 (JPOTS, 1981; Lewis, 1980) that salinity be defined using only conductivity, breaking the link with chlorinity. All water samples with the same conductivity ratio have the same salinity even though their chlorinity may differ.

The Practical Salinity Scale of 1978 is now the official definition:

$$S = 0.0080 - 0.1692 K_{15}^{1/2} + 25.3851 K_{15} + 14.0941 K_{15}^{3/2} - 7.0261 K_{15}^2 + 2.7081 K_{15}^{5/2} \quad (2a)$$

$$K_{15} = C(S, 15, 0) / C(KCl, 15, 0) \quad (2b)$$

$$2 \leq S \leq 42$$

where  $C(S, 15, 0)$  is the conductivity of the sea-water sample at a temperature of 14.996 °C on the International Temperature Scale of 1990 (ITS-90) and standard atmospheric pressure of 101325 Pa.  $C(KCl, 15, 0)$  is the conductivity of the standard potassium chloride (KCl) solution at a temperature of 15 °C and standard atmospheric pressure. The standard KCl solution contains a mass of 32.435 6 grams of KCl in a mass of 1.000 000 kg of solution. Millero (Millero, 1996) and Lewis (Lewis, 1980) gives equations for calculating salinity at other pressures and temperatures.

The various definitions of salinity work well because the ratios of the various ions in sea water are nearly independent of salinity and location in the ocean. Only very fresh waters, such as are found in estuaries, have significantly different ratios. The result is based on Dittmar’s (Dittmar, 1884) chemical analysis of 77 samples of sea water collected by the Challenger Expedition and further studies by Carritt and Carpenter (Carritt & Carpenter, 1959).

The importance of this result cannot be over emphasized, as upon it depends the validity of the [chlorinity:salinity:density] relationships and, hence, the accuracy of all conclusions based on the distribution of density where the latter is determined by chemical or indirect physical methods, such as the electrical conductivity (Sverdrup, Johnson, Fleming, 1942).

The relationship between conductivity-salinity has an accuracy of around  $\pm 0.003$  in salinity. The very small error is caused by variations in constituents such as  $SiO_2$  which cause small changes in density, but no change in conductivity.

<b>Ion</b>	<b>Atoms</b>
55.3% Chlorine	55.3% Chlorine
30.8% Sodium	30.8% Sodium
7.7% Sulfate	3.7% Sulfate
3.7% Magnesium	2.6% Sulfur
1.2% Calcium	1.2% Calcium
1.1% Potassium	1.1% Potassium

*Table 1: Major constituents of Sea water (Stewart, 2008)*

The Practical Salinity Scale of 1978 introduced several minor problems. It led to confusion about units and to the use of “practical salinity units” [PSU] that are not part of the definition of Practical Salinity. In addition, absolute salinity differs from salinity by about 0.5%. And the composition of seawater differs slightly from place to place in

the ocean, leading to small errors in measuring salinity. To avoid these and other problems, Millero et al (2008) defined a new measure of salinity, the Reference Salinity, which accurately represents the Absolute Salinity of an artificial seawater solution. It is based on a Reference Composition of seawater that is much more accurate than the values in Table 1 above. The Reference Composition of the artificial seawater is defined by a list of solutes and their mole fractions. Using this, Millero et al. (2008) defined artificial Reference Seawater to be seawater having a Reference Composition solute dissolved in pure water as the solvent, and adjusted to its thermodynamic equilibrium state. Finally, the Reference Salinity of Reference Seawater was defined to be exactly  $35.16504 \text{ g kg}^{-1}$  (Stewart, 2008).

With the above definitions, and many additional details described in their paper, Millero et al (2008) show Reference Salinity, SR, is related to Practical Salinity, S, by:

$$SR \approx (35.16504/35) \text{ g kg}^{-1} \times S \quad (3)$$

The equation is exact at  $S = 35$ . Reference Salinity is approximately 0.47% larger than Practical Salinity. Reference Salinity SR is intended to be used as an SI-based extension of Practical Salinity.

### 1.3.2 TEMPERATURE

The distribution of temperature at the sea surface tends to be zonal, that is, it is independent of longitude (Fig. 1.4, 1.5). Warmest water is near the equator, coldest water is near the poles. The deviations from zonal are small. Equator-ward of  $40^\circ$ , cooler waters tend to be on the eastern side of the basin. North of this latitude, cooler waters tend to be on the western side (Stewart, 2008).

The anomalies of sea-surface temperature, the deviation from a long term average, are small, less than  $1.5^\circ\text{C}$ , (Harrison & Larkin, 1998) except in the equatorial Pacific where the deviations can be  $3^\circ\text{C}$ . The annual range of surface temperature is highest at mid-latitudes, especially on the western side of the ocean. In the west, cold air blows off the continents in winter and cools the ocean. The cooling dominates the heat budget. In the tropics the temperature range is less than  $2^\circ\text{C}$ .

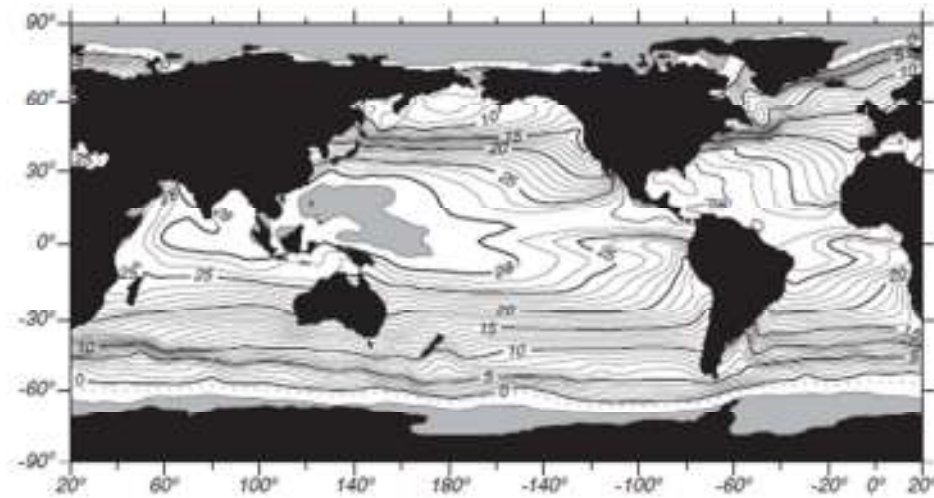


Fig. 1.6 Mean sea-surface temperature for July calculated from the optimal interpolation technique (Reynolds & Smith, 1995) using ship records and AVHRR measurements of temperature. Contour interval is 1 °C with heavy contours every 5 °C. Shaded areas exceed 29 °C (Stewart, 2008)

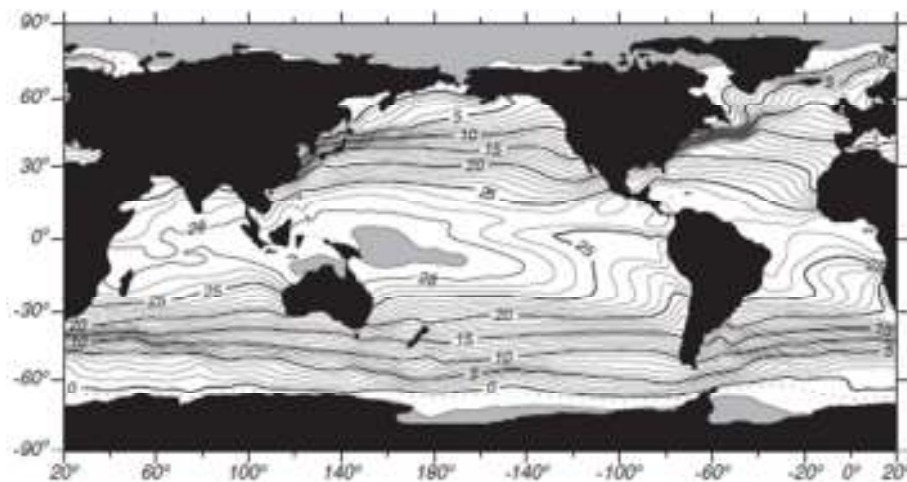


Fig. 1.7 Mean sea-surface temperature for January calculated from the optimal interpolation technique (Reynolds & Smith, 1995) using ship records and AVHRR measurements of temperature. Contour interval is 1 °C with heavy contours every 5 °C. Shaded areas exceed 29 °C (Stewart, 2008)

### 1.3.3 SOUND VELOCITY

Sound provides the only convenient means for transmitting information over great distances in the ocean (Stewart, 2008). Sound is used to measure the properties of the

sea floor, the depth of the ocean, temperature and currents. Whales and other ocean animals use sound to navigate, communicate over great distances, and find food.

The sound speed in the ocean varies with temperature, salinity, and pressure (MacKenzie, 1981; Munk et al., 1995):

$$C = 1448.96 + 4.591 t - 0.05304 t^2 + 0.0002374 t^3 + 0.0160 Z \\ + (1.340 - 0.01025 t)(S - 35) + 1.675 \times 10^{-7} Z^2 - 7.139 \times 10^{-13} tZ^3 \quad (4)$$

where C is speed in m/s, t is temperature in Celsius, S is salinity and Z is depth in meters. The equation has an accuracy of about 0.1 m/s (Dushaw et al., 1993; Stewart, 2008). Other sound-speed equations have been widely used, especially an equation proposed by Wilson (Wilson, 1960, Stewart, 2008) which has been widely used by the U.S. Navy.

For typical oceanic conditions, C is usually between 1450 m/s and 1550 m/s. Using the above equation, sensitivity of C to changes of temperature, depth, and salinity can be estimated. The approximate values are: 40 m/s per 10 °C rise of temperature, 16 m/s per 1000 m increase in depth and 1.5 m/s per 1 increase in salinity (Stewart, 2008). Thus the primary causes of variability of sound speed are temperature and depth (pressure). Variations of salinity are too small to have much influence.

## Chapter 2

# GEODYNAMIC SETTING

### 2.1 THE HELLENIC VOLCANIC ARC

The Hellenic Volcanic Arc (HVA: Methana, Milos, Santorini, Nisyros) is a transitional system that exists in convergent settings, where volcanism and hydrothermal activity occur through thinned continental crust (Kilias et al., 2013). The HVA is a young 5 Ma-to-present volcanic arc that has been developed in the pre-Alpine to Quaternary continental crust of the Hellenic Subduction System (HSS) (Papanikolaou 1993; Royden & Papanikolaou, 2011). Its development is a response to the northward subduction of the last remnant of the oceanic crust of the African plate beneath the southern edge of the active margin of the European plate (Le Pichon & Angelier, 1979) (Fig. 2.1).

The HVA is separated from the Hellenic Sedimentary Arc (HSA: Peloponnesus, Crete, Rhodes) by the Cretan basin, a “back-arc” molassic basin, which lies behind the HSA, but in front of the HVA. The Cretan Basin is the result of extension north of Crete, whereas the Hellenic trench and fore arc basin of the HSS south of Crete is dominated by compression (Le Pichon et al., 1979, Papanikolaou 1993) (Fig. 2.2).

The study of the Tertiary volcanic rocks in the Aegean area has shown a southward migration of the volcanism from late Eocene in the North Aegean coastal areas to the present day active volcanoes along the southern margin of the Cycladic platform and the Cretan back-arc basin (Papanikolaou, 1993; Nomikou et al. 2013a). The total migration of the HVA is approximately 400 km within 40 Ma, which corresponds to an average rate of 10 km/Ma (Papanikolaou 1993; Royden & Papanikolaou, 2011) (Fig. 2.3).

The Hellenic Volcanic Arc (HVA) includes main volcanoes both offshore and onshore (Nomikou et al., 2013a), forming four groups: Methana group at the western edge of the volcanic arc in Western Saronikos Gulf, Milos and Santorini groups in the central part and Nisyros Group at the eastern edge near the Minor Asia coast which have been active during late Pleistocene and Holocene. The submarine outcrops comprise lavas, pyroclastics and pumice deposits of various petrological and geochemical types usually similar to those known from the neighboring volcanic islands.

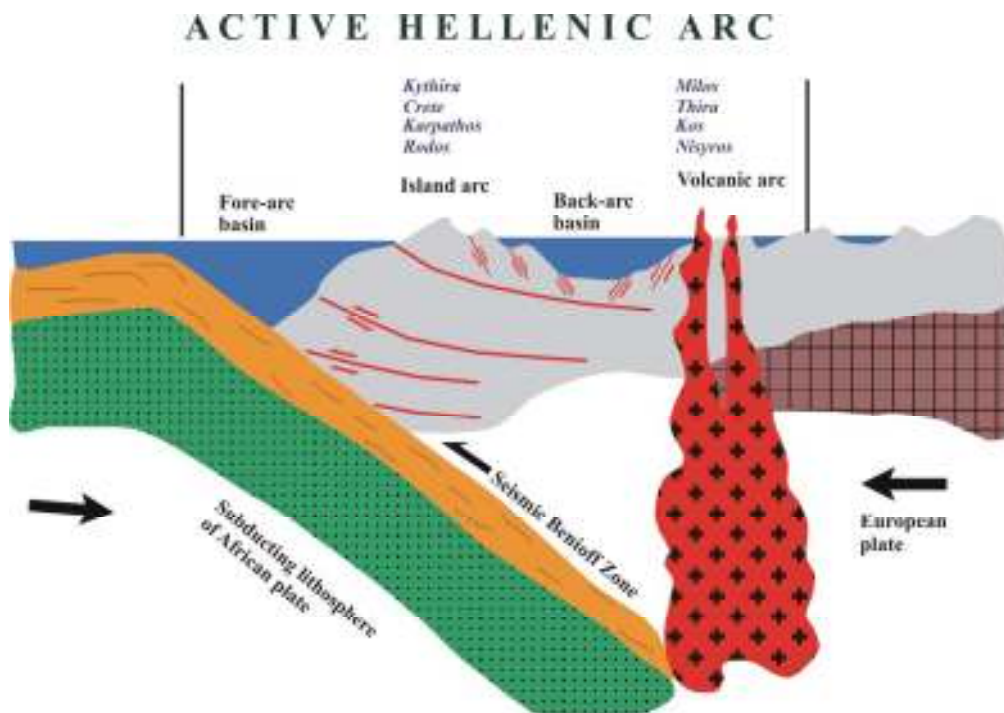


Fig. 2.1 The “Hellenic Subduction System”. The “Hellenic Volcanic Arc”, within active continental margin, developed behind the molassic back-arc basin, hosted over thinned continental crust (Papanikolaou, 1993).

At late 1980s, a systematic reconnaissance of the Aegean sea floor started by the Hellenic Center for Marine Research and the University of Athens, which focused on submarine neotectonic mapping, resulted in the discovery of Paphsanias Volcano in the Western Saronikos Gulf, a few km northwest of Methana volcanic peninsula (Papanikolaou et al., 1988, 1989; Pavlakis et al., 1990; Nomikou et al., 2013a). Soon after, a number of outcrops of volcanic rocks were discovered belonging either to new, previously unknown, submarine volcanoes or to submarine prolongations of volcanic rocks of the Aegean islands in the areas of Nisyros (Papanikolaou et al., 1998; Papanikolaou & Nomikou 2001; Nomikou & Papanikolaou 2010a, 2010b; Nomikou et al., 2013a), Milos (Alexandri et al., 2001; Camilli et al., 2007; Nomikou et al., 2013a) and Santorini (Alexandri et al., 2003; Sigurdsson et al., 2006; Nomikou et al., 2012a; Nomikou et al., 2013a).

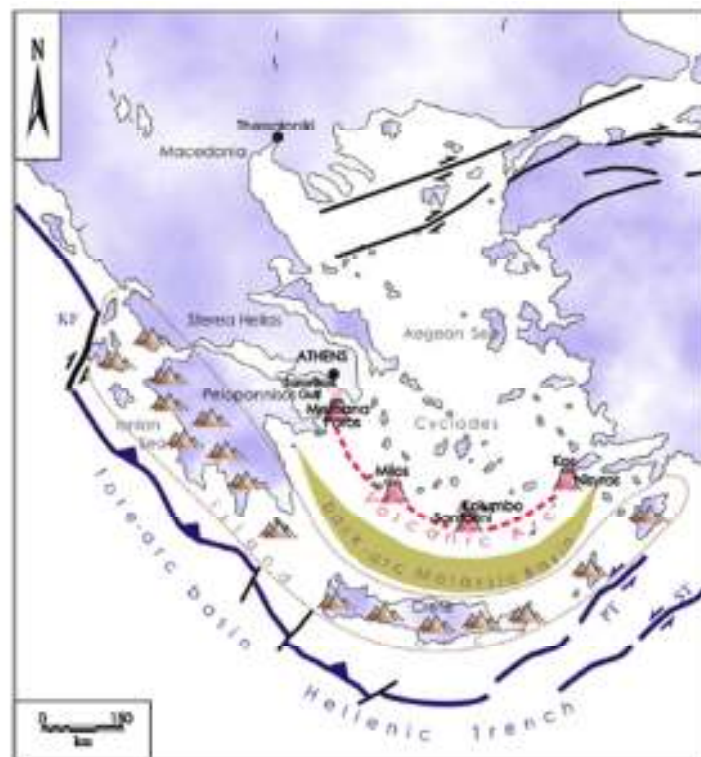


Figure 2.2 The Hellenic Volcanic Arc and the Hellenic Sedimentary Arc separated by the back-arc Molassic basin (Papanikolaou, 1993)

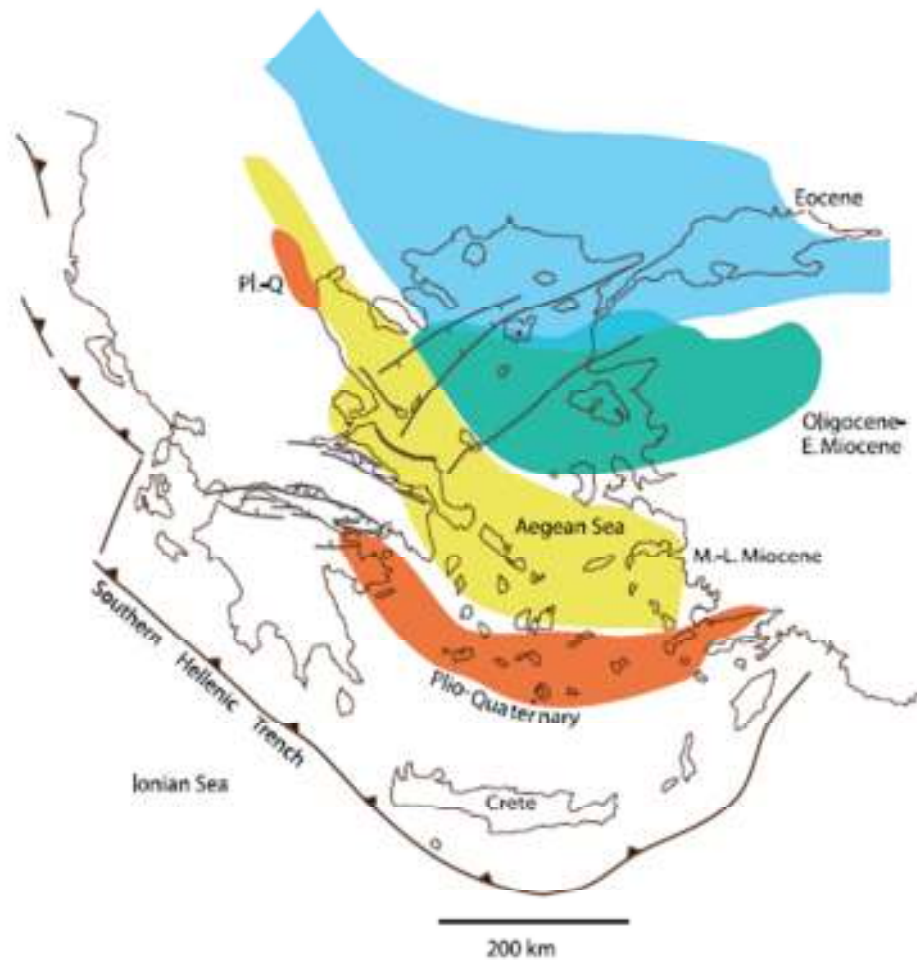


Fig.2.3 Approximate location of the subduction-related Hellenic volcanic arc for the Eocene, Oligocene to early Miocene, middle and late Miocene, and Pliocene Quaternary time periods. The Hellenic trench is indicated by a heavy barbed line, and active normal and strike-slip faults in mainland Greece and the northern Aegean are indicated by black lines with ticks (Royden & Papanikolaou, 2011).

According to Nomikou et al., 2013a, the geometry of each volcanic group is different through time, and so is the volume of the extruded rocks. The Methana group shows a medium activity mainly onshore throughout Late Pliocene–Holocene, with the exception of the Paphsanias volcano occurring offshore. The shift of the volcanic activity from Aegina to Methana within early Pleistocene is remarkable in this case, following the overall outward migration of the volcanic arc. Milos group shows a long lasting activity since Late Pliocene with several different volcanic centers around the onshore outcrops of the islands with a minor recent submarine activity. On the contrary,

Santorini shows a shorter volcanic activity since early Pleistocene with intense Holocene volcanism both onshore and offshore, including the Kolumbo volcanic chain with a well oriented NE-SW structure. Finally, Nisyros is an even younger volcanic group with the highest activity during Late Pleistocene–Holocene, both onshore and offshore, post-dating the previous intense activity throughout Pliocene-Middle Pleistocene of Kos (Papanikolaou, 1993).

The tectonic structure of the volcanic centers is usually a form of neotectonic graben with normal faulting, sometimes overprinted by subvertical strike-slip structures, especially in the Santorini and Nisyros volcanic groups, which form the central and eastern part of the arc. The neotectonic graben structures hosting the volcanic centers have different orientations along the arc with prevailing NW-SE direction in Methana and Milos and NE-SW orientation in Santorini and Nisyros following the general geometry of the Hellenic Arc (Fig. 2.4b). Marine or continental - usually lacustrine- sedimentary deposits are found together with the volcanic rocks in the neotectonic graben structures with deposition of several hundred meters thick Plio-Quaternary volcanosedimentary formations, such as the cases of Milos and Kos (Fytikas, 1977; Nomikou, 2004). In all four volcanic groups the major structure is developed at the southern margin of the Cycladic metamorphic belt towards the more external non metamorphic geotectonic units of the Hellenides. This tectonic boundary runs near the southern border of the Cycladic plateau, parallel to the northern margin of the Cretan back-arc basin (Fig. 2.4a).

The NE-SW strike-slip direction of faults has been proposed in the Santorini and Kolumbo volcanic structures, based on the observed subvertical faults in the offshore Anhydros Basin and the associated system of volcanic dikes (Nomikou et al., 2013). Thus, the overall tectonic regime in the central and eastern part of the arc is better described as transtensional with prevailing NE-SW direction. This trend is very intense in the Santorini volcanic group and less in Nisyros. The other two volcanic groups of Methana and Milos show different orientations that may co-exist and the outcrops of the volcanic formations are more circular and not necessarily aligned in a pronounced direction as for example in Western Saronikos Gulf. The prevailing tectonic trend in Milos group and Methana group is rather in the NW-SE direction, similar to the general direction of the Hellenic arc. However, this tectonic trend is overprinted by E-W normal faults, creating the more recent neotectonic horst and graben structure following the

disruption of the arc parallel structures of the Hellenic arc by the more recent structures of the Central Hellenic shear zone which accommodates the differential motion of the Hellenic arc from the annexed to the European plate northern part of the Hellenides (Papanikolaou & Royden, 2007; Royden & Papanikolaou 2011).

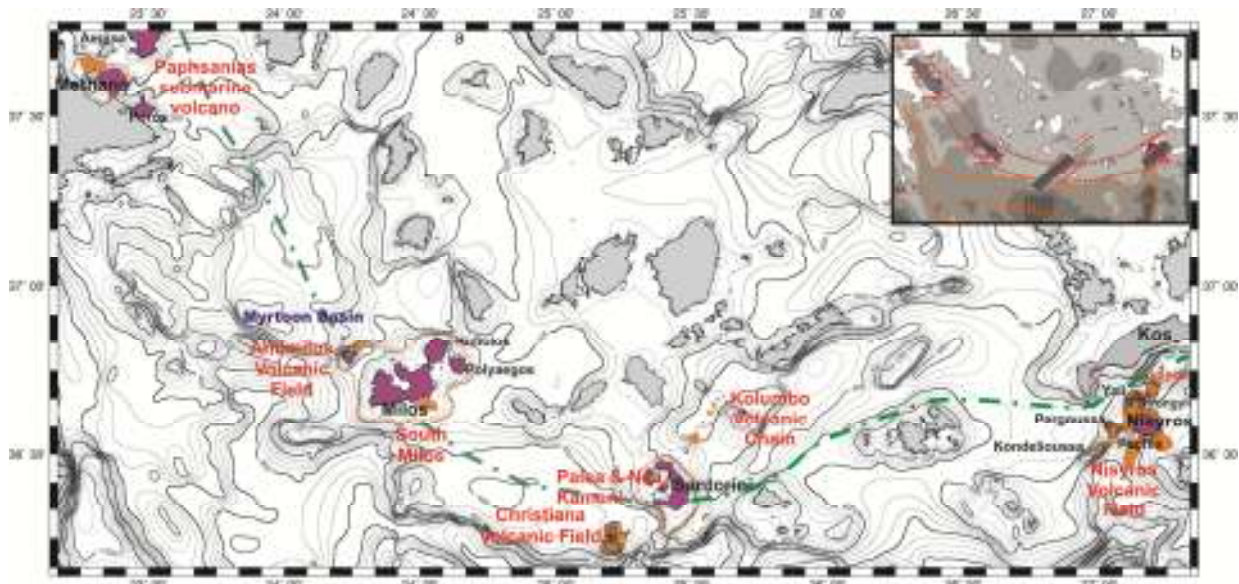


Figure 2.4: General Bathymetric map of Hellenic Volcanic Arc with 50 m contours. The volcanic outcrops of the Aegean volcanic arc both onshore and offshore areas shown on the above maps. The approximate extent of the submarine prolongation of the onshore volcanic outcrops is indicated by dashed lines in those areas where submarine reconnaissance is still in progress. The tectonic boundary of the Cycladic metamorphic belt, north of the volcanic arc is indicated by a green dashed line (Nomikou et al., 2013a)

*Inset map: Tectonic sketch indicating the tectonic trend of the Aegean volcanic outcrops. Dark gray corresponds to the Late Pleistocene–Holocene volcanic outcrops whereas light gray dashed lines correspond to the Late Pliocene–Middle Pleistocene outcrops. Red lines correspond to major normal faults (with ticks) or strike-slip faults (with double arrows) (Nomikou et al., 2013a).*

## 2.2 THE SANTORINI VOLCANIC FIELD

The Santorini Volcanic field is located at the central part of the Hellenic Volcanic Arc and is a large tectonic/volcanic complex that trends generally from the southwest to northeast over a distance of 45 km and includes the islands of Christianna, the island of

Santorini and the Kolumbo volcanic chain in Anhydros basin (Fig. 2.5 Nomikou et al., 2012a).

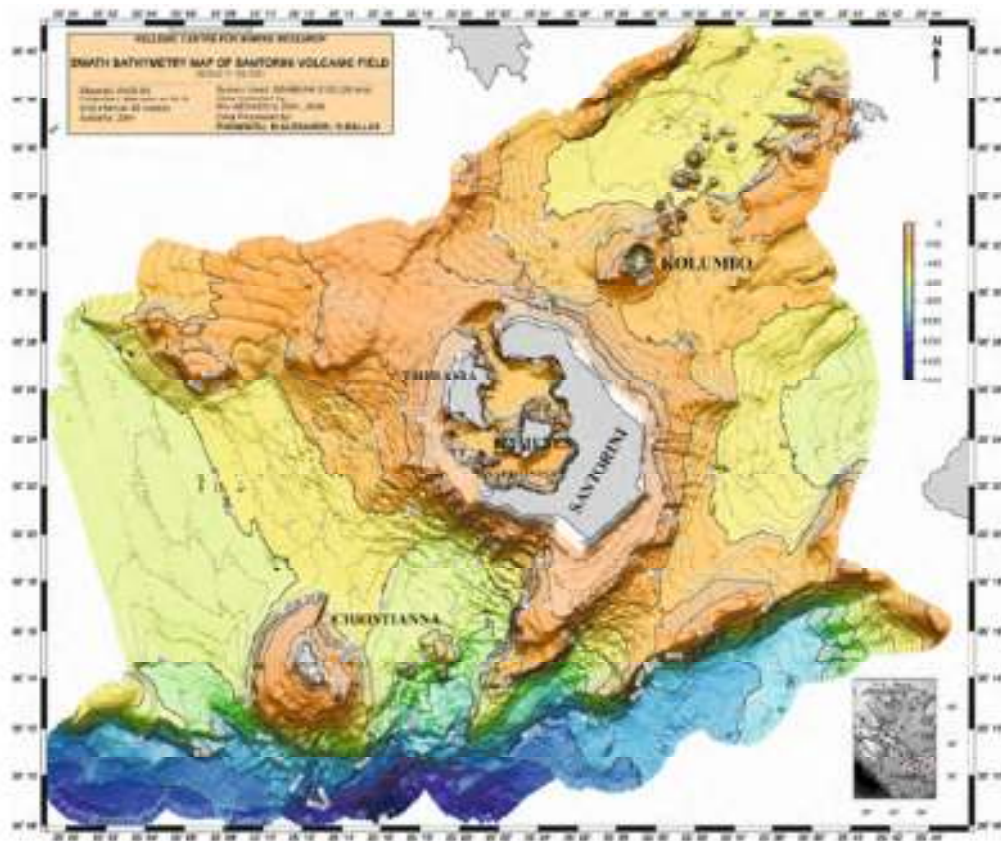


Fig.2.5 Swath bathymetric map of the Santorini Volcanic field (Nomikou et al., 2012a).

### 2.2.1 Christiana

Christiana islands, a group of four small islets, belong to a stand-alone volcanic cone that updomed the sea floor and, as the shape of the bathymetric contours indicates, it produced various flows and pyroclastic deposits. It seems that the whole edifice was built at the junction of a pair of fault zones trending NNW-SSE and NNE-SSW with most prominent the latter one, cutting sharply the volcanic cone and continuing north of the northern island (Fig. 2.6a) (Nomikou et al., 2013a). The dimensions of the Christiana volcanic cone are 10 to 13 km and the four islets constitute the summits of the same cone aligned along the NNW-SSE direction (The maximum elevation of the islands is 283 m). The base of the volcanic cone rises from different depths above the sea bottom with approximately 500 m depth at the northern periphery and much deeper along the

southern part where it exceeds 800 m depth. The total volcanic relief of the Christianna structure is more than 900 m.

Three new volcanic dome structures can be observed east of Christiana islands at 10 km distance with their base at an average depth of 500-600 m. The summit of the three domes is at a depth of 300 m for the larger and 400 m for the two smaller ones. Thus, the volcanic relief is about 300 m for the larger and 200 m for the two smaller domes. No visual observations have been made on the submarine domes, before “Nautilus” Cruise in 2011 (E/V Nautilus, expedition NA014 report, 2012). Several *Hercules* (see Chapter 4 for details) dive transects reconducted up the slopes of the Christiana domes to study their origin, history, and relationship with the rest of the Santorini volcanic complex. Evidence of faulting was found such as dramatic cliffs up to 100 meters tall, and small colonies of yellow, presumably sulfur-reducing hydrothermal bacteria (Fig. 2.6b), as well as abundant benthic megafauna, including sponges, corals, sea cucumbers and urchins (Bell et al., 2012; Nomikou et al., 2013a).

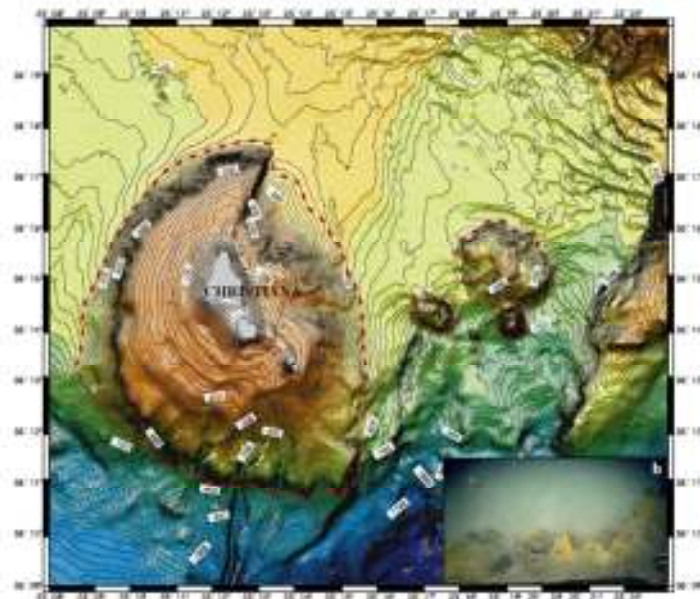


*Fig.2.6a A swath bathymetric map of Christiana volcanic field using 10 m isobaths. The three newly discovered submarine volcanic domes are shown by red dashed lines. b: Small colonies of yellow sulfur hydrothermal bacteria observed at the higher slopes of the larger volcanic dome (Nomikou et al., 2013a)*

### *2.2.2 Santorini Island*

The volcanic island of Santorini (Thera) is located in the southern Aegean Sea and currently represents the most active volcanic field of the Hellenic Volcanic Arc. Its most recent large eruption, the so-called Minoan eruption, occurred 3600 BP and is particularly well known for the significant impact on the Minoan civilization (Druitt, 1989; Friedrich, 2000; Friedrich et al, 2006). The volcanic complex includes the islands of Thera, Therasia, Nea Kameni, Palaia Kameni and Aspronisi, arranged in a circular shape (Fig. 2.7). The largest island, Thera, is semicircular and its concave side is open to the west, while Therasia and Aspronisi lie at the western part of the complex. They all represent the remains of the collapsed volcanic shield and form a ring around a large submarine caldera that was formed around 1600 BC (Pyle 1990; Friedrich, 2000; Nomikou et al., 2013).

Volcanic activity on Santorini started 2 Ma before present with the extrusion of dacite vents on the Akrotiri Peninsula and continued producing different kinds of lavas and pyroclastics (Druitt et al., 1989). The pre-volcanic alpine basement, consisting mainly of late Mesozoic-early Cenozoic schists and marbles, is exposed on Mt. Profitis Ilias (Papastamatiou, 1958; Tataris, 1965), at the southeastern part of the island. At least seven large-volume explosive eruptions and caldera-forming events have taken over the last 600,000 years (Druitt et al., 1989).

The Nea Kameni Island in the center of the caldera forms the summit of the actively growing new volcanic center. The ancient geographer Strabo was the first to record volcanic eruptions inside the Santorini caldera. He described the birth of a newly formed small island in 197 BC in the middle of caldera, which currently corresponds to Palaia Kameni. Several eruptive phases followed the birth of Kameni islands (Palaia and Nea) in the years 46-47, 726, 1570-1573, 1707-1711, 1866-1870, 1925-1928, 1938-1941 and 1950 AD, as the most recent eruption (Pyle and Elliot, 2006).

The maximum diameter of the caldera is nearly 11 km long in a North-South direction (longest axis), while the minimum East-West diameter is approximately 7 km long (short axis) (Fig. 2.8). The caldera walls rise to over 300 m above sea level, while the maximum depth of the caldera seafloor is about 390 m below sea level. The present configuration of the caldera consists of three distinct basins that form separate depositional environments (Nomikou et al., 2013a). The North Basin is the largest and

the deepest (389 m) developed between the Kameni islands, Therasia and the northern part of the Santorini caldera. It is connected by a narrow steep-sided channel with a depth of 300 m to a scallop-shaped ENE-WSW trend that lies outside Santorini caldera, NW of Oia Village (Nomikou et al., 2013a).

The smaller West Basin is encompassed by Aspronisi islet, Palaea Kameni and Southern Therasia with a moderate maximum depth, up to 325 m. The flanks of the basin are gentle in the western part and steepen close to Thirasia and Aspronisi. The South Basin is bounded by the Kameni islands (to the north) and the southern part of the Santorini caldera (to the south). It covers a larger area and is shallower by ~28 m than the western basin. The seafloor morphology suggests that the southern basin has been separated from the western and northern basins by the development of a series of subaerial and submarine volcanic domes, aligned in a NE-SW direction. Apart from the subaerial Kameni islands, the most well-known submarine extrusion is the reef close to Fira Port (referred to here as NK East), which has grown from 300 m b.s.l. up to 40 m b.s.l.

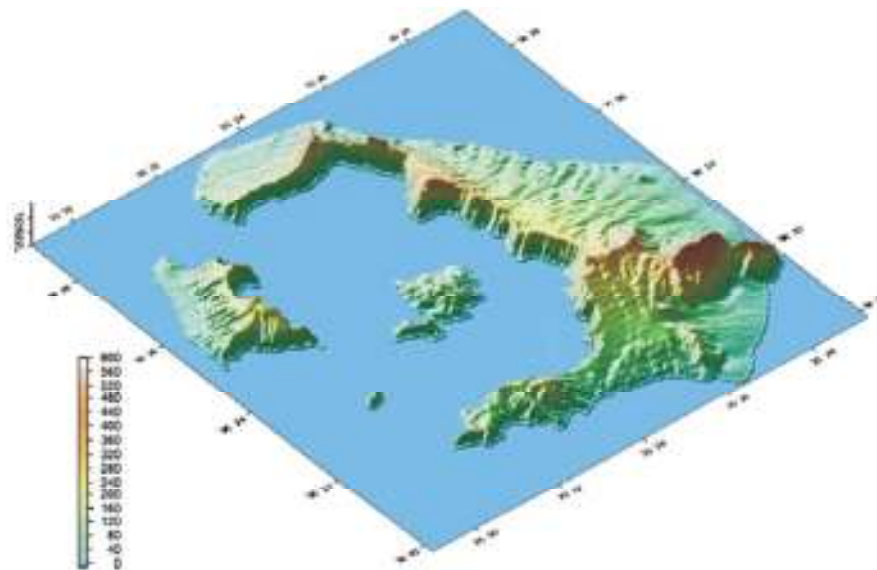


Figure 2.7 3D image of Santorini volcanic field (Nomikou et al., 2012a)

The Kameni islands reach a total relief of almost 470 m in the central part of the Caldera and cover an area of ~ 4×6 km<sup>2</sup>. The submarine structure of the islands to the north and

to the south is very different. The submarine continuation of lava flows can only be observed in the north-eastern part of Nea Kameni, in contrast to the southern part which is characterized by abrupt submarine volcanic cliffs up to 250 m in height (Nomikou et al., 2012a; 2013a).

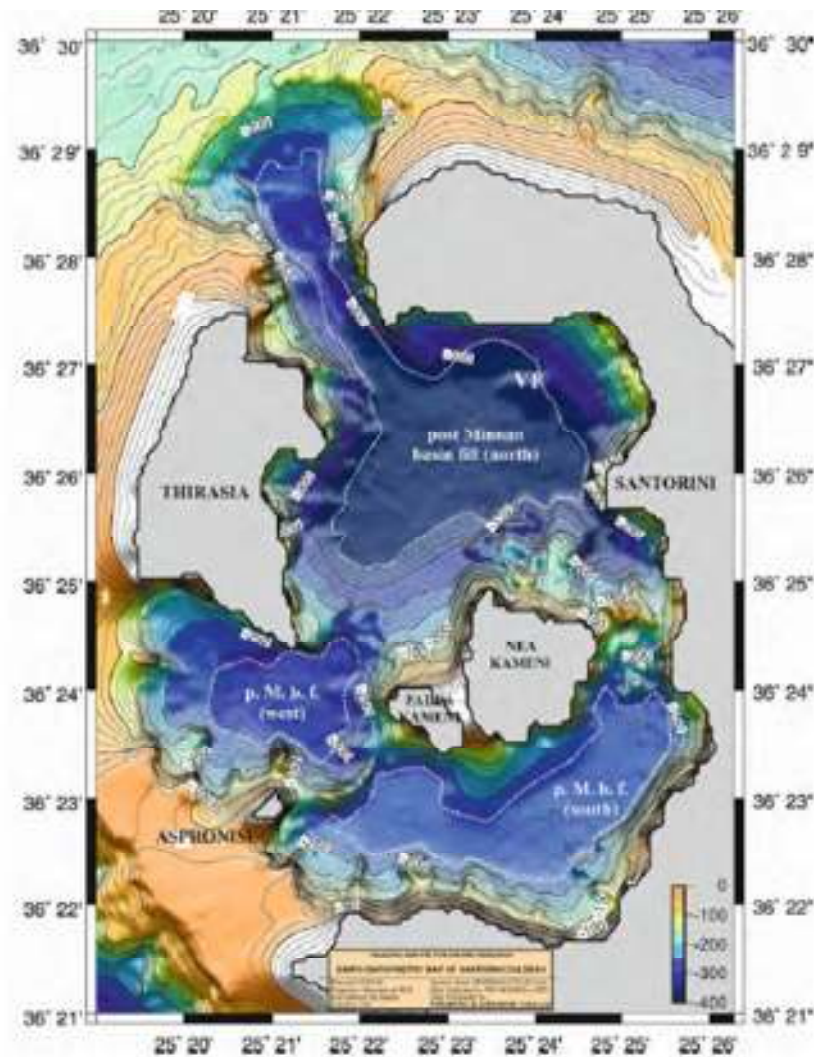


Figure 2.8 Swath bathymetric map of Santorini caldera using 10 m isobaths. Three post- Minoan caldera sub-basins are indicated (bordered with dotted lines with varying depths: 350 m in the north, 280 m in the south and 320 m in the west). VF corresponds to the location of the low temperature vent field discovered in the northern part of the caldera. (Nomikou et al., 2013a).

Hydrothermal vents occur in both the North and South Basin of the caldera (Sigurdsson et al., 2006; Nomikou et al., 2013a). They form a vent field in the NE part of the North Basin that is 200-300 m in extent (Fig. 2.8). The vents form hundreds of 1-to-

4 m diameter mounds covered by a yellowish bacterial mat that are up to 1 meter high. The temperature in these mounds is around 15 to 19 °C or about 5 °C above ambient temperature. The North Basin hydrothermal vent field is located in line with the normal fault system of the Kolumbo rift. Similar vent mounds occur in the South Basin, where most of the low temperature vents are seeps along a ridge separating the West and South Basins. Some more active vents also occur at the shallow depths of the submarine flanks of the Kameni volcanic islands. There is no evidence of high temperature discharges or massive sulphide formation, only low temperature seeps characterized by meter-high mounds of bacteria-rich sediment. Hydrothermalism within the caldera is known to temporally vary in composition and intensity, influenced by tidal and climatic variations (Varnavas and Cronan, 2005, Camilli et al., 2007).

### *2.2.3 Kolumbo Volcanic Chain*

The Kolumbo volcanic field extends 20 km to the northeast of the main island of Santorini, as a linear distribution of over 20 submarine cones of varying sizes (Fig. 2.9). The line of craters lies within a rift in a basined area which is rather flat and featureless with a maximum depth of approximately 450 m. Most of these volcanic cones are circular or concave with abrupt, steep slopes. Some have well-defined craters, whereas others are dome-shaped. The summits of the cones lie between 130 and 370 meters depth with the majority in the depth range 200-350 m. They have been constructed on a seafloor that ranges in depth from 300 to 450 meters (Nomikou et al., 2012a). By far the largest of these submarine craters is Kolumbo, a 3 km diameter cone with a 1500 m wide crater, a crater rim as shallow as 18 m below sea level in the south-west, and a flat crater floor 505 m in depth below sea level. The caldera rim lies in average at a depth of about 150 m forming a submarine circular cliff of about 350 m from the bottom. The volcanic cones to the east of Kolumbo appear to be aligned along two distinct linear trends (29 °NE and 42 °NE) that converge at the point of the crater (Nomikou et al, 2012a; 2013a). Cones in the more northerly trend are generally larger, but vary in size towards the northeast, whereas cones in the more easterly trend are smaller and more uniform in size. In addition, the size and the height of the volcanic domes generally

decrease toward the northeast, indicating that the volcanic activity diminishes as the distance from Kolumbo increases (Nomikou et al, 2012a).

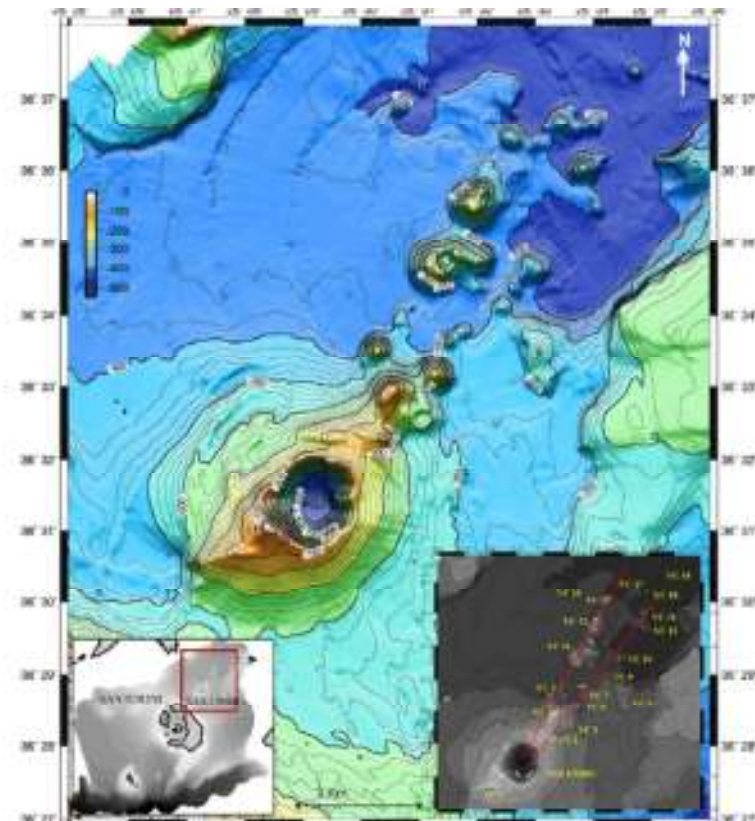


*Fig. 2.9 A swath bathymetric map of the submarine Kolumbo volcanic chain using 10 m isobaths and zoom on the Kolumbo crater (b). VC2-20: number of individual volcanic cones (Nomikou et al., 2012a; 2013a).*

The structure of the Kolumbo submarine volcano is shown on the profile of Fig. 2.10 (Bejelou, 2013). The interpretation of this profile suggests that at least one older volcanic cone exists and is located underneath the present one, indicating that Kolumbo has been active at least once, prior to the 1650 AD eruption (Huebscher et al., 2006). Layered or massive lava flows form the lower part of the present Kolumbo cone and are displayed as stratified, high amplitude, subhorizontal reflectors on the profile. The upper part of the cone shows a transparent acoustic character and is composed of tephra deposits produced during the 1650 eruptive phase. Further on, the volcanic edifice of Kolumbo is clearly shown in this section, with its almost vertical crater walls, as well as the three smaller volcanic domes belonging to the Kolumbo Volcanic Chain.

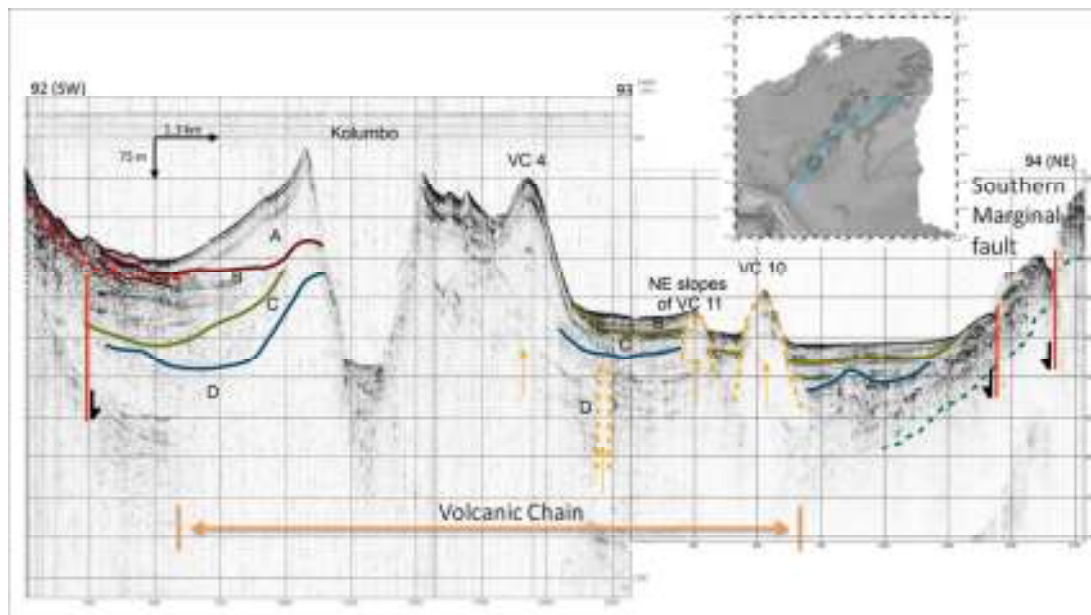
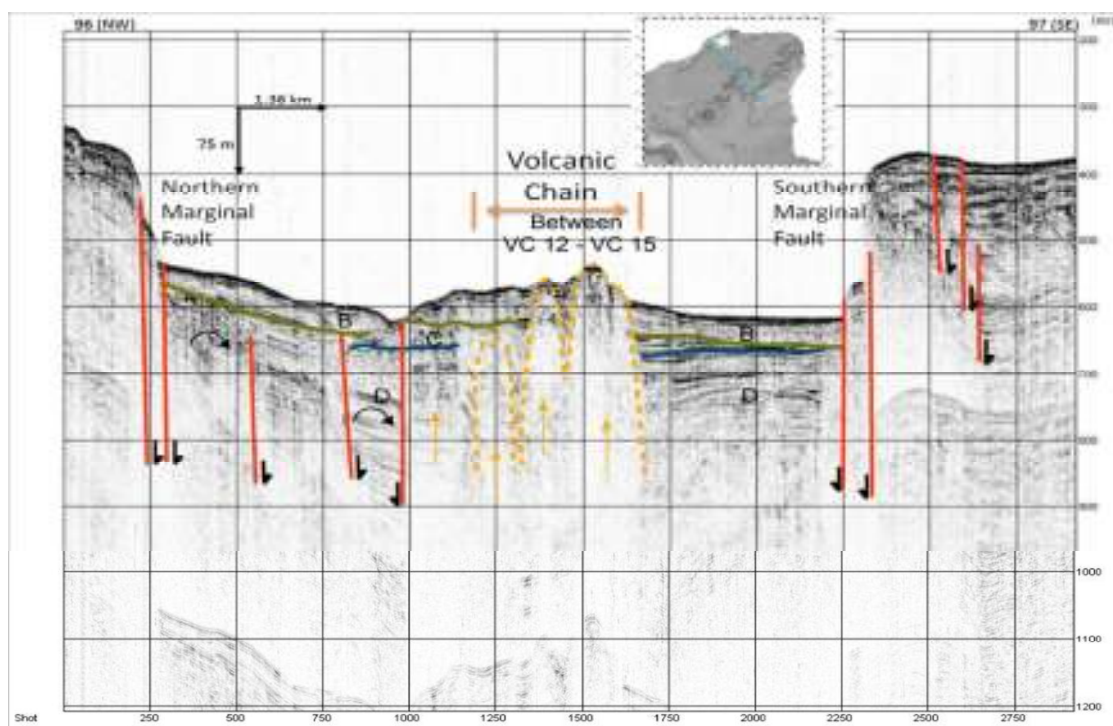


Fig. 2.10: Seismic profile 92-93-94 (Bejelou, 2013).

Integrated evaluation of the swath bathymetry of the Anhydros basin (Sigurdsson et al., 2006; Nomikou et al., 2012a; Nomikou 2013a) and seismic profiling data indicate that the linear distribution of the volcanic cones is controlled by strike-slip faults, which run parallel to the long axis of the basin (Sakellariou et al., 2010; Nomikou 2013a; Bejelou, 2013). This transtensional zone has provided pathways for subduction generated magmas to reach the surface and form at least 20 submarine volcanic centers that are aligned along two principal trends. The southwesterly portions of both trends intersect approximately within the crater of Kolumbo, the largest submarine center within the NE zone. Moving to the northeast the centers diminish significantly in size and are all equal to or less than  $1.0 \text{ km}^3$  in volume. The majority of the cones is dome-shaped and lacks a recognizable summit crater suggesting that the dominant form of eruptive activity involved effusive dome building. However, the presence of some craters and the common occurrence of bedded volcanoclastic deposits indicate that at least part of the submarine activity was explosive. Their small size also suggests that the activity may have been monogenetic in many cases. Geochemical analysis of samples collected on the northeast cones showed evidence of low temperature hydrothermal circulation on the summit and upper flanks in the form of stream-like manganese precipitates emanating from pits and fractures (Nomikou et al., 2012a; 2013a).

The profile of Fig. 2.11 illustrates the characteristic structure of the Anhydros basin. Both margins of the basin are of tectonic origin and are developed along active faults

(Sakellariou et al., 2010) forming a neotectonic graben. Areas of diffuse or transparent acoustic character crosscutting the sedimentary layering of the basin are delineated by dashed lines and indicated by dashed arrows pointing upwards. They are always located below the volcanic domes, while some of them die out before reaching the seafloor. The sedimentary layers are being dragged upwards at their contact to these diapir-like structures. They are interpreted as conduits of the ascending magmatic fluids. They are associated with the existing ruptures, indicating that the latter are zones of crustal weakness which facilitate the magmatic fluid flow (Nomikou et al., 2013a; Bejelou 2013).



*Fig. 2.11 Seismic profile 96-97 interpreted (Bejelou, 2013).*

## **Chapter 3**

### **KOLUMBO**

#### **3.1 HISTORICAL REFERENCES**

Kolumbo submarine volcano erupted explosively in 1650 AD and caused 70 fatalities on the nearby island of Santorini. The accounts of this eruption were collected by Ferdinand A. Fouqué and published in his book, "*Santorini et ses eruptions*" in 1879. This treatise provided the first detailed geological and petrological study of the Santorini volcanic complex and the stratigraphy of the Santorini caldera (Druitt et al., 1999). Fouqué assembled the sequence of events surrounding the eruption (Table 2) from eyewitness accounts of the volcanic activity.

Violent earthquakes occurred across the Santorini archipelago throughout the year leading up to the Kolumbo eruption. In March 1650 droughts and famine followed a series of particularly intense earthquakes. The eruption began in full in September of 1650 with violent seismic activity accompanied by subterranean roaring beginning on the 14th and continuing throughout the month. Primary activity was initiated on the 27<sup>th</sup> when subaerial plumes repeatedly broke the sea surface above the cone. Volcanic gases inundated the archipelago and the volcanic activity formed a small islet just above

the surface. Small earthquakes continued, large quantities of pumice were produced, and plumes formed and dispersed on a roughly hourly cycle throughout the 28th.

September 29, 1650 marked the most violent eruptive activity at Kolumbo. The subaerial plume that formed on the 28th was still visible when incandescent material was observed being ejected from the crater. Father Richard's account notes

*"this was the most terrible day. The earth quivered and the air was afire. Thick sulphurous steam billowed out of the depths. Then suddenly the clouds caught fire, lightning rent the sky, thunder burst forth and strange forms moved before one's eyes: flying snakes shining spears and lances and whirling blazing torches. All that day the clouds hung low and the wild elements met in such raging combat that their clamour could be heard a hundred leagues off" (Fouque 1879, Nomikou et al., 2012b).*

These descriptions captured the spectacular displays of lighting that commonly accompany highly explosive eruptions. Lightning within the plume was accompanied by explosions that were heard as far as 400 km away in the Dardanelles. Intense earthquakes increased in frequency and were felt in Crete while ash fallout from the plume reached Turkey.

Prevailing winds carried fine-grained volcanic ash from the eruptions to the east where it was deposited as a thin, white powdery layer in parts of Turkey. Closer to the volcano, pumice was floating on the sea surface. Pumice can float for several days and travel long distances from the source volcano before its immersion and deposition on the seafloor. Though the activity ceased around 11 pm on the 29<sup>th</sup>, it began again at midnight and continued throughout the 30<sup>th</sup>. After a few days of decreased activity the eruption diminished. One of the main hazardous effects of this volcanic eruption on the local communities was the clouds of poisonous gases that were released. The gas caused eye pain, blindness, and cerebral congestion and many inhabitants temporarily lost consciousness for several hours. There were also reports that the gases discolored coins, sacred vessels in the churches, paintings, and walls in many buildings. This suggests that the gases were both acidic and poisonous as a result of sulphur, chlorine, and carbon dioxide release during the explosive eruptions. Pyroclastic surges which represent one of the most lethal effects of explosive volcanic eruptions are known to be able to travel great distances over water (fig. 3.2). During the night of October 2 the

nine-man crew of a ship passing near Kolumbo were asphyxiated. The crew of a second ship nearby lost consciousness but survived.



*Fig 3.1 Ash and gas plume from a submarine eruption in the Tonga Islands in 2009. Initial stages of the Kolumbo 1650 AD event likely resembled this type of activity (Nomikou et al., 2012b).*

*Fig 3.2 Pyroclastic surge travelling over the sea surface off the east of Montserrat island in the Lesser Antilles (Nomikou et al., 2012b).*

At least one tsunami inundated Thera, carried away livestock, destroyed buildings, and eroded the roadways and 500 acres of the eastern coastline. Two churches in Perissa and Kamari were swept into the sea and the foundation of old churches and ruins were revealed. These newly exposed areas were likely buildings of the Hellenistic Period on the island (e.g. Ancient Oia and Ancient Eleusis). It appears that the initial sign of the oncoming wave was a large retreat of the sea. Dohiaritis (1947) notes that “*Then 20 men went to the beach to gather fish, which were floundering on the exposed bottom of the sea, and they lost their lives. Suddenly earthquakes and solicitations, and thunder have stopped. After that the sea swelled and climbed upon it to the island as two miles. The sea destroyed boats and vineyards and everything.*” The impacts of the tsunamis were observed not only in Santorini, but on many of the neighboring islands as well. It was reported that boats of the Turkish fleet that were tied up along the coast of Dia island (north of Heraklion, Crete), were carried away by the tsunami. Waves that came ashore in Ios reached a level of 50 feet, while in Sikinos they advanced inland up to 350 feet and covered the fields.

A few isolated explosions occurred on November 4<sup>th</sup> and 5<sup>th</sup> with associated gas release and minor earthquakes. After an increase in earthquake intensity and submarine disturbances in the early days of December the 1650 AD eruption of Kolumbo ended. Small shocks and high water temperatures around Kolumbo continued for a number of years but the small island eroded beneath the waves within a few months leaving an 18 m deep cone.

**Table 1. Kolumbo timeline (from Fouque, 1879)**

<b>Date</b>	<b>Activity</b>
1649	Earthquakes
March, 1650	Violent earthquakes, house shaken, rocks split, stones rolled down to the sea Drought and famine
9/14/1650	Violent shocks felt, subterranean roaring
9/27/1650	Uproar reached a climax, houses severely rocking 3 subaerial plumes of dense smoke and flame seen rising 4 mi NE of Santorini Noxious odor spread around Santorini Snow-white ledge emerged from the sea Two columns of smoke rose and quickly disappear Earthquake all day but with less violence Sea covered with pumice
9/28/1650	Explosions with rising plumes in the morning and afternoon blotted out sky Plume persisted until following morning, flames and lightning observed, incandescent rocks ejected
9/29/1650	Dense eruption plume rising to great heights Emergent crater ejecting enormous glowing rocks, loud detonations, lightning Sound heard up to 400 km from Santorini, earthquakes felt on Crete Ash fallout as far as Anatolia and Platia (covered grapes with white blanket) Large rocks ejected to 8 km Tsunami hits Santorini and submerges 500 acres of land, tore down trees and exposed two ancient villages On Ios, sealevel rose 20 m and pumice was deposited Noxious fumes sickening residents, lightning strikes Thera Pumice rafts reach around southern Aegean Roof collapse of 200 houses on Thera
9/30/1650	Explosions resume very early in the morning (just after midnight 9/29) Fumes return with flames and lightning Inhabitants report terrible pain in the eyes, metals quickly tarnished People die of asphyxiation (50 people, >1000 animals)
10/2/1650	Boat recovered with nine inflated bodies, indications of burns
10/4/1650	Intensity of eruptions diminish, some periodic bursts, some small plumes to great height Earthquakes become less violent Great quantities of pumice still came from the volcano
11/4/1650	Dense black cloud rose from the crater, blotting out the sky –20 people lose consciousness
11/5/1650	More "flames" observed Seawater is green and discolored fumes less noticeable, earthquakes imperceptible
12/1/1650	Flames reappeared, earthquakes stronger, sea more restless
12/8/1650	Activity ceases, water becomes clear Island disappears after a few months, leaving an 18 m deep cone

The summary of the 1650 AD submarine eruption of Kolumbo by Fouque contains key observations that are critical to interpreting the eruptive processes of this event. The first is that the activity clearly breached the sea surface and was able to produce subaerial eruption columns of substantial height. Fallout of tephra in western Turkey

suggests eruption column heights in excess of 10 km based on some preliminary modeling were carried out using the PUFF ash-transport model (Searcy et al., 1998). The development of such high eruption columns indicates high mass eruption rates and substantial degassing of primary volatiles in addition to the likely role of phreatomagmatic fragmentation. Second, observations of the extensive development of floating pumice on the sea surface support the existence of a volatile-rich silicic magma. The very rapid disappearance of the island once the activity stopped indicates that the emergent part of the island consisted of easily erodible pyroclastic material. Finally, a certain type of deposits (angular non volcanic clasts) was discovered at St George' s small church near Kamari village, at a distance of 80 m from the shoreline, reinforcing the historical accounts regarding the tsunami (Papadopoulos, 2009). According to Dominey-Howes et al. (2000) all the sites investigated at the eastern coast of Santorini (Kamari, Perissa) show that the tsunami, which accompanied the 1650 AD eruption, probably had a run up of less than 2 m a.s.l. and penetrated less than 500 m from the shore.

### 3.2 GEOLOGY-MORPHOLOGY

Kolumbo is built on the pre-Alpine continental basement of the Cyclades (10-15 km thick) consisting of a core of Carboniferous granites (ortho-gneisses) and a sequence of garnet-mica schists corresponding to the Palaeozoic Metamorphic Basement cropping out on Ios Island (Forster et al., 1999; Kiliyas et al., 2013). Alpine blueschists and overlying nappes comprising both metamorphosed in Late Cretaceous, greenschists, marbles, metaophiolites and metagranites and unmetamorphosed Mesozoic, carbonates and Tertiary flysch are found respectively on top of the pre-Alpine Basement (Fig. 3.3). Kolumbo volcano and the other 19 submarine cones (Nomikou et al., 2012a; Nomikou et al., 2012b Kiliyas et al., 2013) are lying within the Plio-Quaternary marine sediments of the extensional Anhydros basin bordered by marginal fault zones. This linear contribution of the volcanic cones is controlled by the NE-SW Christiana-Santorini-Kolumbo (CSK) volcano-tectonic zone which provides pathways for subduction-generated magmas to reach the surface (Nomikou et al., 2013a; Kiliyas et al., 2013).

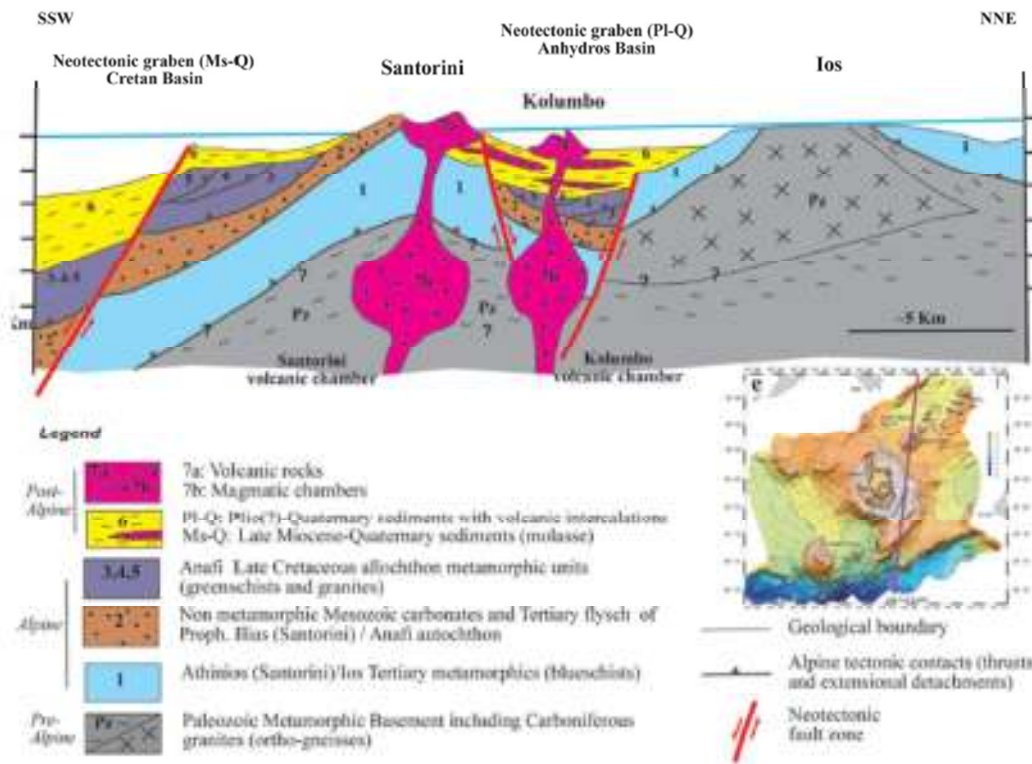


Fig. 3.3 Schematic cartoon depicting the geological cross section through the Hellenic Volcanic Arc, from the molassic back-arc Cretan basin to the Cycladic island of Ios in the back-arc area. (Kiliyas et al., 2013).

Kolumbo is the largest cone in volume and the point where the two different trends of Kolumbo Volcanic Chain converge. Its basal diameter is approximately 3 km and its crater diameter about 1.7 km. The average depth of the crater rim is 150 m, with the shallowest at the depth of 18 m towards the southwestern side of the volcano. The smooth crater floor is at a depth of 500 m (Nomikou, 2003). The highest slope values at the inner crater walls of Kolumbo most likely represent the remnants of the collapse of a relevant volcanic cone. Slope values at the external flanks diminish gradually. On the northwestern flanks, linear to curvilinear areas of abrupt change in slope probably represent an earlier stage of volcanism which created a pre-existing volcanic cone. The volcanic structure of Kolumbo caldera and the minor small, symmetric volcanic cones at the northeastern slope of Kolumbo, are clearly shown in the 3-D stereogram (fig. 3.5).

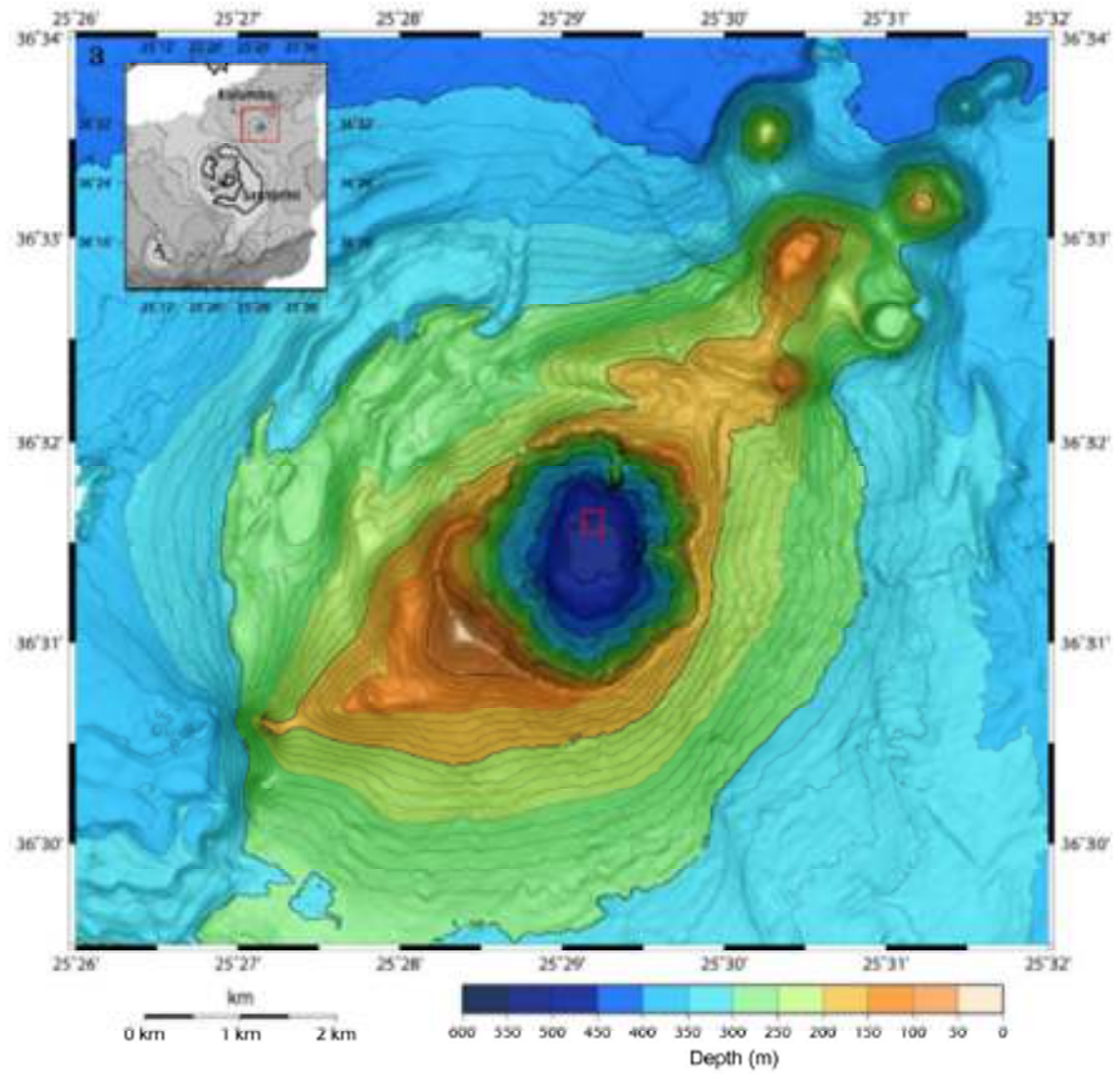
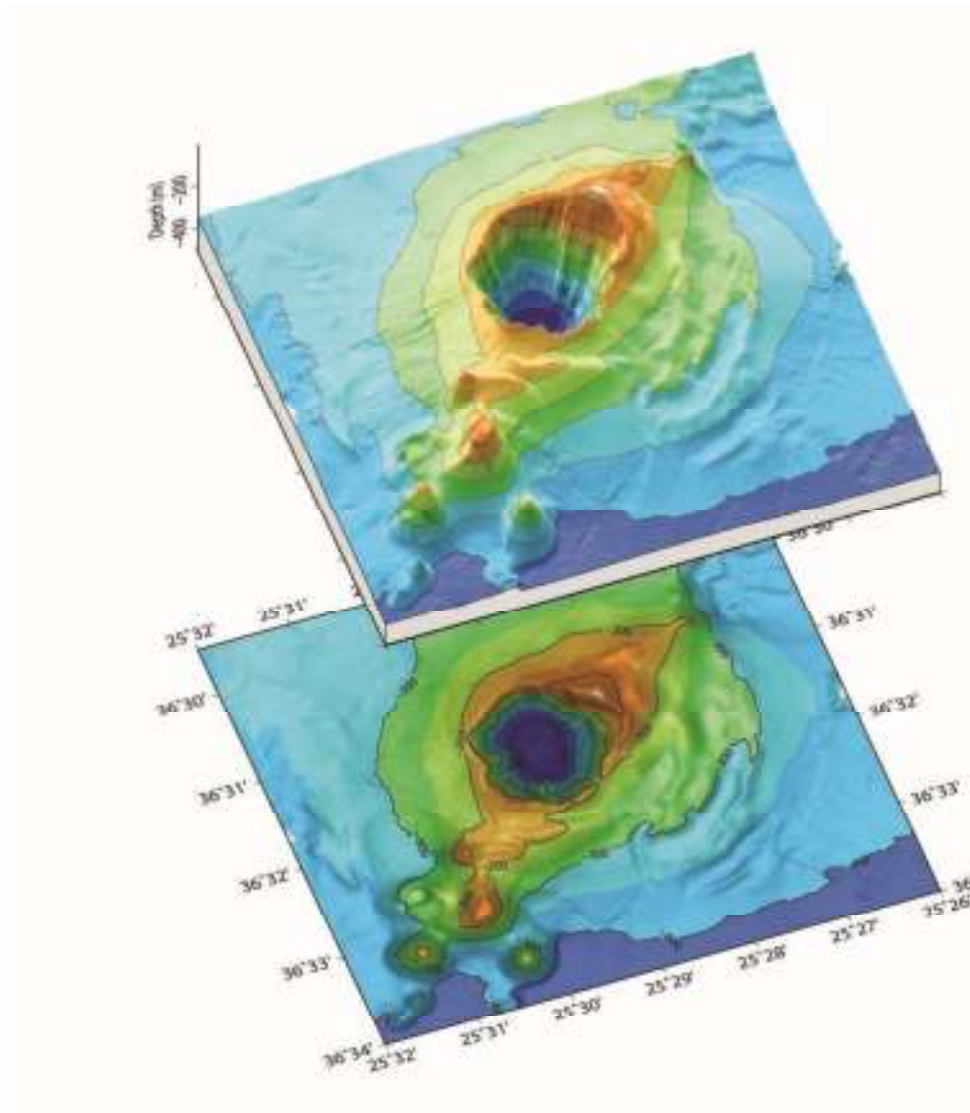


Figure 3.4. Swath bathymetry of Kolumbo volcano (modified after Nomikou 2003)



*Fig. 3.5 3D view of the submarine cone of Kolumbo at depths between 18 and 505 m (Nomikou et al., 2013b).*

The highest slope values (35-50%) are observed within the internal walls of Kolumbo crater and in the external flanks of the closest submarine cones towards NE (Fig. 3.6). Kolumbo's northwestern external slopes gradually diminish from 25-35% to 15-25% and 5-15%, whereas in the southeastern external slopes gradually diminish from 15-25% to 5-15% and 0-5% (Nomikou et al., 2012b).

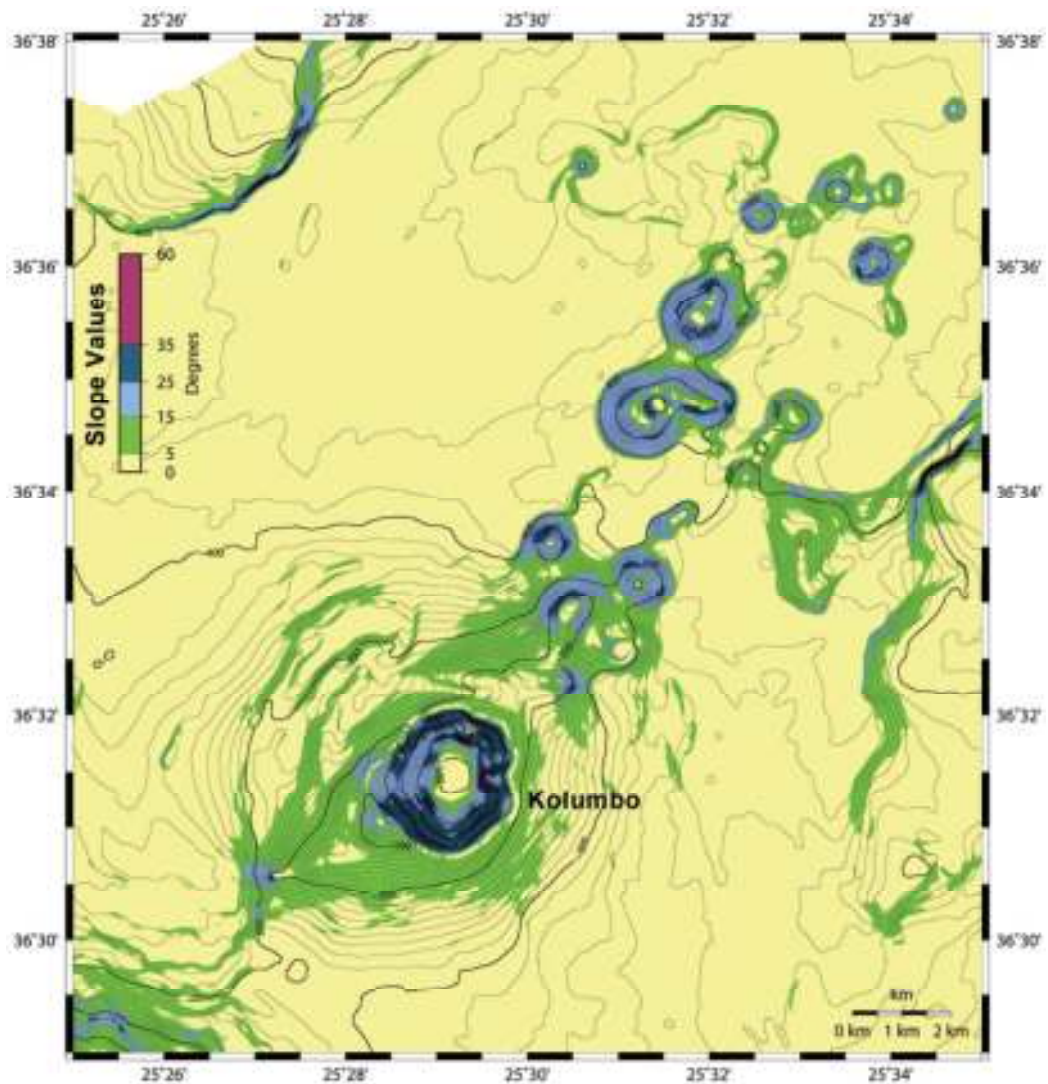


Fig. 3.6. Slope distribution Map of Kolumbo volcano (color scale to the down right of map, Nomikou et al. 2013b).

On the west and northwest flanks are several curvilinear scarps with inward dipping faces and high slope values 25-35%. The orientation of these features suggests that they may represent remnant crater rims and are likely to contain outcrops of volcanic rocks from the earlier stages of cone building. ROV explorations on the flanks of Kolumbo in 2010 (E/V Nautilus, expedition NA007 & NA011 report, 2011) revealed a seafloor irregularly covered by a layer of lapilli size pumice with common outsized boulders of large pumice. This type of distribution is lines up with models for pumice interactions with seawater during explosive submarine eruptions that breach the surface of the sea, as occurred during the 1650 AD Kolumbo event (Fouque, 1879). Large pumices that are ejected above the sea surface can float for significant periods of

time, but eventually become water-logged and sink. Smaller pumices tend to sink rapidly because they become saturated with water much more quickly (Carey, 2000). On the flanks of Kolumbo, extensive deposition of small pumices occurred simultaneously with occasional sinking of much larger pumices (Fig. 3.7).



*Fig. 3.7. Large rhyolite pumices scattered on the seafloor around Kolumbo submarine volcano resulting from the sinking of material from pumice rafts (Nomikou et al., 2013b)*

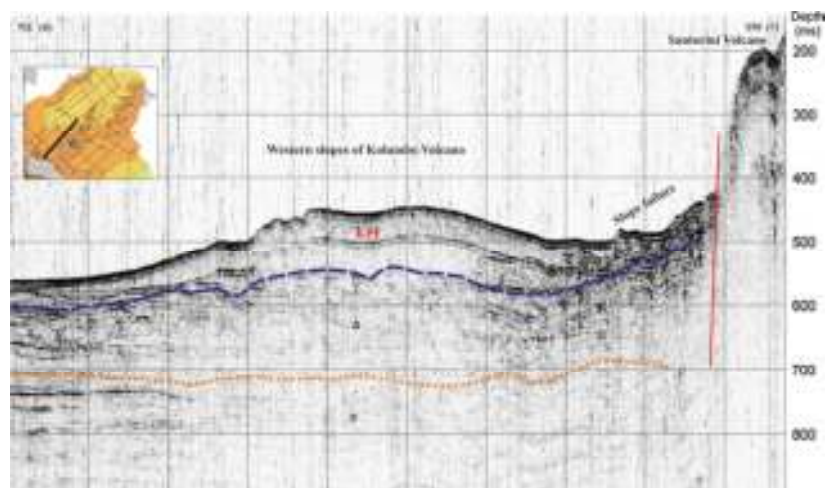


*Fig. 3.8 Seismic reflection profile NE of Santorini. Kolumbo pyroclastic flow deposits (Nomikou et al., 2012b)*

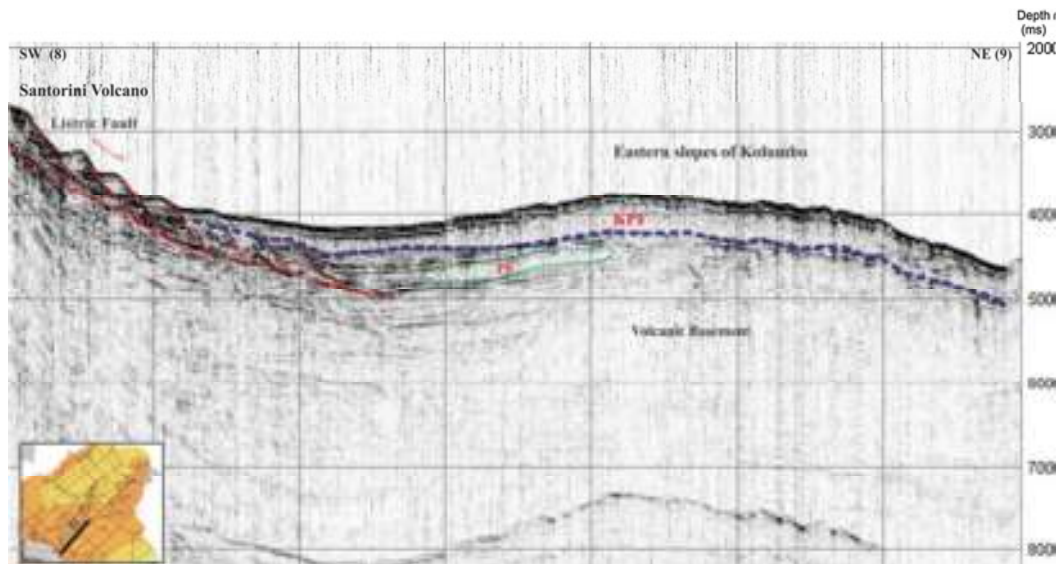


Fig. 3.9 Seismic reflection profile NE of Santorini. Kolumbo pyroclastic flow deposits (Nomikou et al., 2012b)

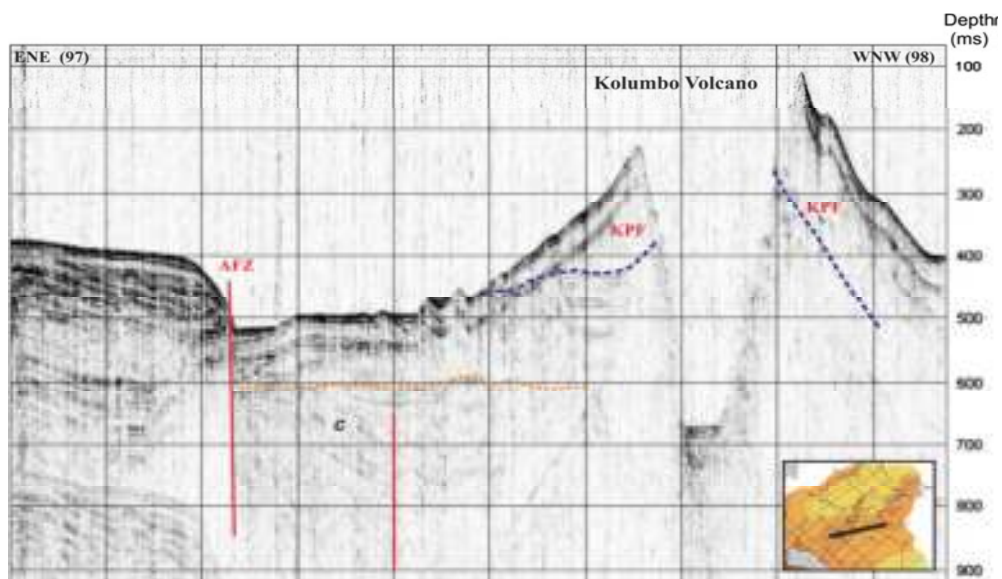
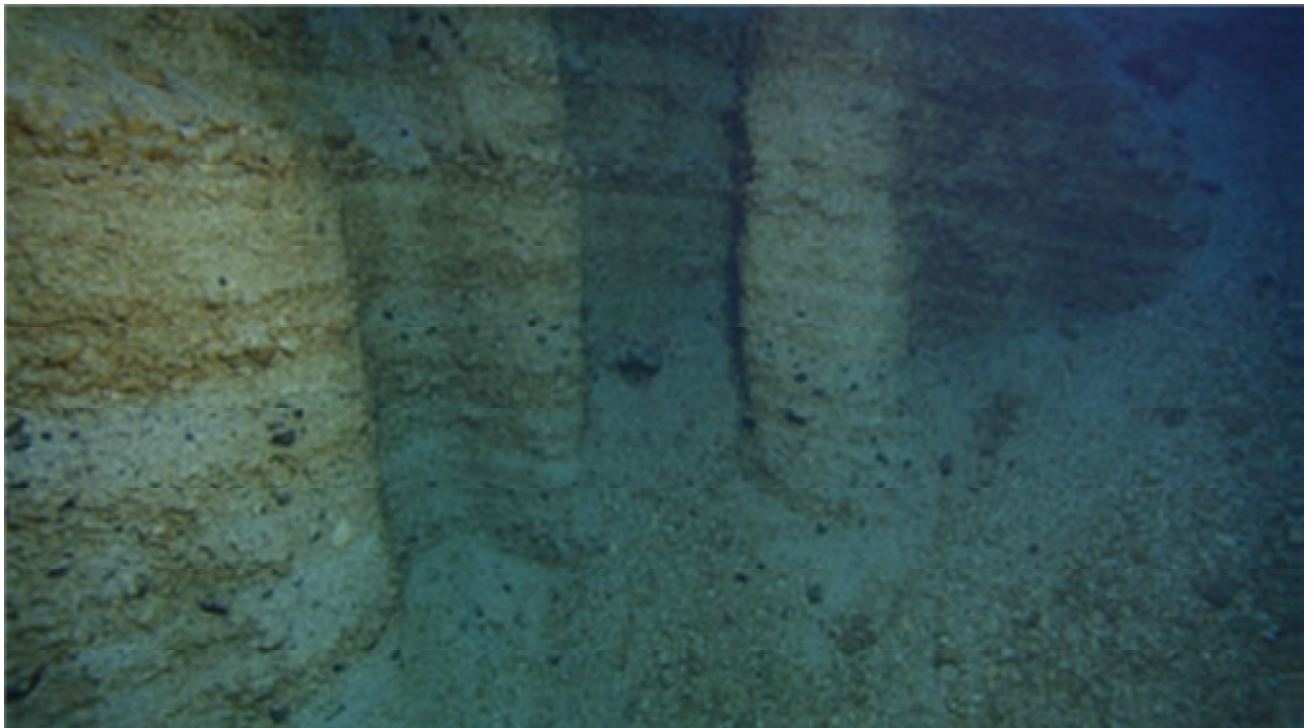


Fig. 3.10 Seismic reflection profile NE of Santorini and crossing Kolumbo volcano. Kolumbo pyroclastic flow deposits (Nomikou et al., 2012b)

Seabed mapping of the Kolumbo submarine volcano have yielded a number of interesting structural features on the slopes that are likely related to the evolution of the volcanic center (Nomikou et al., 2012a). The crater walls display a scalloped morphology that is visible as undulating contour lines. ROV video footage from transects of the crater wall has been used to examine the morphology of the crater region which was found to be controlled by outcrops of a variety of volcanic lithologies including

thick pumice fall/flow accumulations, dikes, intrusions, breccias and mass wasting deposits. The steep crater walls reveal a series of promontories and undulating cliff faces (Fig. 3.11) carved by mass wasting of unconsolidated pyroclastic deposits onto the crater floor. Vertical outcrops form cliffs that taper into promontories that either extend back into another vertical face or transition into talus slopes.



*Fig. 3.11. Submarine erosional processes have given this part of the crater wall an undulating shape (Nomikou et al., 2012b)*

ROV exploration at Kolumbo crater walls has revealed a thick (~200 m) sequence of pumiceous pyroclastic deposits that is the likely a product of the 1650 AD eruption (Fig. 3.12). Two main lithological units were recognized throughout the stratified pumice deposits: a thick-bedded pumice block breccia, and a thin interbedded block breccia and pumice lapilli (Cantner et al, 2010).

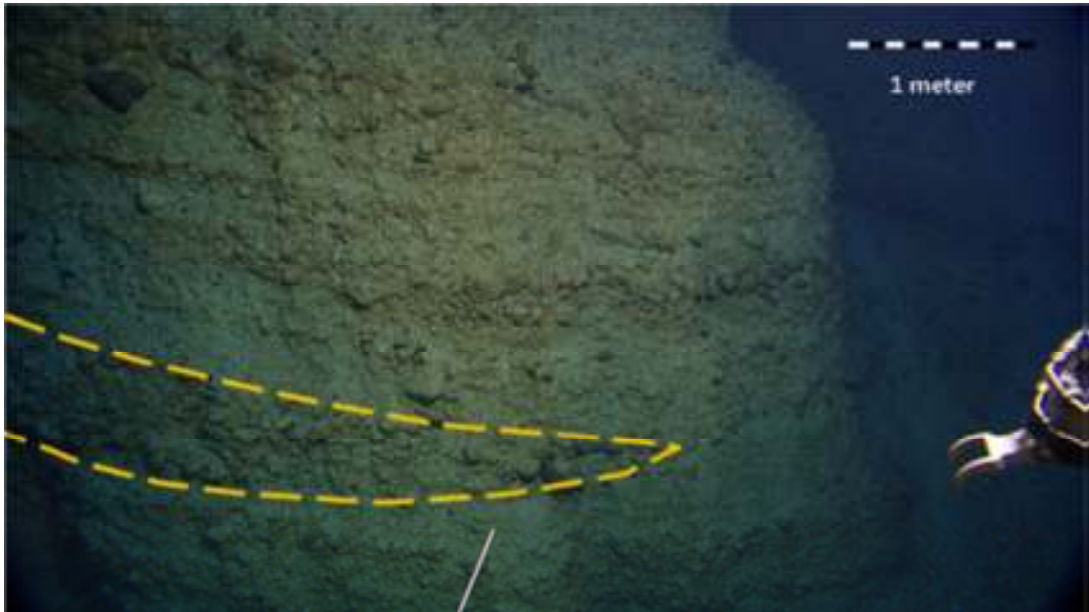


*Fig. 3.12. Vertical cliffs of pumice deposits from the 1650 AD eruption of Kolumbo submarine volcano (Nomikou et al., 2012b).*

Within the crater several prominent ridges extend from the crater walls and slope down into the crater floor. ROV exploration of these ridges revealed outcrops of massive lava flows, dikes (Fig. 3.13) and intrusions that were emplaced prior to the 1650 AD eruption, covered partially with bacteria.

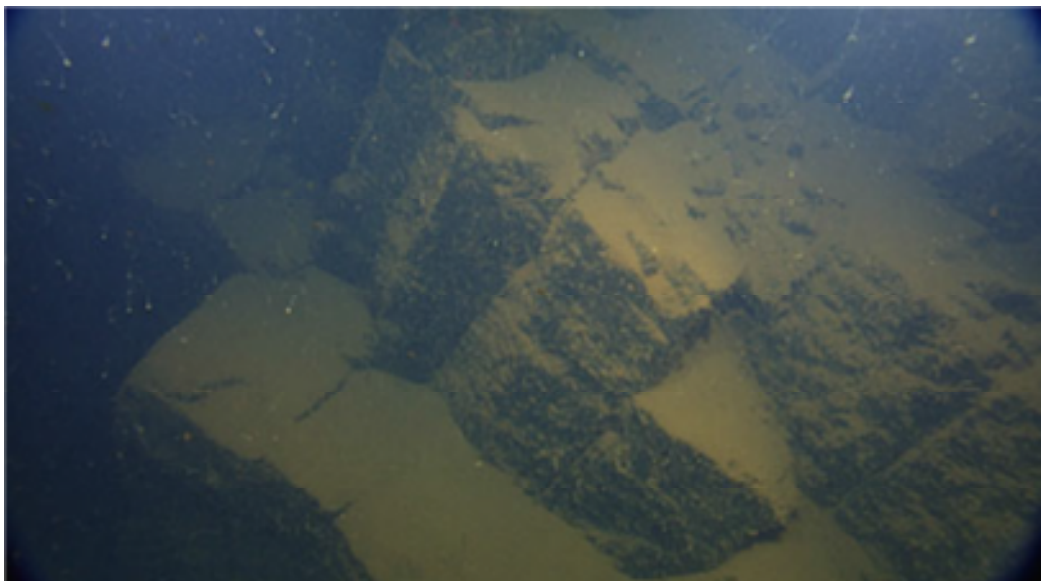


*Fig. 3.13. Lava dyke exposed at the lower part of the eastern wall of Kolumbo submarine volcano (Nomikou et al., 2012b).*

Several transects of the Kolumbo crater walls were conducted using the ROV Hercules in 2010 and 2011. The deposits consist of loosely consolidated subrounded to subangular pumices and mass wasting has produced large talus aprons around the bases. Moderately to well sorted pumiceous block breccia was found at the base of most transects (Cantner et al., 2014). These units appear to display an average grain size around 20-30 cm diameter and are 5 to 10 meters thick.

Interbedded block breccia and pumice lapilli comprise most of the deposits examined in 2006 and 2010. Bed contacts are generally sharp and dip down to the west and to the southwest. Interbedded breccia and lapilli form a series of terraces as the finer grained material provides infilling between the thick breccia beds. Many beds displayed lateral continuity and were well sorted, however others were poorly sorted and contained abundant lithics. These poorly sorted units displayed appreciable variations in bed thickness.

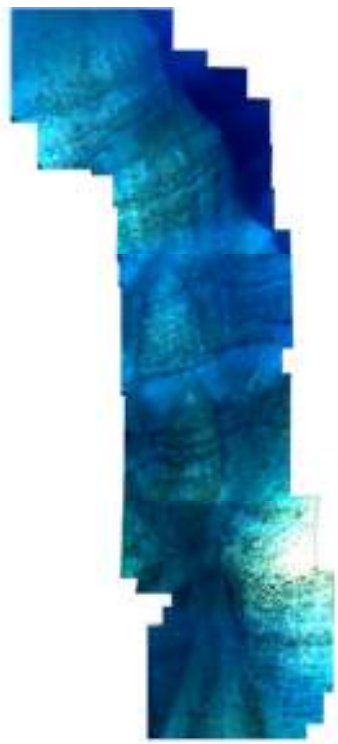


*Figure 3.14 Photomosaic of pyroclastic sequence. The base of the deposits lies at 192 m depth and the top of the deposits lies at 172 m. (Cantner et al., 2014)*

Distinct beds of coarse ash were identified between beds of pumice lapilli. Some of these beds are interpreted to be stratigraphically equivalent and were used to correlate sequence 4 and sequence 5 located ~20 m apart (Cantner et al., 2014). Lithic fragments and thin bedding are clearly visible in the fine grained beds of sequence 5 while the corresponding beds in sequence 4 are deeply incised by erosion. The upper part of sequence 5 is better exposed than of sequence 4 due to the steep angle of the face. At depths above 165 m, the deposits are covered by talus, which forms long slopes between ledges of breccia. The persistence of the horizontal breccia beds suggests that the stratified pumice outcrop continues to the crater rim.

In 2010, ROV footage of stratified pumice deposits on the western crater wall revealed similar stratigraphic units. The deepest exposed deposits at a depth of 220 m are two meters thick and consist of thin beds of pumice block breccia interbedded with fine ash. Massive pumice block breccia, 10 to 20 meters thick, grades upwards to stratified lapilli and block breccia units. Freshly exposed faces reveal abundant lithics in the upper lapilli and breccia beds. Some of the thin, stratified lapilli beds pinch and swell laterally. Observations from both 2006 and 2010 show grain size decreasing from the base of the deposits to the top. Grain size, lateral continuity and sorting of the beds are used to infer the depositional and fragmentation mechanisms occurring during the 1650 AD eruption.

Cantner et al. (2014) developed a model for the evolution of the 1650 AD eruption based on the lithology and stratigraphy of the submarine pyroclastic deposits at Kolumbo. The eruption was driven primarily by exsolution of volatile-rich (~5% H<sub>2</sub>O) rhyolite magma that had been stored at a depth of approximately 5 km in a crustal magma chamber. Initially the eruption appears to have been completely submarine as suggested by historical observations of a period of intense water discoloration at the surface and intense seismicity (fig. 3.15A). For 13 days the eruption was evolving underwater and the magma discharge rate and intensity of the eruption varied intermittently (fig. 3.15B). During this phase, large volumes of unconsolidated rhyolitic pumice accumulated around a submarine vent that may have been as deep as 500 m. Growth of the pyroclastic deposits led to a shallowing of the edifice and eventually a transition to subaerial discharges of highly fragmented magma that generated convective eruption columns that rose to >5 km in the atmosphere (fig. 3.15C). As the vent approached the sea surface the hydrostatic pressure was reduced. This may have

significantly increased the role of phreatomagmatic fragmentation. The increase in phreatomagmatic activity is reflected in the stratigraphy as the upper sequences of the crater wall are finer grained and thinner bedded than those at depth. The presence of large lithic clasts throughout the pumice lapilli units indicates that conduit erosion and vent expansion occurred periodically throughout the eruption. Different facies of the submarine pyroclastic deposits indicate that deposition occurred by both pumice fallout and sediment gravity flows, some of which were likely to at high temperature. Historical reports of fatalities by asphyxiation and burns in the vicinity of Kolumbo and on the shores of Santorini strongly suggest that pyroclastic flows and/or surges were generated from eruption columns that broke the sea surface (fig. 3.15D).

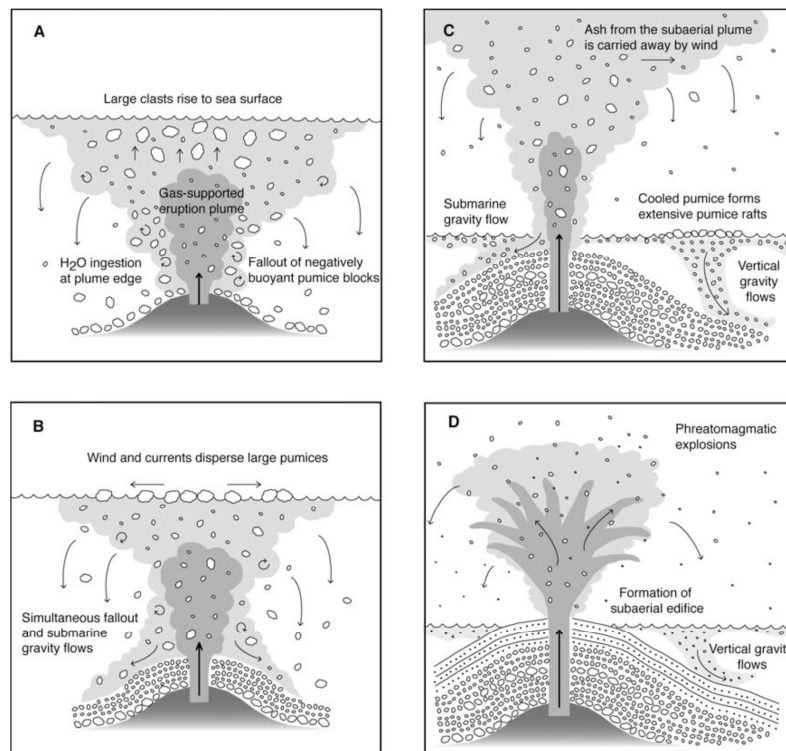


*Fig. 3.15 Model of Kolumbo 1650 AD eruption processes from Cantner et al. (2010). A) Sustained submarine eruption column - ingestion of seawater at the plume edge causes pumice quenching and fallout of negatively buoyant clasts; B) Simultaneous deposition from submarine gravity flows and eruption column fallout; C) Sustained subaerial plume - fallout accumulates in water column and forms vertical density currents; D) Phreatomagmatic activity increases fragmentation.*

### 3.3 HYDROTHERMAL VENT FIELD

Most hydrothermal vent studies have dealt with mid-ocean ridges (Fig. 3.16a), intraoceanic island arcs (e.g. Philippines) (Fig. 3.16b) or subduction systems beneath active continental margins with back-arc marginal basins (e.g. Japan) (Fig. 3.16c). However, unique but less studied, transitional situations exist in convergent settings such as in the Hellenic Volcanic Arc (HVA), where volcanism and hydrothermal activity occur through thinned continental crust.

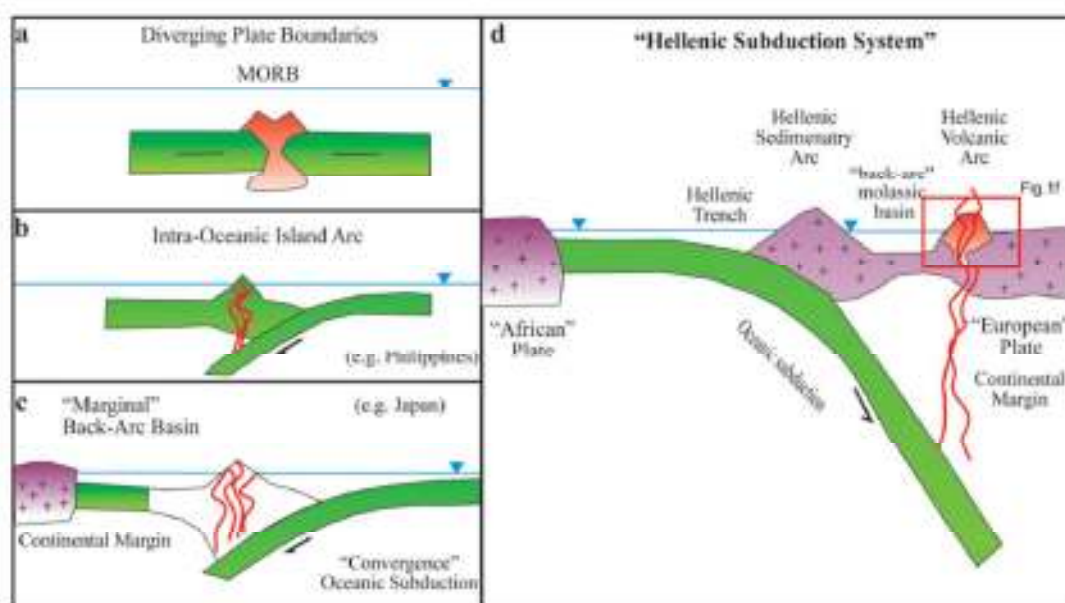
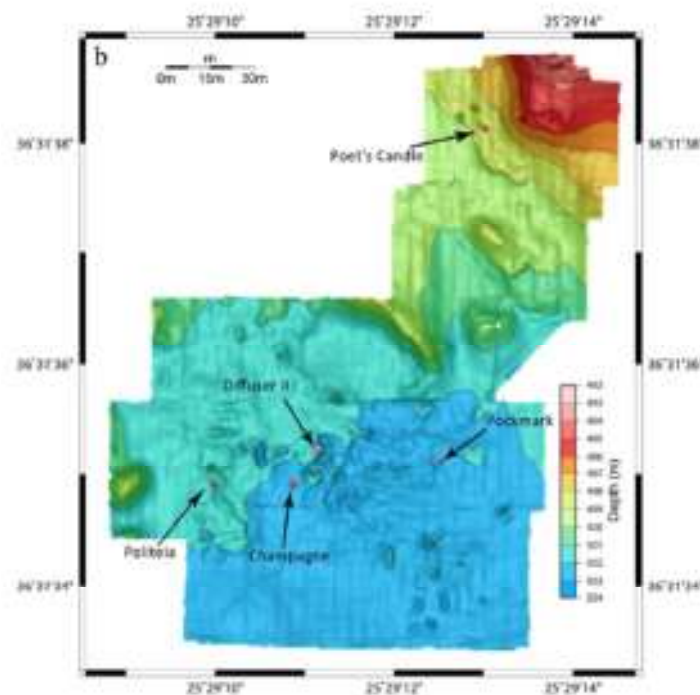


Figure 3.16 Tectonic setting of the Santorini-Kolumbo volcanic field. (a–d): Schematic cartoons of different geodynamic environments where seafloor hydrothermal vents occur. (a) Mid-Ocean Ridges along divergent plates. (b) Intra-Oceanic Arcs within convergent boundaries (e.g. Philippines). (c) Marginal back-arc basins and island arcs along active continental margins with oceanic subduction (e.g. Japan). (d) “Hellenic Subduction System”. The “Hellenic Volcanic Arc”, within active continental margin, developed behind the molassic back-arc basin, hosted over thinned continental crust (Kilias et al., 2013)

Submarine hydrothermal vents are well known for hosting unique, highly productive chemoautotrophic microbial communities. Microorganisms are involved at various levels in the transformation of rocks and minerals at and below the seafloor, therefore microbe-minerals interactions in hydrothermal vents are thought to play an important role in global biogeochemical element cycles, and biomineralization (Southam & Saunders, 2005; Holden et al., 2012; Kilias et al., 2013).

In 2006, ROV explorations in the northern part of Kolumbo's crater floor revealed an extensive "diffuse-flow"-style hydrothermal vent field, Kolumbo Hydrothermal Field (KHF) (Sigurdsson et al., 2006; Kiliyas et al., 2013), between 492 and 504 m depth. In 2010 and 2011, onboard E/V Nautilus, a bathymetric map of KHF created (Fig. 3.17) by utilizing the 1.375 kHz BlueView multibeam sonar, structured light and stereo imagery data (Roman et al., 2012; Kiliyas et al., 2013) acquired by the ROV Hercules. The detailed swath bathymetric mapping using 0.5 m grid interval revealed an extensive field with numerous active vents in the central part of KHF, with larger, but less active vents occurring in the northern part of the crater floor.



*Fig. 3.17 Detailed bathymetric map of Kolumbo hydrothermal vent field located in the northern part of the crater floor (red square in a) (Kiliyas et al., 2013).*

Virtually the entire crater floor of Kolumbo (area of approximately 600 x 1200 m) is covered by a few-cm-thick orange to brown smooth sediment (Sigurdsson et al., 2006; Carey et al., 2011; Kiliyas et al., 2013) that consists of Fe-encrusted flocculent microbial

mats and amorphous Fe-oxyhydroxide deposits. Temperature in the Fe-rich sediment varies between 16.2°C and 17°C. Clear, low-temperature fluids ( $\leq 70^\circ\text{C}$ ) and  $\text{CO}_2$  gas bubbles slowly discharge from the Fe-microbial mats through small pockmark-like craters. This “diffuse-flow” may be supporting microbiological productivity on Kolumbo’s crater floor and may be linked to Fe-mat formation (Edwards et al., 2011; Kiliyas et al., 2013). The seawater column in the crater at depths  $>250$  m, is strongly clouded with reddish-orange and white particles, most likely of Fe-rich plume-dispersed flocculent pieces of the microbial mat. Towards the base of the northern wall at depths of  $\sim 490$  m, white microbial mats were observed as streaks on the wall, interpreted as the result of colonization of low-temperature probably dense-fluid seeps.

The KHF consists dominantly of active and inactive sulphide-sulphate structures in the form of vertical spires and pinnacles, mounds and flanges along a NE-SW trend, sub-parallel to the CSK volcano-tectonic zone (Nomikou et al., 2013a). These vents are surrounded by sites of low-temperature ( $\leq 70^\circ\text{C}$ ) diffuse venting from the Fe-mats. A typical spire-type vent, named Politeia Vent Complex (“Politeia”), covers an area of 5m x 5m in the western part of the KHF. It is dominated by short ( $\leq 3$  m tall), slender, intermediate-temperature diffusely-venting, isolated and/or merged, sulphide-sulphate spires or “diffusers” (Carey et al., 2011 ; Kiliyas et al., 2013). These spires usually taper to their top, and rise up from a hydrothermal mound that grows directly on the sediment and Fe mat-covered seafloor. “Diffuser” spires at Kolumbo discharge clear shimmering fluids, from which sulphide minerals have precipitated prior to discharge (Hannington et al., 2005; Kiliyas et al., 2013). Similar vents have been observed at shallow-water boiling vents on the Tonga arc, SW Pacific (Stoffers et al., 2006) and the Mid-Atlantic Ridge near Iceland (Hannington et al., 2001). The spires lack beehive structures, “black smoke”, and an axial conduit that typify “black smoker” chimneys (Fouquet et al., 1993; Tivey M. 2007). The exterior of the Politeia spires is covered by grayish suspended filamentous microbial biofilms (streamers) that could not be recovered.

In the central part of the vent field are smooth-sided sulphide-sulphate mounds, such as the Champagne Vent Complex (“Champagne”) and the “Diffuser II Vent Complex (“Diffuser II”), that are covered by orange to brown Fe-rich microbial mats. They consist of a basal mound with no spire structures, and commonly discharge streams of bubbles, mainly  $\text{CO}_2$ , from small holes and cracks on their sides and bases; dissolution of the gas

causes accumulation of stably-stratified CO<sub>2</sub>-rich water within the enclosed basin of the Kolumbo crater, and the accumulation of acidic seawater above the vents (as low as pH 5.0) (Carey et al., 2013a, 2013b). In the absence of dissolved oxygen data, a hypothesis of oxygen depletion near the crater floor can be based on the CO<sub>2</sub>-induced density stratification within the crater (Kiliass et al., 2013; Carey et al., 2013a, 2013b). This phenomenon probably leads not only to accumulation of acidic water that is impeded from vertical mixing, but also to oxygen deprivation by precluding efficient transfer into the deeper layer of the oxygenated surface seawater. The highest vent temperature that was measured in 2010 was 210 °C (Carey et al., 2011). The largest observed hydrothermal vent with Fe microbial mat covering is Poet's Candle (height ~4m), located at the northern crater slope with no clear evidence of shimmering fluids.

Two massive sulphide-rich spires, Politeia spire-1 and Politeia spire-2 (samples NA014-003 and NA014-039 in Table 2, respectively), were recovered from "Politeia" at ~500 m depth. The spires were intact and measured ~25 cm long and ~15 cm in diameter. They consist of an anastomosing, discontinuous array of narrow ( $\leq 2$  cm diameter) channels delineating original fluid-flow paths, occurring within a porous sponge-like spire interior. Four mound samples with variable amounts of sulphide and sulphate were collected from vents actively discharging gaseous CO<sub>2</sub> (>99 %w); three from "Champagne" (samples NA014-007, NA014-027 and NA014-028), and one from "Diffuser II" (sample NA014-005).

Sample	Si	Al	Fe	Pb	As	Sb	Zn	Cu	Hg	Tl	Ag	Au
NAO14-003 Poiteia spire-1 (ISSC)	11000	3070	107000	>10000	2740	>2000	>10000	1210	>100	435	>100	17
NAO14-003 Poiteia spire-1 (OASL)	36400	688	6850	5930	>10000	>2000	5950	35	>100	>1000	>100	0.9
NAO14-003 Poiteia spire-1 (SFeC)	21100	1010	19800	4130	7290	>2000	1470	11	>100	868	>100	0.7
NAO14-003 Poiteia spire-1 composite	14100	9280	163000	66400	6430	12600	60900	1690	571	505	1710	18
NAO14-005 Diffuser II		7470	311000	42500	5440	4650	1210	2760	0.1	50	763	16
NAO14-007 Champagne active mound (base)	16600	16500	313000	19700	2290	8010	3900	848	967	260	218	2
NAO14-016 Pout + Conelle sulphide		5910	172000	53500	2640	5680	17800	2210	1	200	686	9
NAO14-027 Champagne active mound-1 (N = 2)	25100	3240	242000	28800	2910	5690	2630	1510	1074	429	191	6
NAO14-028 Champagne active mound-2 (N = 3)	11700	1170	217000	55700	5770	6300	3620	3480	0.7	831	614	5
NAO14-039 Poiteia spire-2 (ISSC)	9070	4920	201000	>10000	2230	>2000	>10000	2940	>100	415	>100	32
NAO14-039 Poiteia spire-2 (SFeC)	5280	1270	10600	5990	747	1380	1430	10	79	80	>100	0.4
NAO14-039 Poiteia spire-2 composite	2510	5470	101000	67100	2350	22400	3060	1300	481	280	1910	12
AVERAGE	14100	5890	166000	35000	3810	8330	10200	1640	397	389	871	9
MAX	36400	16500	313000	67100	7290	22400	60900	3751	1070	868	1910	32
N	12	14	14	10	13	8	10	14	8	13	7	14

Table 3. Average content in ppm of selected elements in hydrothermal vent samples from the Kolumbo deposit (Kiliass et al., 2013)

A vertical water sampling profile conducted directly above the active “Champagne” vent, showed significant positive correlation between the distribution of  $\text{NH}_4^+$  and filterable ( $<45 \mu\text{m}$ )  $\text{Fe}_{\text{FT}}$  ( $R=0.97$ ,  $p < 0.008$  Pearson). The highest levels of  $\text{NH}_4^+$  (21  $\mu\text{mol/l}$ ) and  $\text{Fe}_{\text{FT}}$  (2.1  $\mu\text{mol/l}$ ) were recorded at 500 m depth just above the active vent, while an abrupt decrease in their concentration (14- and 44-fold respectively) was observed within the zone 500 to 400 m depth. These two profiles are almost mirror images of the pH distribution indicating injection of significant hydrothermal quantities of both species from the sea floor into the water column. Intercomparison of the profiles of the nitrogenous species indicate an upward gradual oxidation of  $\text{NH}_4^+$  to  $\text{NO}_2^-$  and finally to  $\text{NO}_3^-$  reaching 30  $\mu\text{mol/l}$  at the 200 m depth, just below the euphotic zone. Such concentrations are by far higher than the typical for the region undeniable proving the  $\text{NH}_4^+$  emanating from the seafloor vents (nutrients concentration range in seawater

profiles from the Santorini Caldera is 57-276 nmol/l  $\text{NH}_4^+$ , 21-87 nmol/l  $\text{NO}_2^-$ , 45-1,500 nmol/l  $\text{NO}_3^-$  while for Fe it is 13-115 nmol/l). The aforementioned oxidation of  $\text{NH}_4^+$  is followed by pH increase indicating  $\text{CO}_2$  depletion.

Dissolution of  $\text{CO}_2$  in seawater is an increase in water density (Haugan & Drange, 1992; Zhang & Kling, 2006; Carey et al. 2013a). Carey et al., 2013a suggests that  $\text{CO}_2$  from the Kolumbo hydrothermal vent field is being sequestered within the crater as a result of the formation of dense water as  $\text{CO}_2$  gas is dissolved in the bottom waters of the confined crater. The closed geometry of the Kolumbo crater facilitates the establishment of a stably stratified density gradient driven by  $\text{CO}_2$  dissolution during gas injection, and leads to accumulation of acidic water that is impeded from vertical mixing.

The results show that in addition to the significant gradient in the pH within the crater, the water column is stably stratified, largely due to the effect of  $\text{CO}_2$  on seawater density (Figure 3.18)

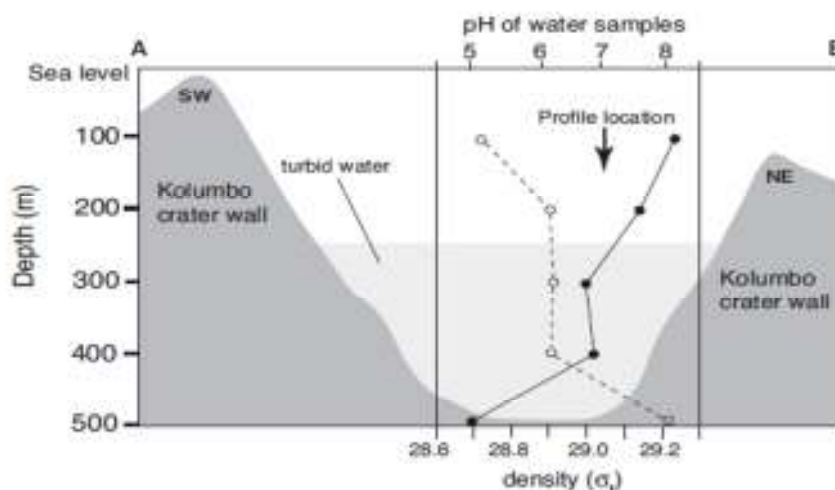


Figure 3.18. pH (solid circles) and density (open circles) of water samples collected along a vertical profile (arrow location) in Kolumbo submarine volcano. Density in  $\text{kg m}^{-3}$  equals plus 1000 where  $\sigma_t$  is the sigma (t) value (Carey et al., 2013a).

## Chapter 4

### CTD MEASUREMENTS

This chapter describes the technical aspects of the CTD data collection during a marine geological survey using the E/V Nautilus in August 2010 (NA007), October 2010 (NA011) and September 2011 (NA014). The three cruises of Nautilus was part of 2012 vehicle's field season in the Mediterranean Sea. All data were collected from the Anhydros basin northeast of Santorini Island, where the Kolumbo volcano lies within. Measurements were performed mainly on the hydrothermal vent field at the northeast part of the Kolumbo's crater and at seventeen (17) smaller cones extending northeast of Kolumbo outside the crater.

#### 4.1 THE CRUISES

##### *4.1.1 Cruise NA007 (August 2010)*

Cruise NA007 focused on five principal areas of exploration to better understand the nature and extent of submarine volcanism and hydrothermal circulation in the area to the northeast of the main volcanic island, Santorini (E/V Nautilus, expedition NA007 & NA011 report, 2011). Three types of operations were conducted within the Santorini and Kolumbo craters project: remotely operated vehicle (ROV) surveys and sampling

using *Hercules* and *Argus*; side scan survey and sub-bottom profiling using *Argus*; and coring using the *Hercules* push cores.

During cruise NA007 the NE Kolumbo crater line, the crater walls of Kolumbo, the submarine volcano flanks, the Kolumbo hydrothermal vent field at the northeast part of the crater floor and the Santorini debris avalanche field were studied (Fig. 4.1). The expedition lasted from July, 29<sup>th</sup> 2010 till August, 12<sup>th</sup> 2010. ROV *Hercules* and ROV *Argus* were employed for the CTD data collection.

Three types of operations were conducted on this cruise: remotely operated vehicle (ROV) surveys and sampling using *Hercules* and *Argus*, side scan survey and sub-bottom profiling using *Argus* and coring using the *Hercules* push cores. CTD data were collected by the instrument incorporated in *Hercules*.

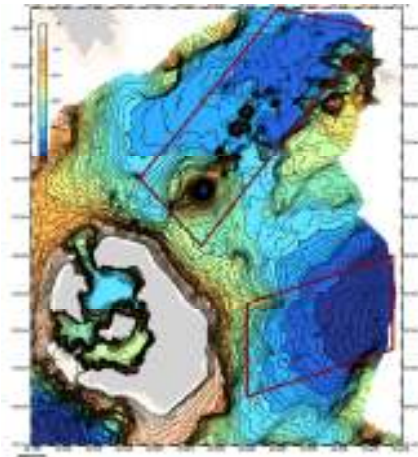


Figure 4.1 Operating areas for NA007, Santorini and Kolumbo volcanoes (bathymetry) are marked by red enclosures (E/V *Nautilus* expedition NA007 & NA011, report, 2011).

At the NE Kolumbo crater line, nineteen (19) cones to the NE of Kolumbo Submarine Volcano have been explored to determine the structure, geological deposits, age relations, hydrothermal venting and biological communities. Faulting and tectonic processes that control the orientation of volcanism in the area have also been investigated.

Subsequently, an exploration of the stratigraphic succession in the Kolumbo's crater walls was carried out with emphasis on mapping out the distribution of the upper pumice sequence (1650 AD eruption), potential areas of dome or dike outcrops on the crater walls were investigated, and water column variations within the crater were determined. In addition, the surface morphology of Kolumbo's submarine flanks was explored to investigate processes of submarine deposition of volcanoclastic material

(1650 AD pyroclastics) and curvilinear scarps at the W-NW base of Kolumbo's flanks were examined.

At the hydrothermal vent field, special focus was given on determining the composition of gases and fluids being discharged from active hydrothermal vents on the floor of Kolumbo submarine volcano (500 m depth). Additional samples of hydrothermal vent chimneys and biological organisms were additionally collected. Temperature measurements and observations of vent types and vent's distribution were carried out.

In the basin on the southeast side of Santorini, near Anafi Island, the seafloor consists of a large number of blocks, which is the debris avalanche field of Santorini. There, the blocky/hummocky topography was explored and the distribution, size and lithology of potential slide blocks were investigated.

The Kolumbo hydrothermal vent field is unusual in that many of its vents are giving off both high temperature fluids and gases. The gases were sampled using pre-evacuated gas tight bottles that were positioned over active gas streams with the ROV. Samples were also collected of the chimneys at several vents sites (Fig. 4.2, 4.3).



*Figure 4.2 Sample of gases from hydrothermal vents in the crater of Kolumbo volcano (E/V NAUTILUS, expedition NA007 & NA011 report, 2011).*

A systematic survey of the vent field was conducted in search of new vents in the crater floor and slopes. Several areas of new venting were discovered in the northern part of the crater and further up the crater walls to depths of 300 meters. A spectacular

higher-than six-meters vent was found just north of the vent field discovered in 2006 (Fig. 4.4). This vent was completely draped in bacteria and exhibited minor fluid venting at its top. Attempted sampling of this vent demonstrated that it was very friable and likely composed of iron oxides, not sulphides, unlike the other vents on the crater floor.



*Figure 4.3 Sampling of a vent chimney by ROV Hercules in the crater of Kolumbo volcano (500 m depth) (E/V Nautilus, expedition NA007 & NA011 report, 2011).*



*Figure 4.4 A large (>6m high) hydrothermal vent in the northern crater floor of Kolumbo volcano, completely draped in brownish-orange bacterial mat (E/V Nautilus, expedition NA007 & NA011, report, 2011).*

#### 4.1.2 Cruise NA011: Kolumbo and Nisyros Volcanoes

Cruise NA011 lasted from October, 3<sup>rd</sup> 2010 till October, 16<sup>th</sup> 2010 and conducted at Kolumbo and Nisyros volcanoes (E/V Nautilus, expedition NA007&NA011 report, 2011). The first five days was a continuation of cruise NA007, exploring the crater walls and the hydrothermal vent field of Kolumbo (Fig. 4.5) and then the vessel was transferred to Nisyros and surrounding areas (Fig. 4.6).

The primary objective of the work at Kolumbo volcano was to experiment with high-resolution mapping techniques, including stereo-imaging, structured light and multibeam mapping. The areas identified for mapping are: (1) the inner walls of Kolumbo crater, which poses a technical challenge (reconfiguration of the mapping sensor suite was needed), and (2) the hydrothermal vent field in the northern quadrant of Kolumbo crater.

Four types of operations were conducted on the Santorini/Nisyros Project:

- Remotely operated vehicle (ROV) surveys and sampling using *Hercules & Argus*
- Side-scan survey and sub-bottom profiling using *Argus*
- Multibeam survey using *Hercules & Argus*
- Coring using the *Hercules* push cores.

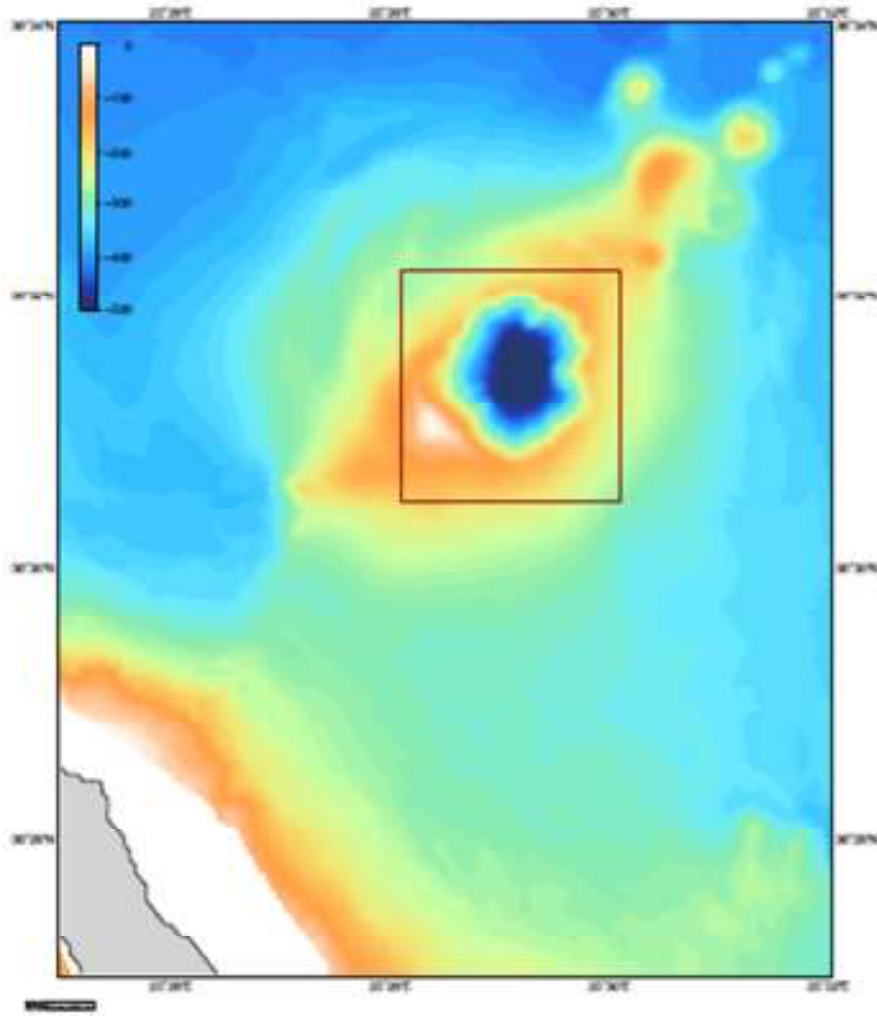


*Figure 4.5 Survey during October 3-18 took place only within the crater of Kolumbo (red box) (E/V Nautilus, expedition NA007 & NA011, report, 2011).*

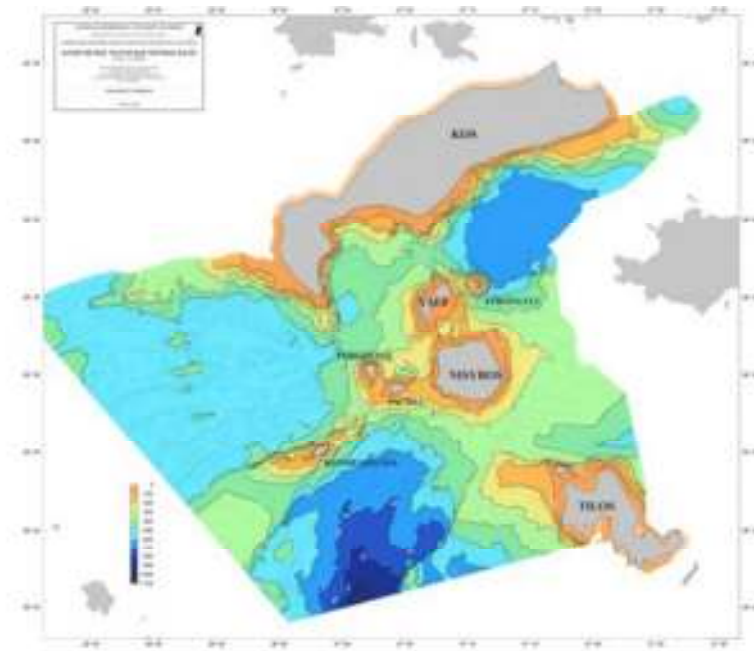


Figure 4.6 A general map of operation during NA011 (Oct 9-16): Nisyros and surrounding areas. All work took place within Greek waters (E/V Nautilus, expedition NA007 & NA011, report, 2011).

#### 4.1.3 Cruise NA014: Hellenic Volcanic Arc and Cretan Basin

The cruise NA014 took place during 1-10 September 2011 at the Hellenic Volcanic Arc and Cretan Basin (E/V Nautilus, expedition NA014 report, 2012). The project was intended to be a continuation of the previous projects since 2006. In 2011 three locations were investigated: i) Kolumbo submarine volcano, ii) Christianna volcanic domes, and iii) Cretan basin (Fig.4.7).

Research in Kolumbo volcano continued work that has been ongoing for several years. The objectives that the scientific team focused on, at the Kolumbo volcano, were: i) high-resolution mapping of the hydrothermal vent field and pumice walls, and ii) biogeochemical sampling of geological deposits, bacteria, water and gases that exist on and around the hydrothermal vent field. The discovery of an actively-forming Kuroko-type mineral deposit in the crater of Kolumbo volcano presented an outstanding opportunity to investigate this style of economically important mineralization (Sigurdsson et al., 2006). During the 2010 field season, the gases being discharged from the Kolumbo vents was determined that are composed almost entirely of CO<sub>2</sub>. This large

concentration of CO<sub>2</sub> into the water poses many unanswered questions, such as on the stability and toxicity of the water. These questions were investigated during the 2011 fieldtrip.

In total, 26 rock and sediment samples (with bacteria), 10 Niskin water samples and 14 gas samples from the Kolumbo vent field were collected. The first analytical data showed that active and extinct chimneys are built of Fe, Pb, Cu, and Zn sulfides, and Ba and Ca sulfates. Iron-rich minerals and some arsenic-sulfur minerals that may be of biogenic origin cover some of the Kolumbo chimneys. Gas samples collected in 2010 showed that 99% of the gas being emitted from the hydrothermal vents is composed of CO<sub>2</sub> (Carey et al., 2011). Preliminary onboard analysis of water samples in 2011 shows pH levels lower than average.

Kolumbo mapping efforts focused on two new ways to visualize active physical processes. First, the hydrothermal vent field and actively bubbling vents were mapped at high resolution. Second, the use of structured light mapping over areas venting hot water without bubbles (“shimmery” water) was tested. The observed refraction of light can be used to visualize these venting areas.

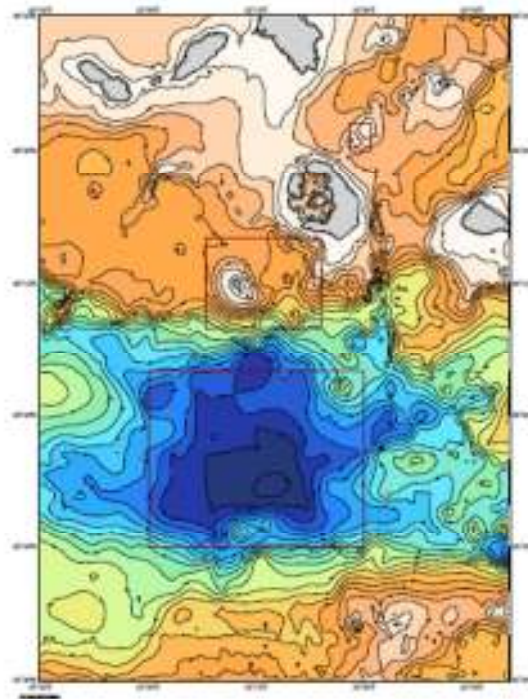


*Figure 4.7 Operating areas for NA014, the Hellenic Volcanic Arc and Cretan Basin in the Southern Aegean Sea (E/V Nautilus, expedition NA014 report, 2012).*

## 4.2 METHODOLOGY

### *4.2.1 Equipment – Sampling statistics*

Expeditions NA007, NA011 and NA014 were conducted by *E/V Nautilus* (Fig. 4.8) that is a fully equipped with high-tech instruments Vessel (Bell et al., 2012). *E/V Nautilus* was built on 1967 in Rostock, Germany.

- Length 64.23 meters
- Beam 10.5 meters
- Draft 4.9 meters.



*Figure 4.8 Exploration Vessel Nautilus*

Measurements were conducted by instruments integrated in ROV *Hercules* and ROV *Argus*.

The *Hercules* and *Argus* system is a state-of-the-art deep-sea robotic laboratory capable of exploring depths up to 4000 meters (Phillips et al., 2011). Each remotely operated vehicle (ROV) has its own suite of cameras and sensors that receive electrical power from the surface through a fiber optic cable, which also transmits data and video. Engineers and scientists command the vehicles from a control room aboard the *E/V Nautilus*, with some dives lasting more than three days long.

*Argus* was first launched in 2000 and was soon followed by *Hercules* in 2003. The system is a versatile tool capable of supporting a wide range of oceanographic instrumentation and sampling equipment; they were employed in surveying ancient

shipwrecks, discovering hydrothermal vents and exploring habitats in oceans and seas around the world.

**ROV *Argus*:** Capable of working as a stand-alone system, *Argus* becomes a towed-body instrument for large scale deepwater survey missions. Sidescan sonar looks out on either side of the vehicle up to 400 meters away, identifying features as small as a brick.

Depth capability	6,000 meters, currently limited by cable length
Cable	4,000 meters
Size	3.8m long x 1.2m wide x 1.3m high
Weight	1,800 kilograms
Maximum transit speed	2 knots
Ascent/Descent rate	30 meters/minute
Propulsion	Two Deep Sea System International 404 brushless DC thrusters for heading control

*Table 4.1 General features of ROV Argus*

ROV *Argus* incorporated sensors and navigation is:

- USBL Navigation: TrackLink 5000 MA system
- Heading: TCM2 magnetic compass, Crossbow magnetic compass
- Pressure Sensor: Paroscientific Digiquartz 8 CB series
- Altimeter: Benthos PSA-916
- Forward-Looking Sonar: Mesotech 1071, 325 kHz
- Side-Scan Sonar: Edge-Tech 4200 MP transducers from Diana can be installed by request
- Subbottom Profiling Sonar

ROV *Argus* is also equipped with cameras and lights.

**ROV *Hercules*:** A 20-hp electric/hydraulic pump powers the mechanical functions on *Hercules*. Two manipulator arms, one dexterous and the other strong, work together to sample and move equipment around on the seafloor. It is also equipped with a number of tools, including a suction sampler, sampling boxes with actuating trays, and sediment coring equipment, as well as several other purpose-built tools for different scientific objectives. The ROV *Hercules* is equipped with a suite of mapping instruments that enable detailed visual and acoustic seafloor surveys. The mapping sensors include a 1.375 kHz BlueView Technologies multibeam, verged color and black and white 12-bit

1360 x 1024 Prosilica stereo cameras, and a 100 mW 532 nm green laser sheet. The sensors are mounted near the rear of vehicle and arranged to image a common area. The vehicle navigation data comes from an RDI Doppler velocity log (DVL), IXSEA OCTANS fiber-optic gyroscope, and a Paroscientific depth sensor.

Depth Capability	4,000 meters
Tether	30-45 meters, 20 millimeters diameter, neutrally buoyant
Size	3.9 meters long x 1.9 meters wide x 2.2 meters tall
Mass	~2,500 kilograms in air
Maximum Transit Speed	1 meter/second
Maximum On-Bottom Transit Speed	0.5 meters/second, no sampling
Descent/Ascent Rate	30 meters/minute

*Table 4.2 General features of ROV Hercules (Bell et al., 2012)*

ROV *Hercules* incorporated sensors and navigation is:

- Gyro: Ixsea Octans fiber optic northseeking
- Pressure sensor: Paroscientific Digiquartz 8 CB series
- CTD: Sea-Bird FastCAT 49 (Sea-Bird Electronics, Inc., User's Manual Version #011, 09/08/11)
- Optode: Aanderaa 3830
- Temperature Probe: Woods Hole Oceanographic Institution high temperature probe (0°-500° C)
- USBL Navigation: TrackLink 5000MA system
- Doppler Navigation & Altitude: RDI Workhorse Navigator Doppler Velocimeter, 600kHz
- Forward-Looking Sonars: Mesotech 1071 profiling sonar, 600 kHz; TriTech Super SeaPrince 675 kHz



*Figure 4.9 ROV Hercules (Bell et al., 2012)*

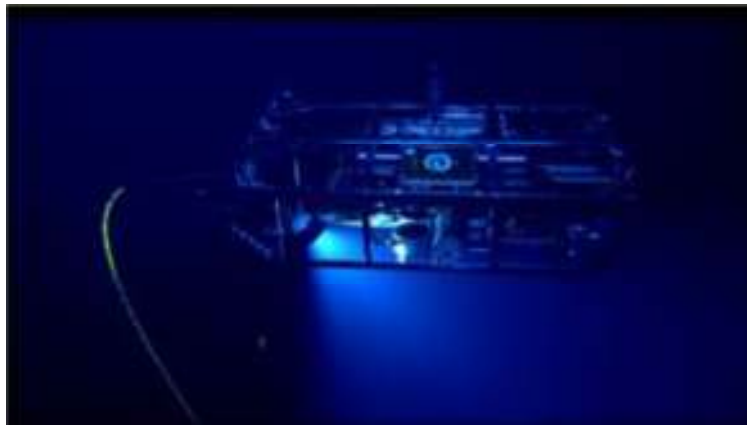


*Figure 4.10 ROV Argus (Bell et al., 2012)*

CTD data in Nautilus expeditions were collected using the SeaBird FastCAT49 (SeaBird, 2013), which is an integrated CTD sensor intended for use as a modular component in towed vehicles, ROVs, AUVs, or other autonomous platforms that can supply DC power and acquire serial data. FastCAT's pump-controlled/TC-ducted flow feature minimizes salinity spiking. Its 16 Hz sampling provides high spatial resolution of oceanographic structures and gradients.

FastCAT's temperature thermistor and conductivity cells are the same as in the *911plus* CTD system (Sea-Bird Electronics, Inc, User's Manual Version #015, 27/09/13). The strain-gauge pressure sensor is offered in eight full scale ranges from 20 to 7000 dbars. Sophisticated interface circuitry provides very high resolution and accuracy.

FastCAT is an easy-to-use, light and compact instrument ruggedly made of titanium and other low-maintenance (plastic) materials; it is well suited to even the smallest vehicle. Titanium housing allows the sensor to dive up to 7000 meters. There are straightforward commands for continuous (full rate or averaged) or single-sample acquisition. EEPROM-stored calibration coefficients permit data output in ASCII engineering units (temperature degrees °C, conductivity Siemens/m, pressure decibars, Salinity [PSU], and sound velocity [m/sec]), or the user can select raw data output if desired.

The ROV was operated in drop down and in autonomous sampling mode, i.e. runs continuously sampling at 16 scans per second (16 Hz). It can be set to average up to 255 samples, transmitting only the averaged data. Programmable real-time processing (aligning, filtering, and correcting for conductivity cell thermal mass effects) provides high quality data for applications where post-processing is not feasible. FastCAT can be programmed to begin autonomous sampling when power is applied or on command. During the Nautilus expeditions, CTD data were collected by cast method.



*Figure 4.11 SEABIRD FastCAT 49 (Sea-Bird 2013)*

On NA007 sixteen Hercules/Argus dives took place, with mean depths ranging from 152 to 518 m. Average bottom time was approximately 14 hours; total bottom time was approximately 224 hours. Approximately 108 km were surveyed with the vehicles.

On NA011 nine ROV's dives were completed, with mean depths ranging from 236 to 500 m. Average bottom time was approximately 20 hours; total bottom time was approximately 179 hours. Approximately 48 km were surveyed with the vehicles.

#### *4.2.2 ANALYSIS TOOLS*

The total data was about 40 GB in plain ASCII format. Firstly, the format was consolidated and data were presorted. The analysis was performed on Ubuntu Linux and Mac OSX platforms. Batch script files were created, which contained series of commands, based on open-source utilities (awk, bash etc). The data analysis sequence was focused on a multi-parametric approach and depending on what information wanted to be extracted, batch files were modified, accordingly. Special emphasis was given on salinity, conductivity, temperature and sound velocity. In addition, there was a day-by-day and hour-by-hour approach of the results, especially for data collected at fixed depths above the vents. The examination of 3D and 2D correlations of the above parameters resulted in numerous plots. Every possible correlation was examined and gnuplot (Gnuplot Version 4.6, 2012) was employed to visualize the information. In total, more than 8,000 graphics were created. Specific dates and hours were selected, based on where vent activity, parameters anomalies and any other interesting feature were detected. Due to the extremely large volume of information, only the most characteristic cases are presented in the next chapter (Chapter 5).

In addition to CTD data, geospatial data were analyzed and maps were created by MapInfo Professional Version 10.0 to identify the exact spots of the measurements. Two vertical profiles of the crater floor, one NNE-SSW direction and one NNW-SSE direction, were created by Global Mapper to combine the CTD info with the geomorphology of the volcano.

## Chapter 5

### RESULTS

Results presented in this thesis are drawn from the analysis of the CTD data collected during the three cruises of E/V Nautilus. About 8,000 2D and 3D plots have been created on an hour-by-hour and day-by-day basis in every possible combination involving the parameters investigated. Correlations of two parameters are DC, DT, DS, DV, TC, TS, CS and correlations of three parameters are DTC, DTS, DTV and CSV. Anomalies in the standard values were detected in some of the graphics, which are presented in the following paragraphs.

The importance of temperature, salinity and conductivity variations in relation with the depth is explored in the curve shape of DC, DT, DS, DV figures. In addition, the correlation between salinity and conductivity is illustrated in CS figures and compared to related literature (Milerro, 1996). Although rare in international literature, 3D correlations are examined. There was special focus on time slots when hydrothermal activity showed extensive excess. This is useful for comparison between the Kolumbo's hydrothermal vent fields and the inactive cones outside the crater.

Maps showing the location where the measurements were performed have been created with the MapInfo using the coordinates recorded by ROV *Argus*. An offset of

about 12 m NE is observed in the Hercules coordinates due to the 20 m tether cable that connects Argus with Hercules.

## 5.1 NA007 RESULTS

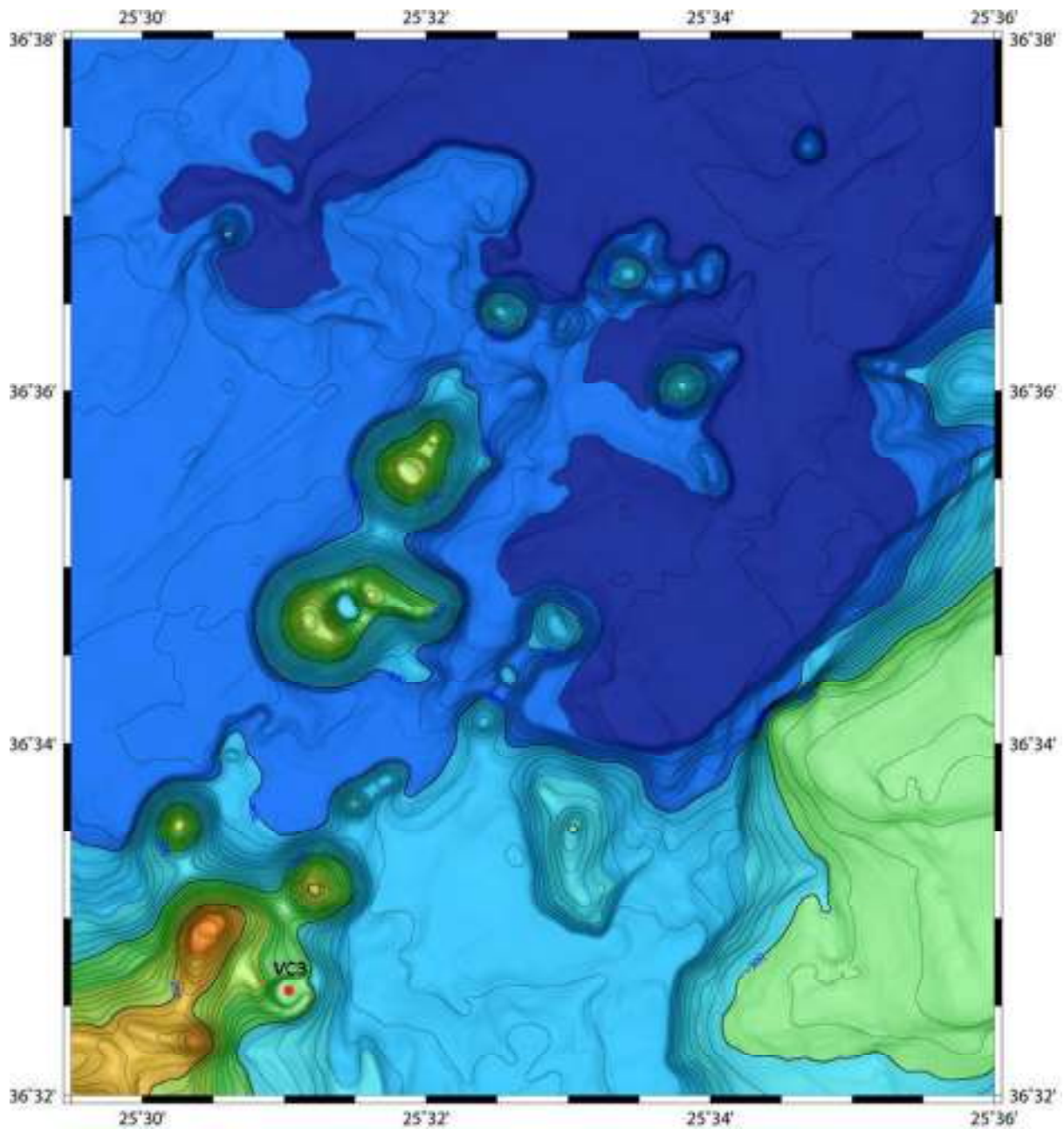


*Figure 5.1 Sampling locations in the VC3 on 29/7/2010, 11.00 a.m. (Bathymetric map, Nomikou et al., 2012a)*

Scanning at Kolumbo site / 29.07.2010

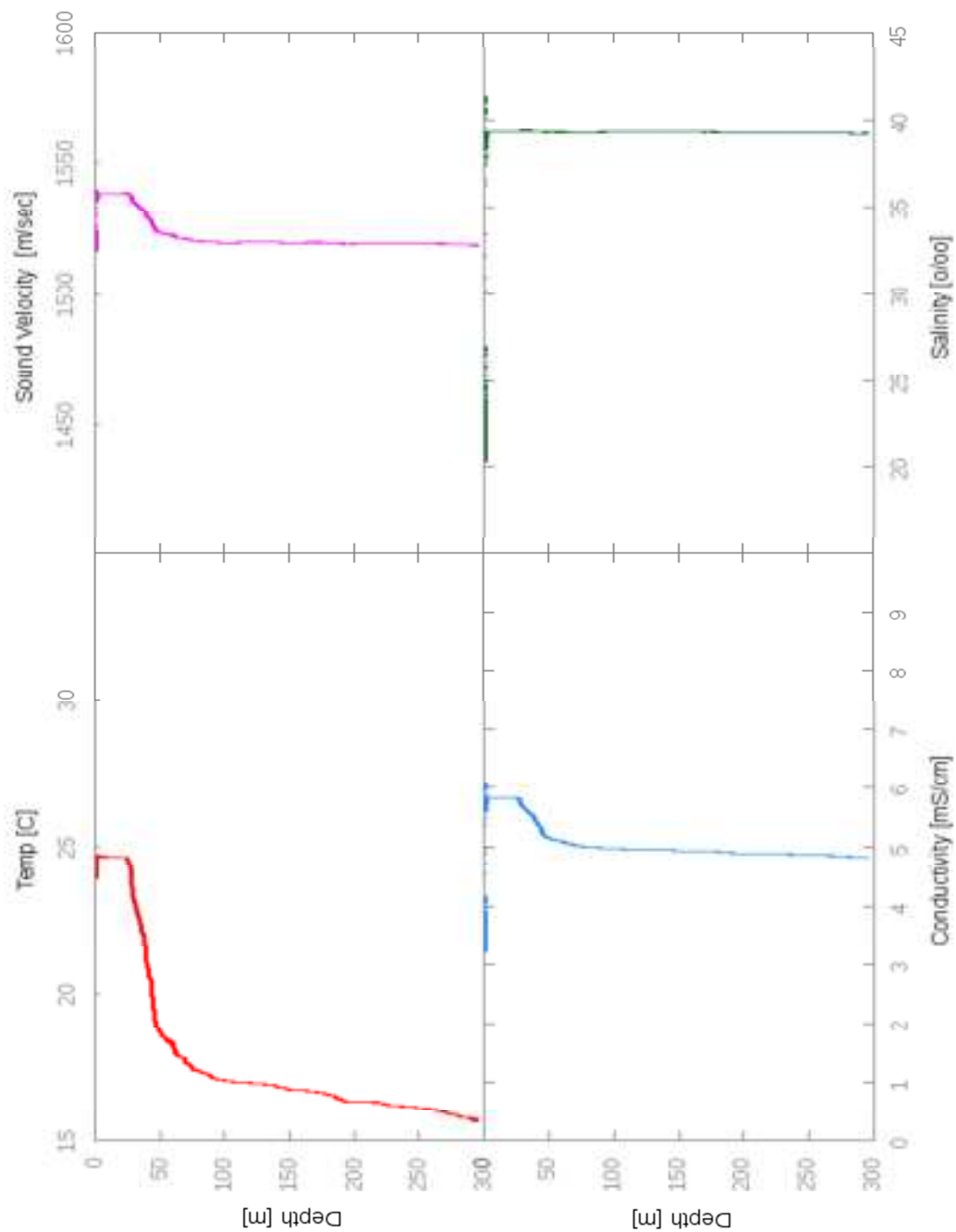


Fig. 5.2: Parameters distributions with the depth at 11.00 a.m. in the VC 3 (please see sideways)

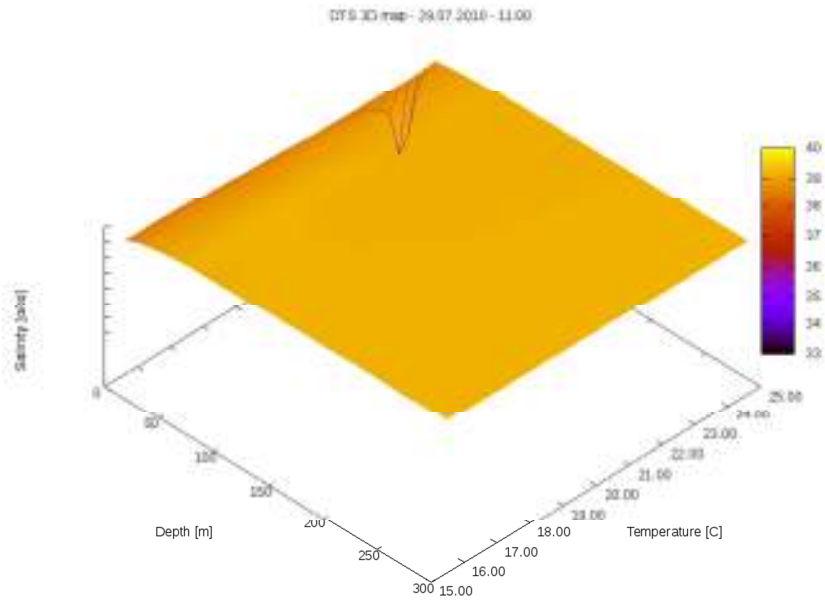


Fig. 5.3: 3D correlations of temperature, salinity & depth at VC3 (11.00 a.m.)

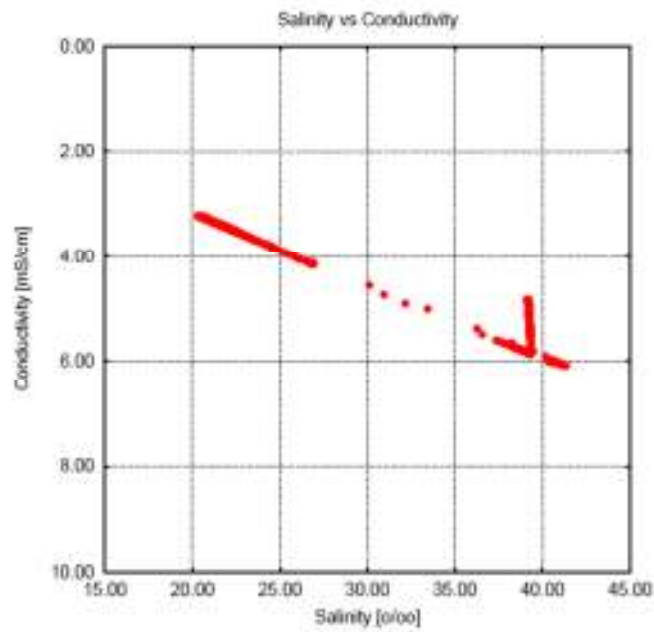
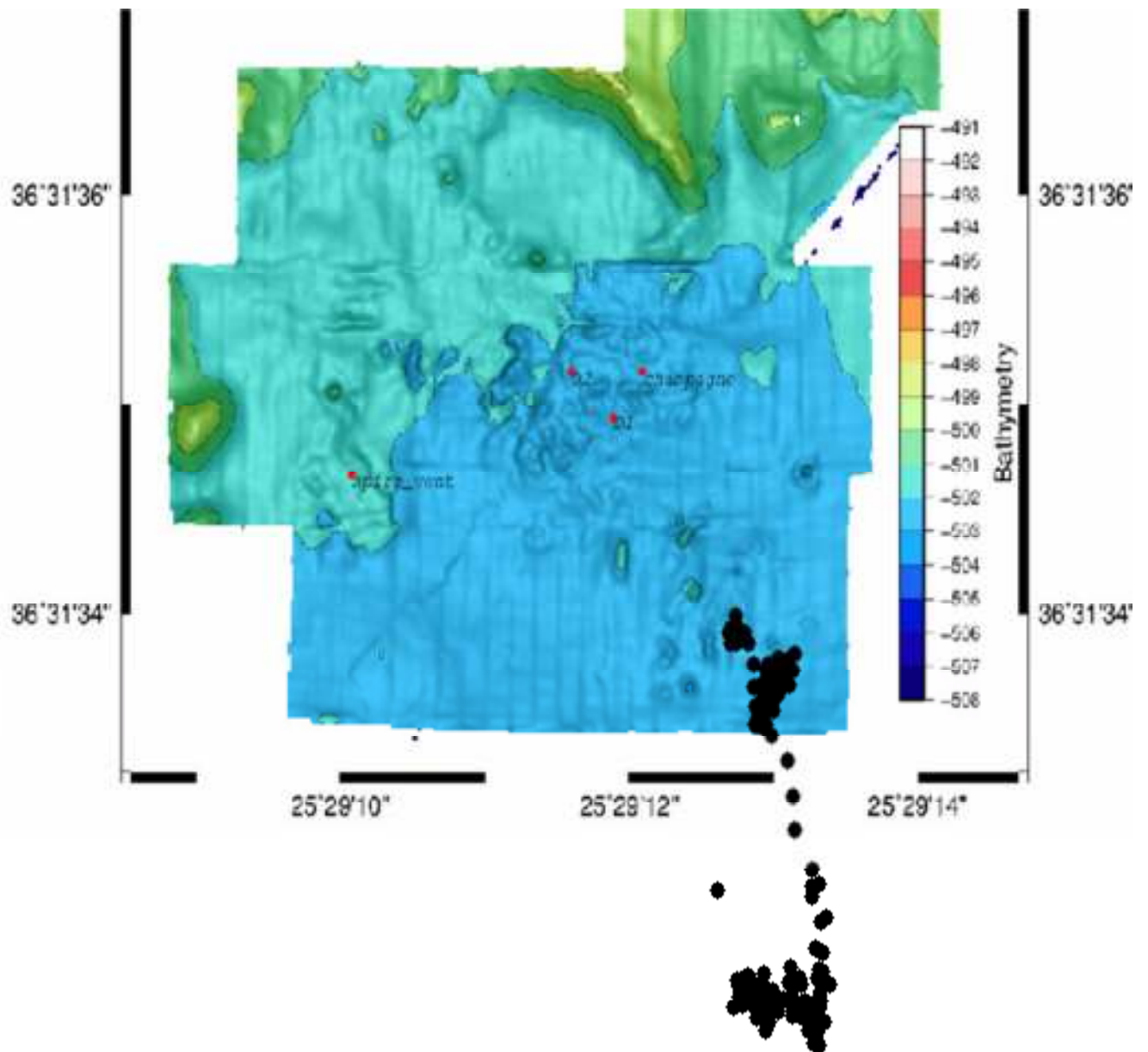


Fig. 5.4: Correlation between salinity and conductivity at 11.00 a.m. in VC3



*Fig. 5.5 Black dots indicate the sampling locations above the hydrothermal vent field as recorded by ROV Hercules (31/07/2010, 14.00 p.m.)*

Scanning at Kolumbo ste / 31.07.2010

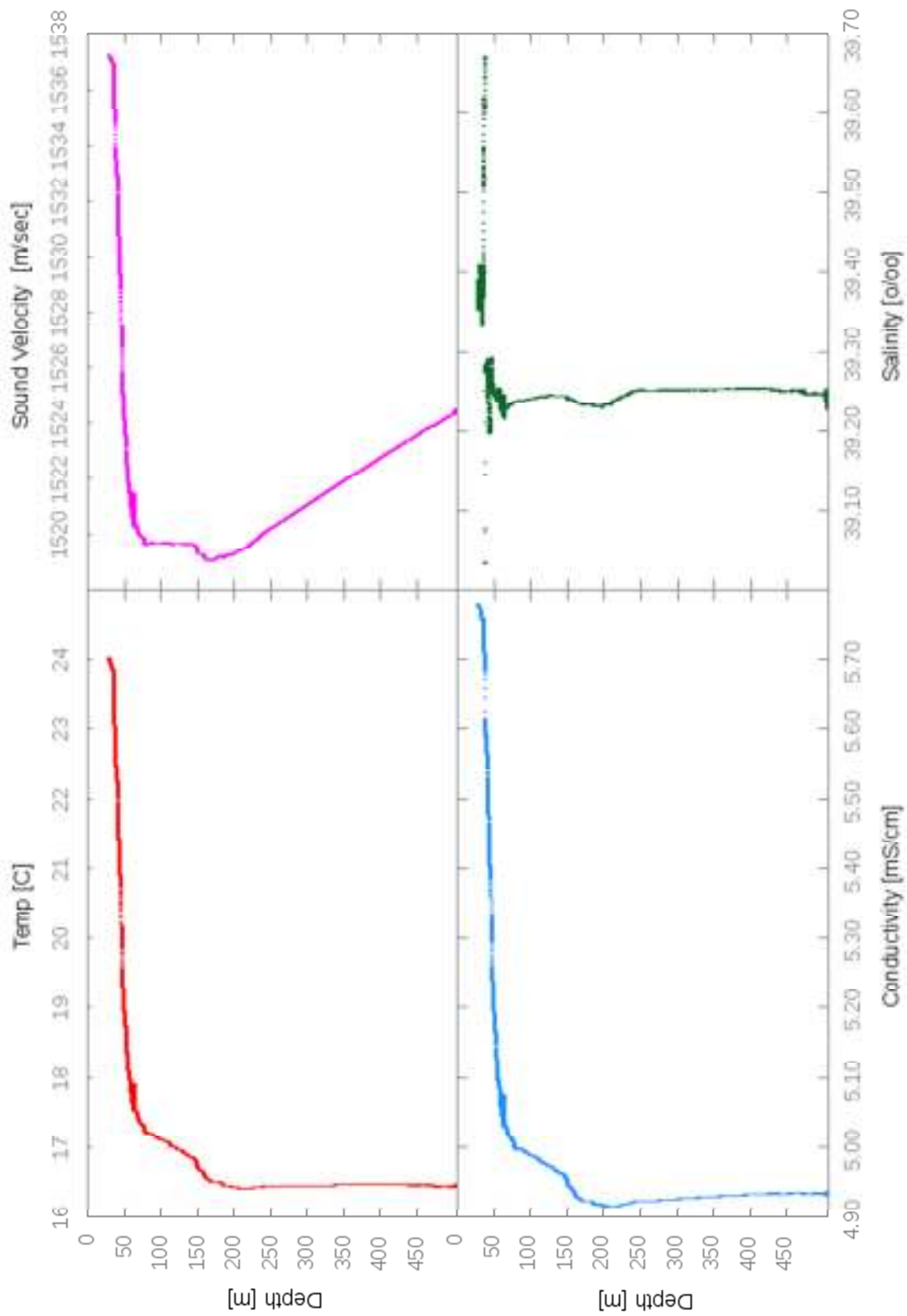


Fig.5.6 Vertical profile of parameters with the depth (31/07/2010, 14.00 p.m.),

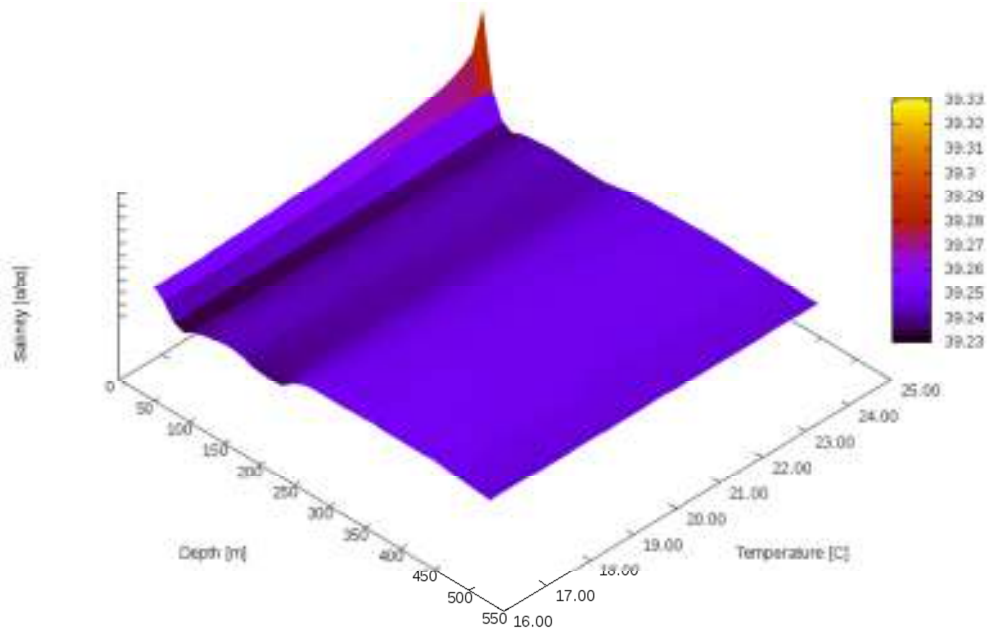


Fig. 5.7 3D correlations of temperature salinity & depth (31/07/2010, 14.00 p.m.)

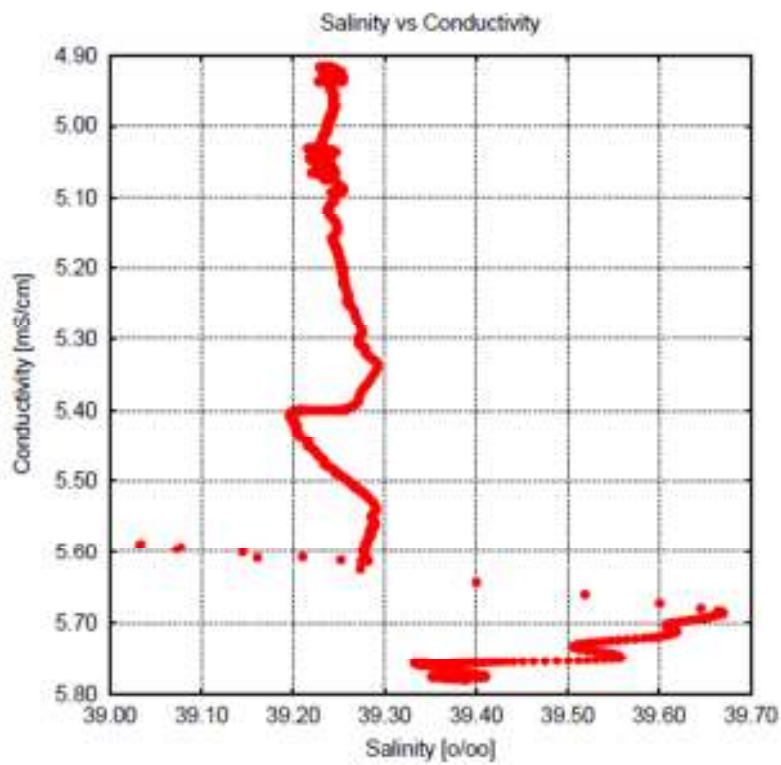


Fig. 5.8 Correlation between salinity & conductivity (31/07/2010, 14.00p.m.)

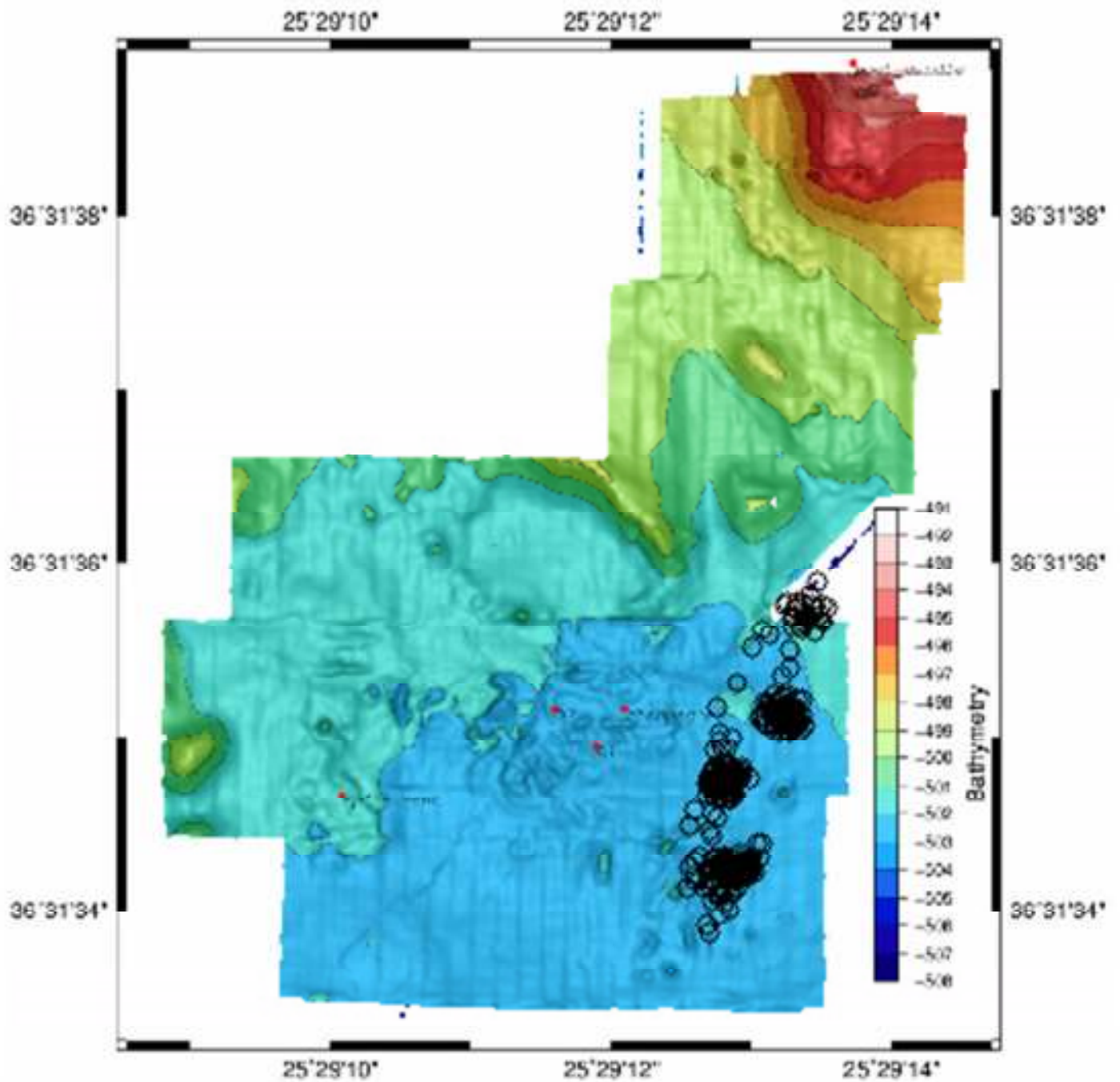


Fig. 5.9 Black dots indicate the sampling locations above the hydrothermal vent field as recorded by ROV Hercules (31/07/2010, 15.00 p.m.)

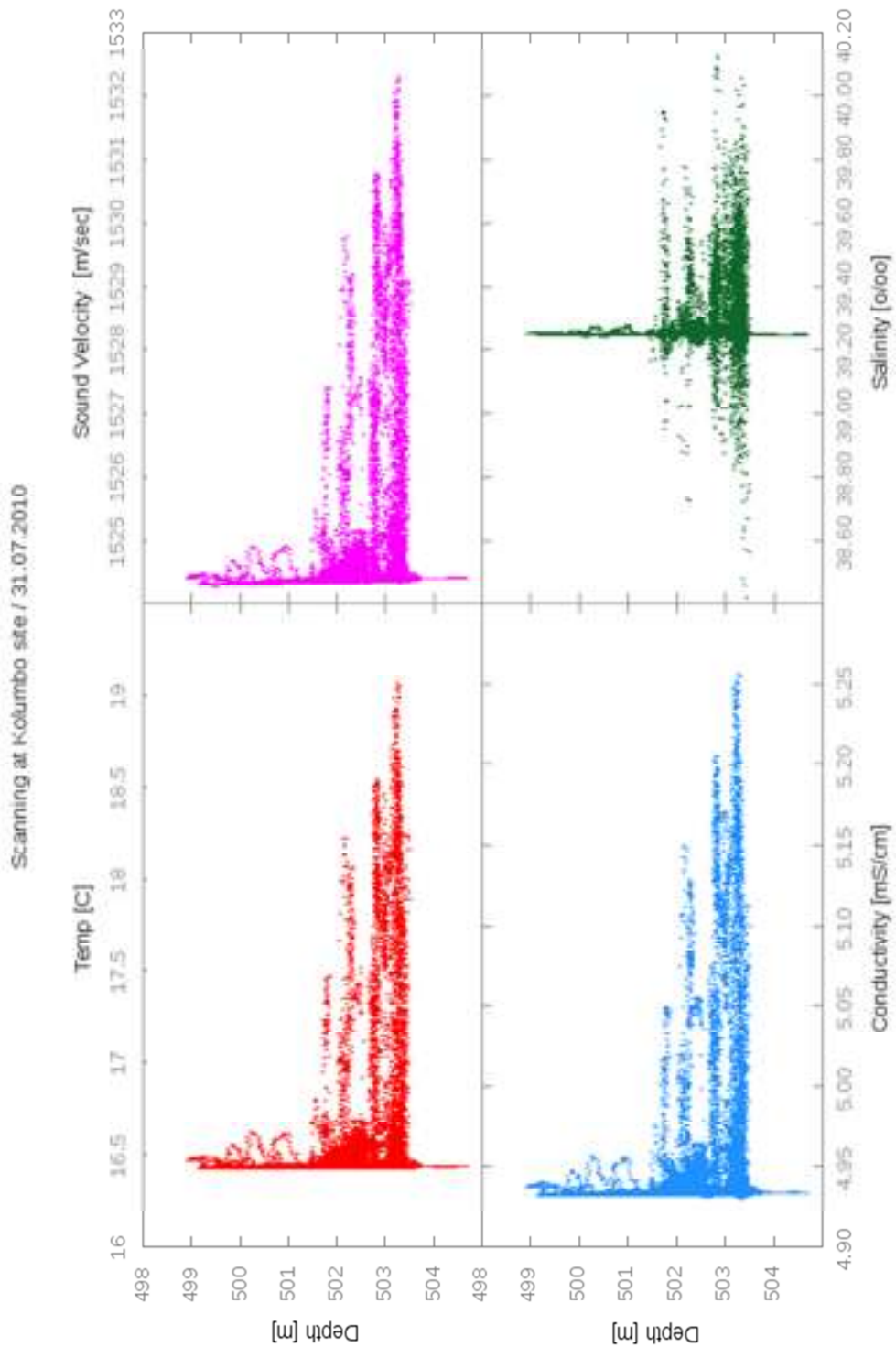


Fig. 5.10 Steep value's increase over the hydrothermal vent field at 501-505 m depth (31/07/2010, 15.00 p.m.). Kolumbo caught in action

DTS 3D map - 31.07.2010 - 15:00

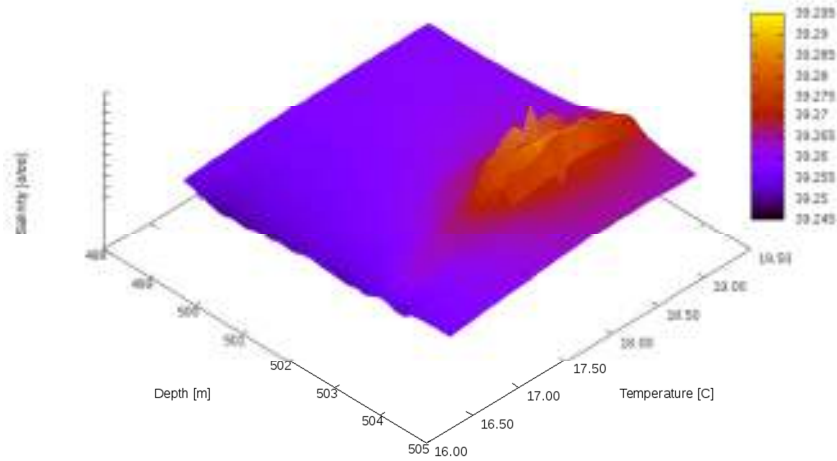


Fig. 5.11 Simultaneous increase of temperature & salinity at a certain depth. Hydrothermal activity is confirmed (31/07/2010, 15.00 p.m.)

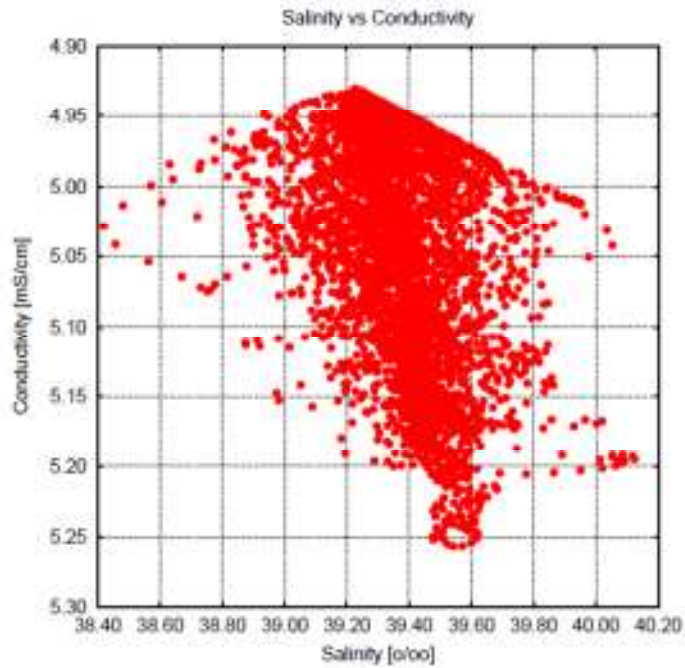
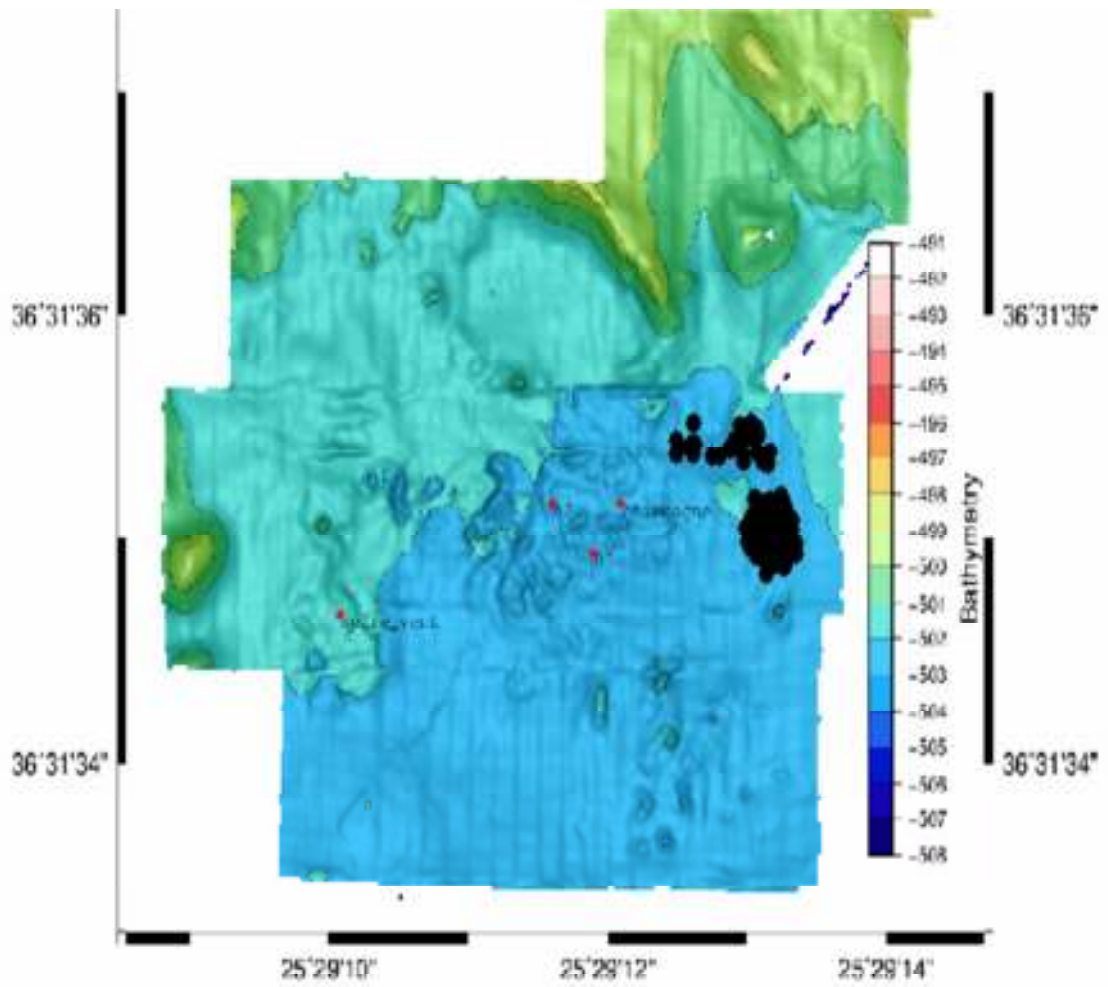


Fig. 5.12 Correlation between salinity & conductivity (31/07/2010, 15.00 p.m.)



*Fig. 5.13 Black dots indicate the sampling locations above the hydrothermal vent field as recorded by ROV Hercules (31/07/2010, 16.00 p.m.)*

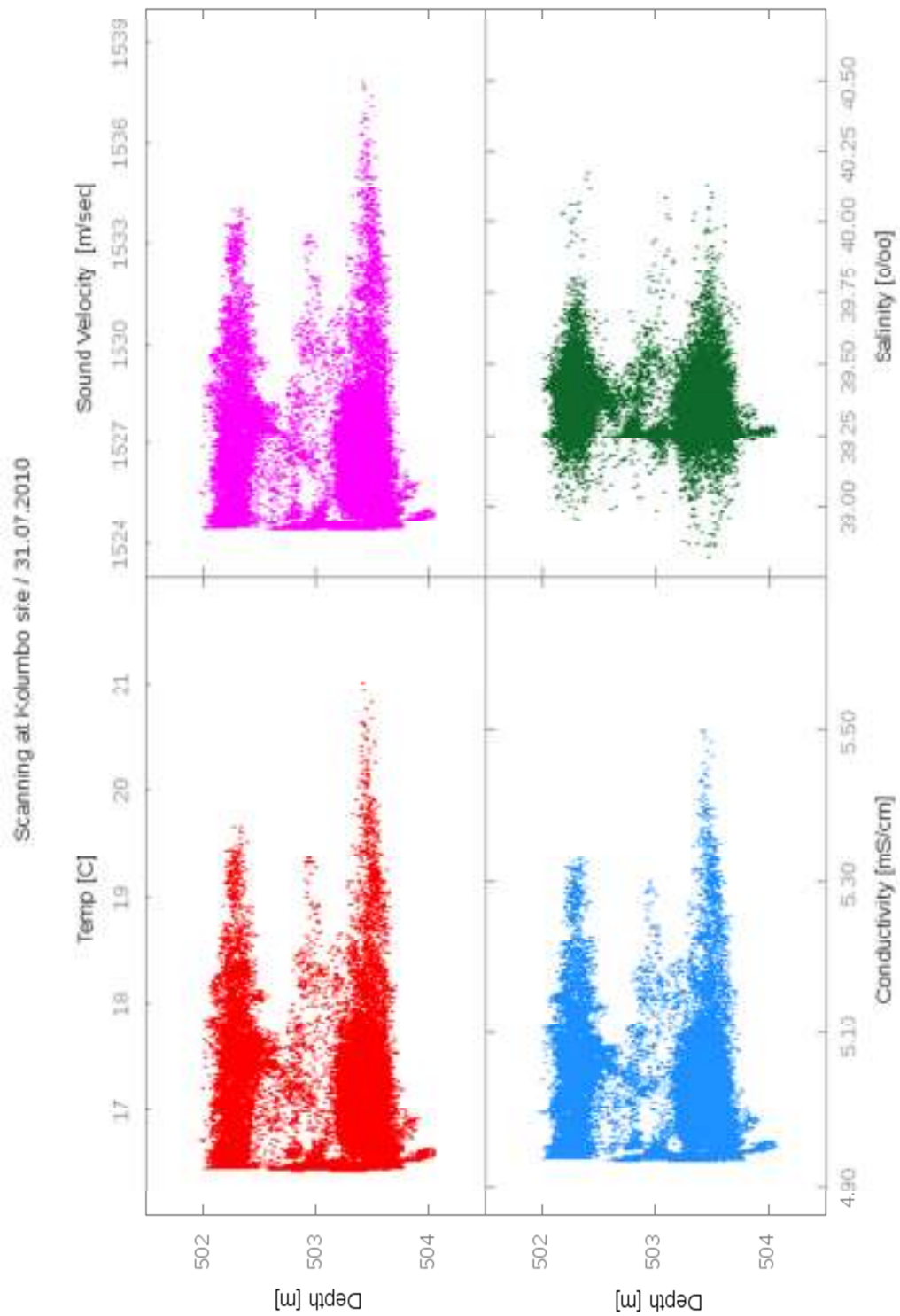


Fig. 5.14 Anomalies on parameters distribution over the hydrothermal vents (31/07/2010 16.00 p.m.)

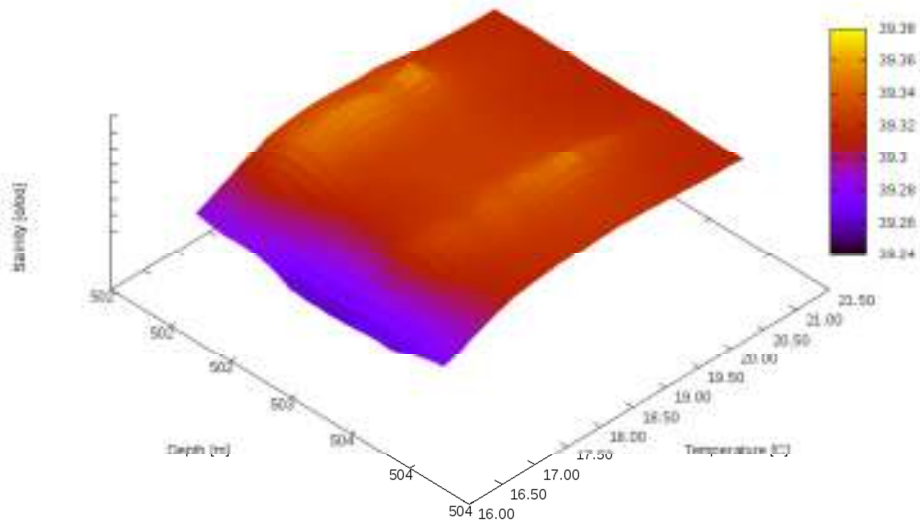


Fig. 5.15 Two bumps in 3D graphic confirm the activity displayed in 5.14 (31/07/2010 16.00 p.m)

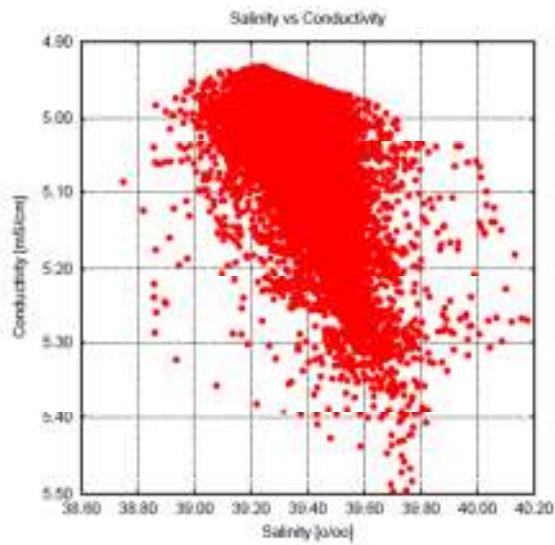
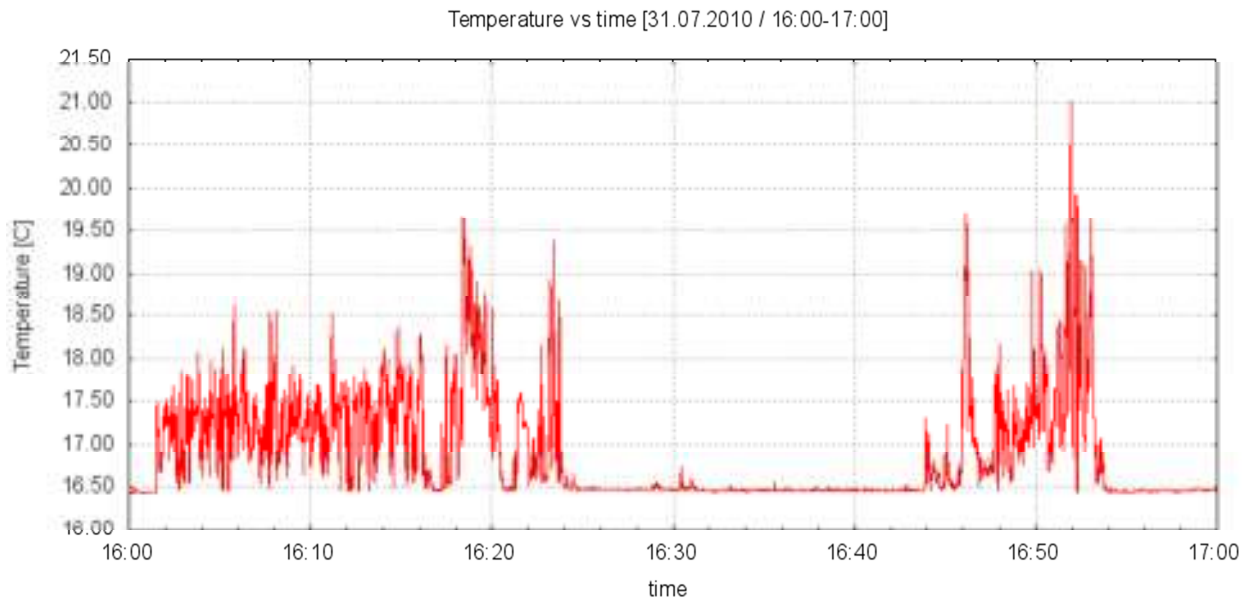
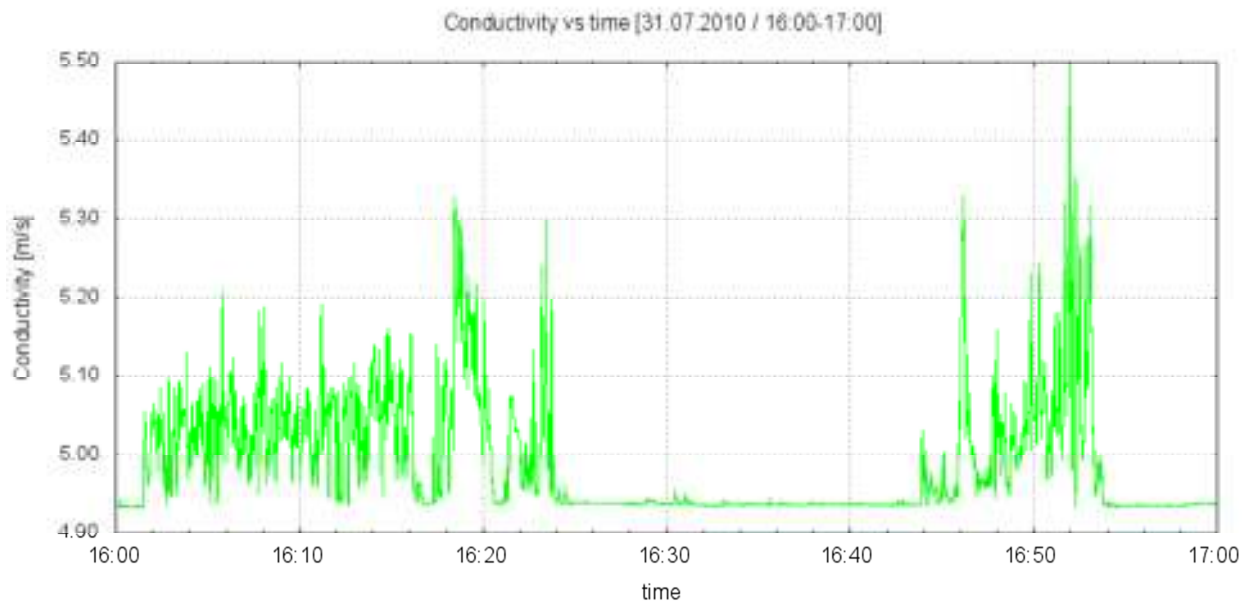


Fig. 5.16 Correlation between salinity & conductivity (31/07/2010, 16.00 p.m.)



*Fig. 5.17 Temperature's variation during one hour over the same spot*



*Fig. 5.18 Conductivity's variation during the same hour over the same spot*

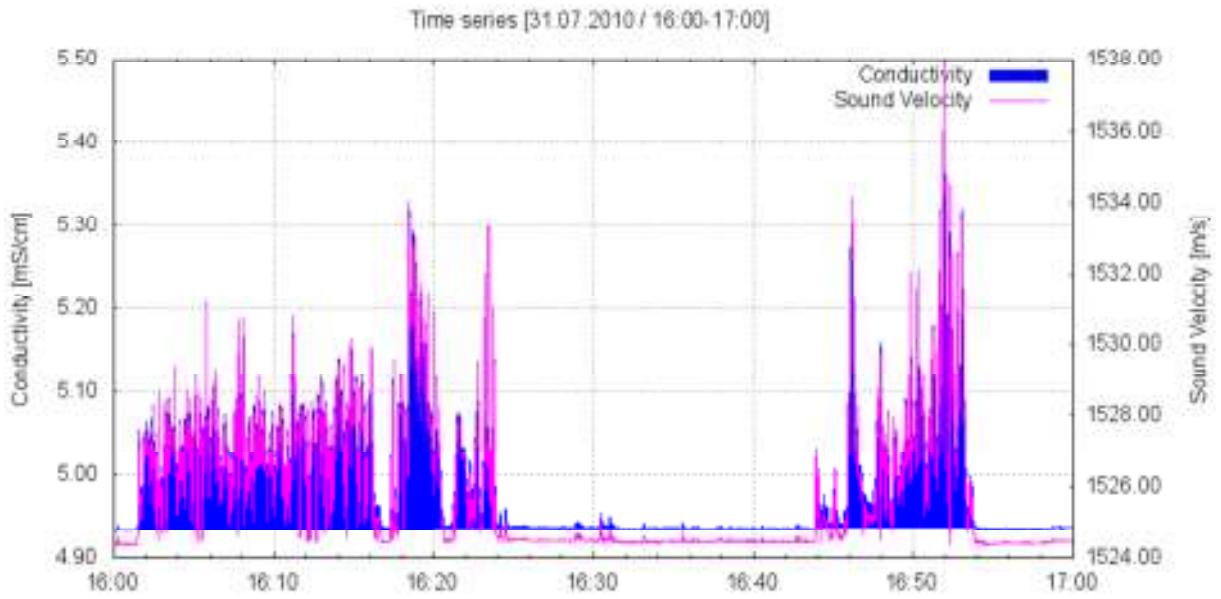


*Fig. 5.19 Conductivity-Sound Velocity correlation during one hour over the same location*

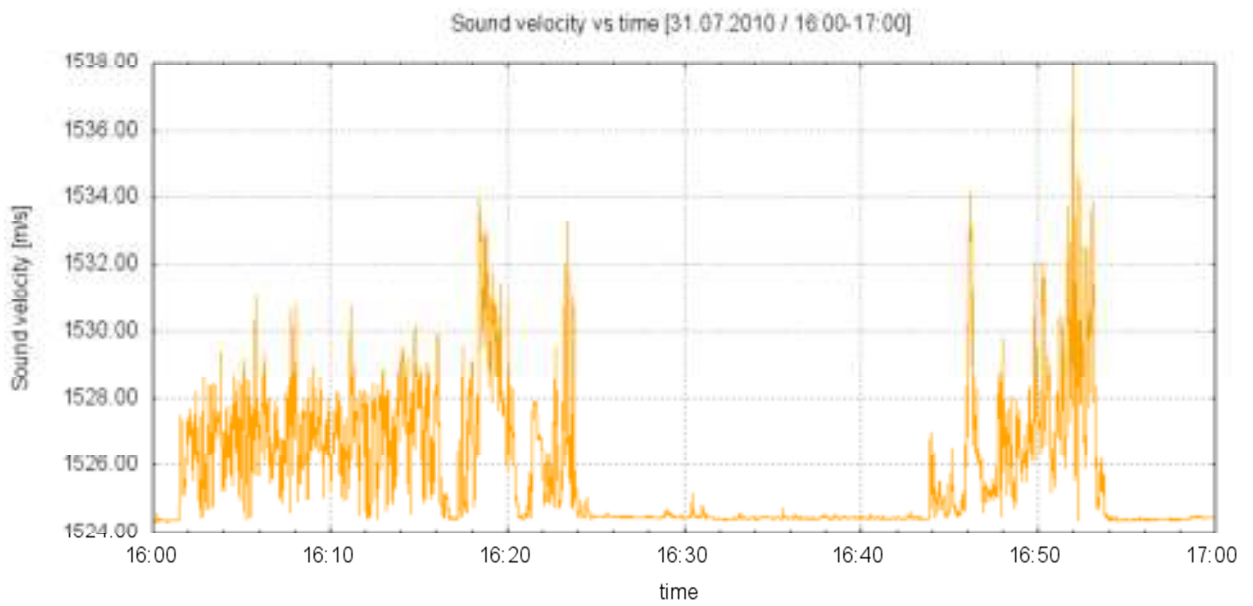


*Fig. 5.20 Sound velocity variation during one hour over the same place*

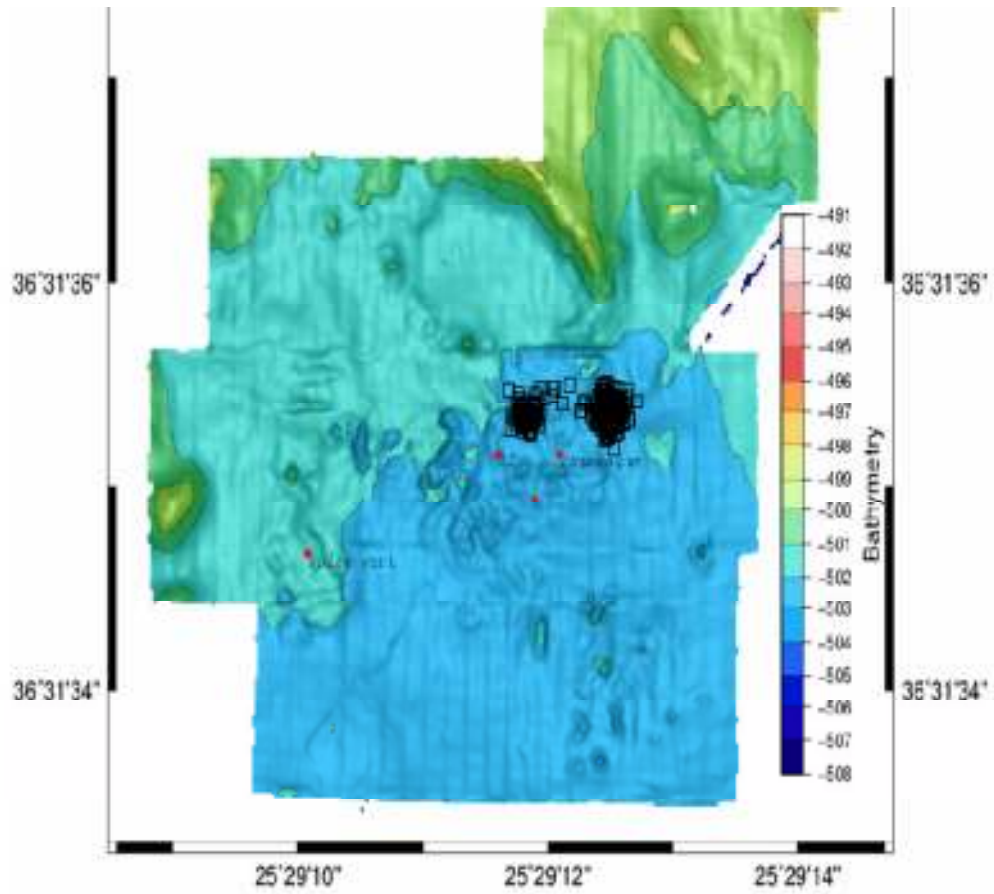


*Fig.5.21 Black dots indicate the sampling locations above the hydrothermal vent field as recorded by ROV Hercules (31/07/2010, 17.00 p.m.)*

Scanning at Kolumbo site / 31.07.2010

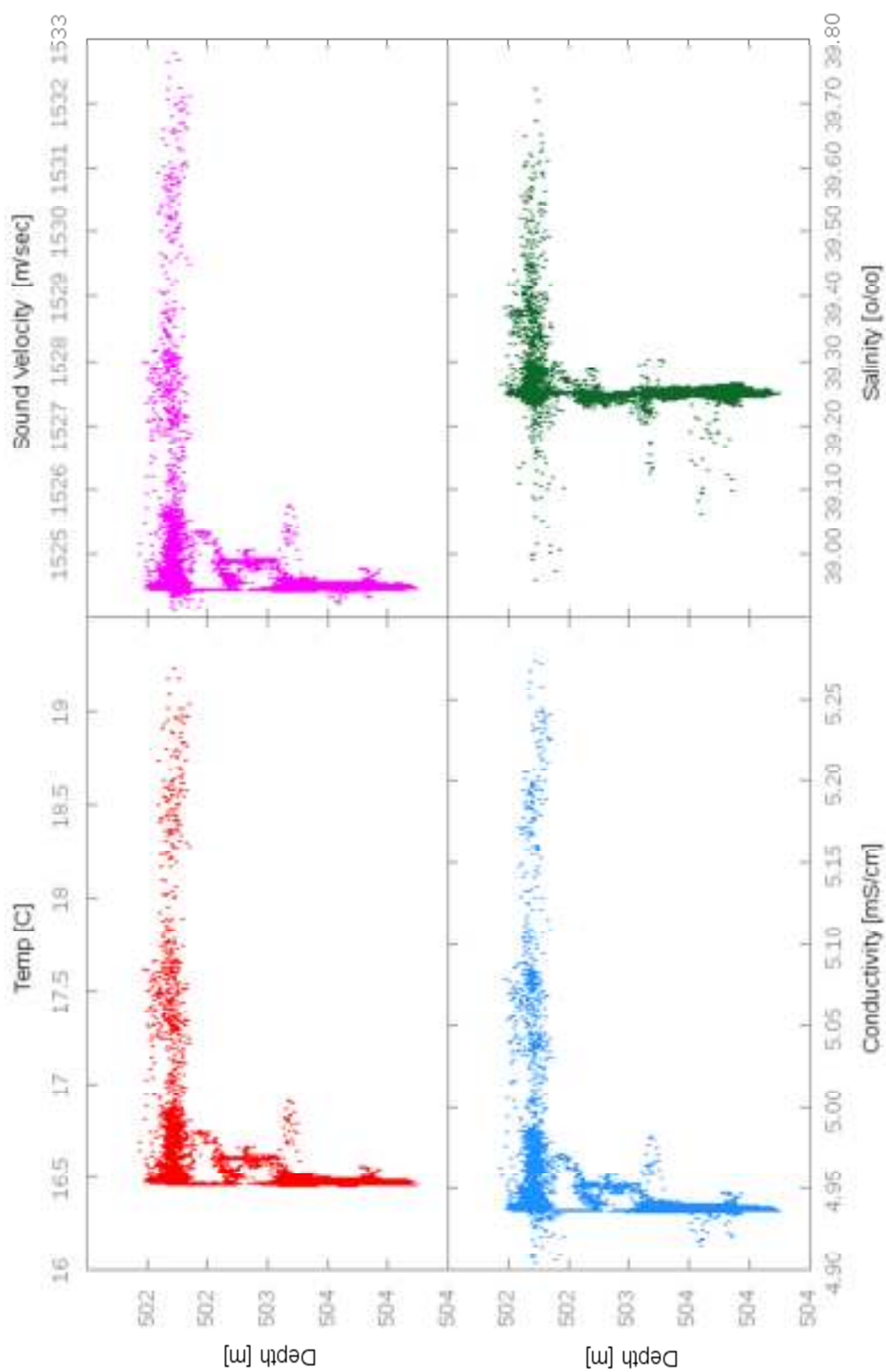


Fig.5.22 Anomalies over the hydrothermal vents (31/07/2010, 17.00 p.m.)

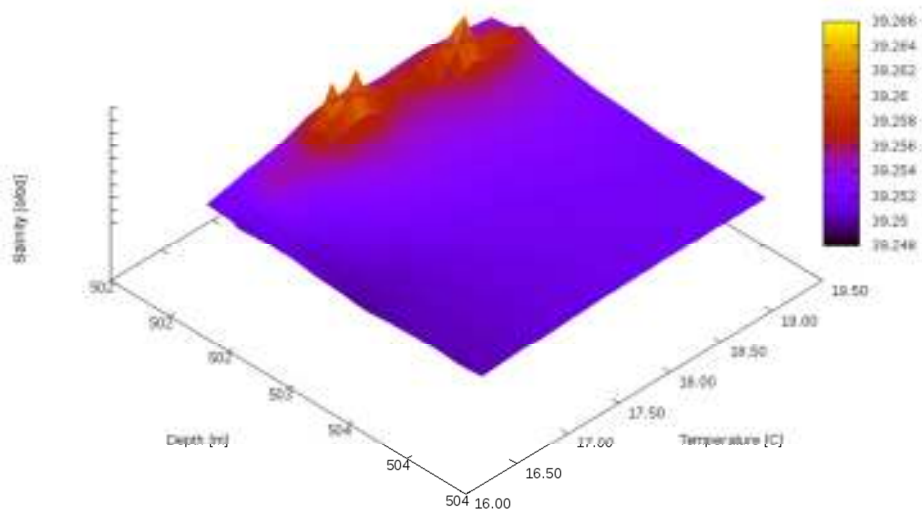


Fig. 5.23 3D correlation of temperature salinity & depth (31/07/2010, 17.00 p.m.)

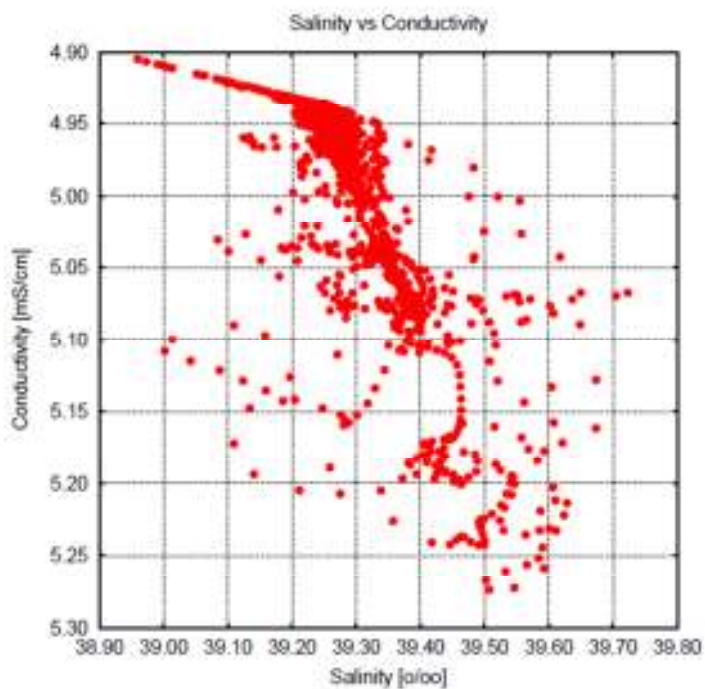
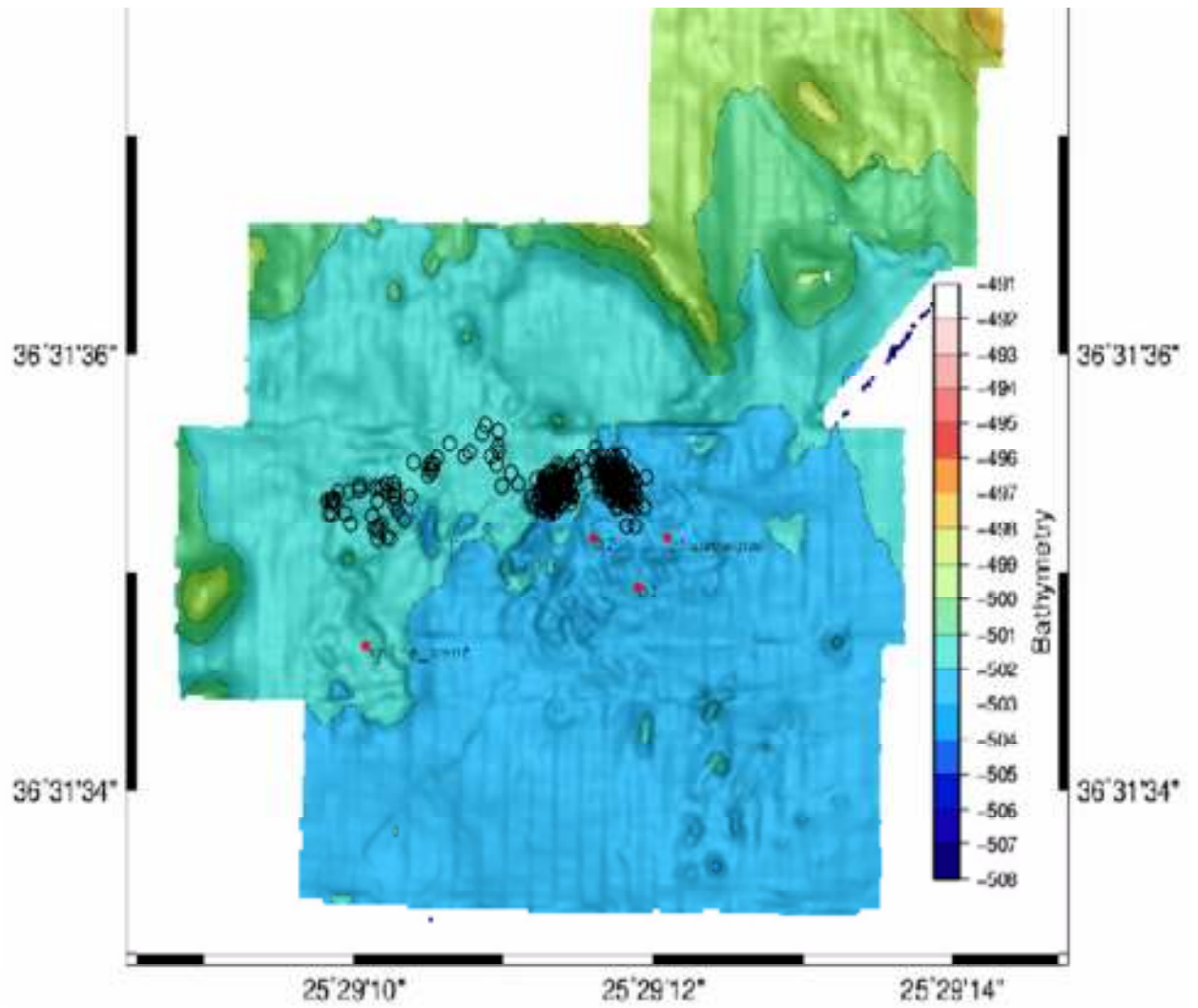


Fig. 5.24 Correlation between salinity & conductivity (31/07/2010, 17.00 p.m.)



*Fig. 5.25 Black dots indicate the sampling locations above the hydrothermal vent field as recorded by ROV Hercules (31/07/2010, 18.00 p.m.)*

Scanning at Kolumbo site / 31.07.2010

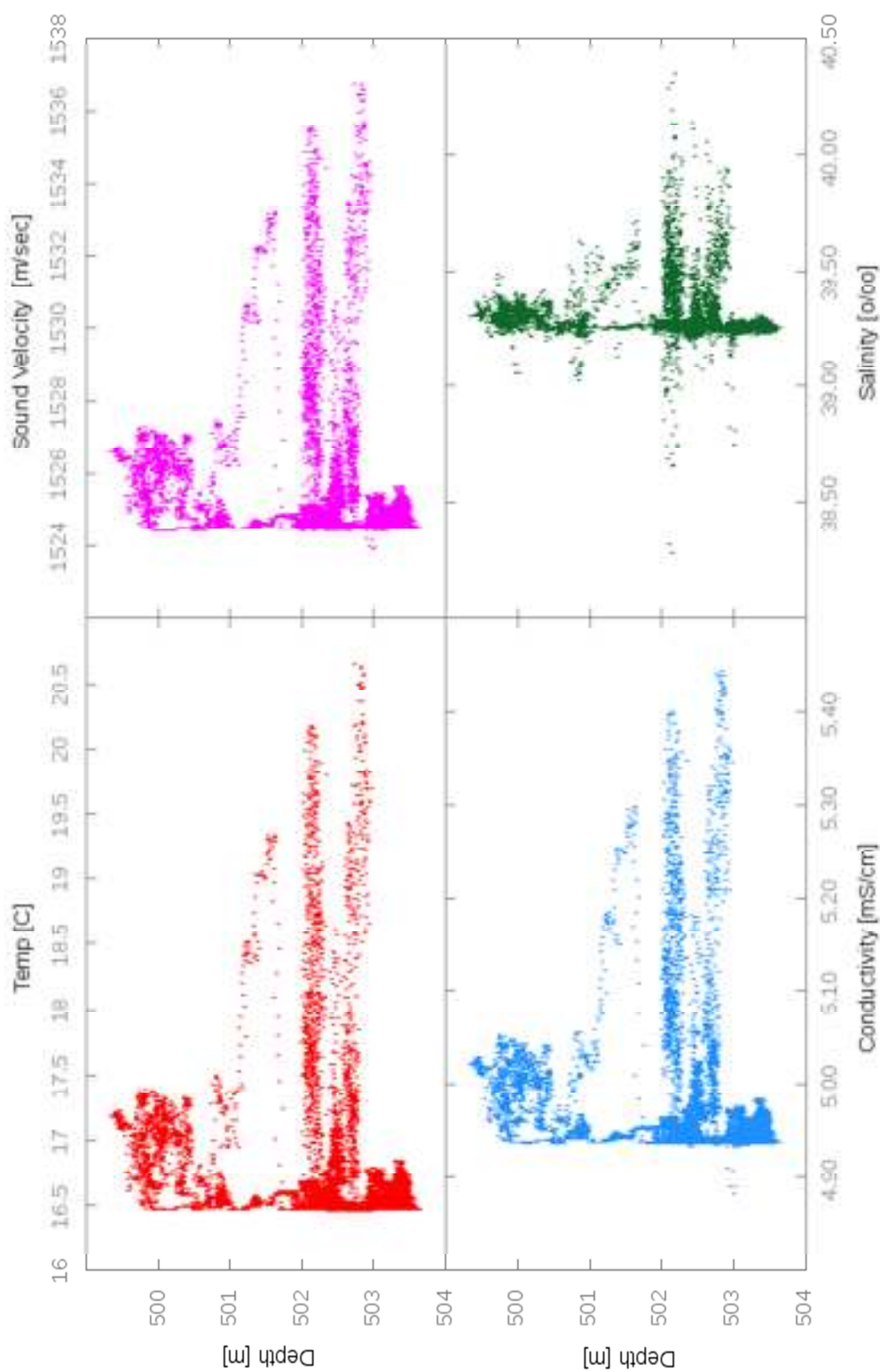


Fig. 5.26 Parameters distribution with the depth (31/07/2010, 18.00 p.m.)

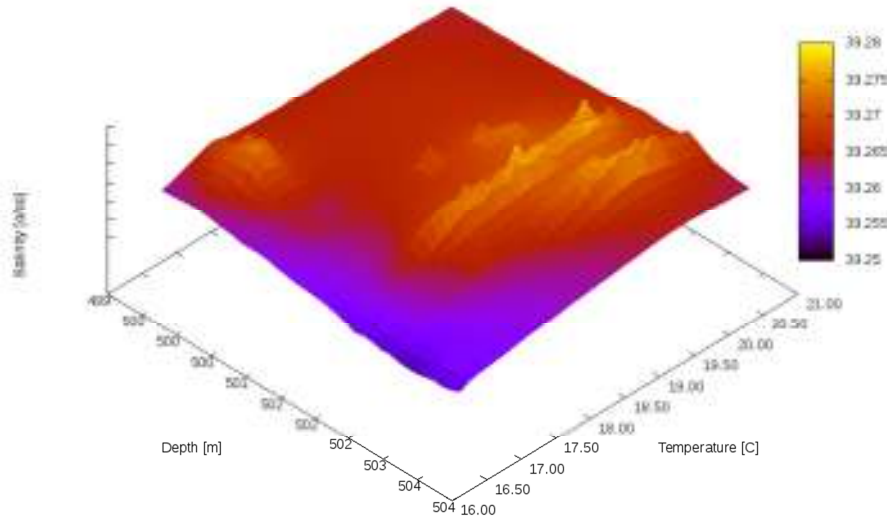


Fig. 5.27 3D correlation of temperature salinity & depth (31/07/2010, 18.00 p.m.)

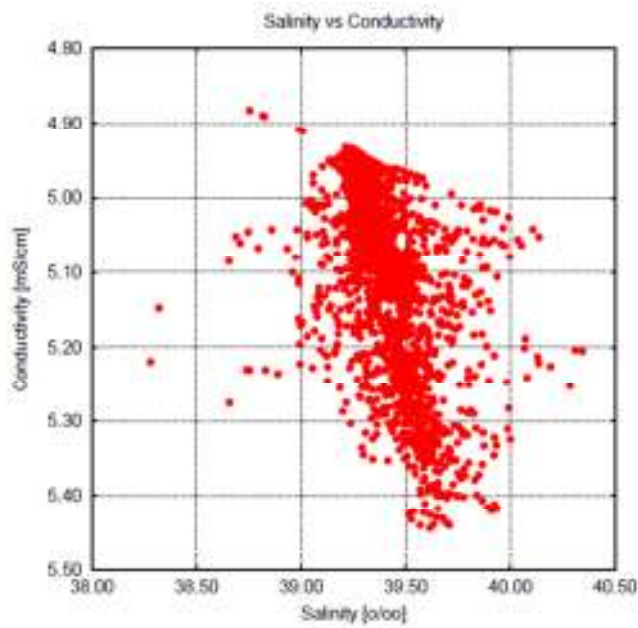
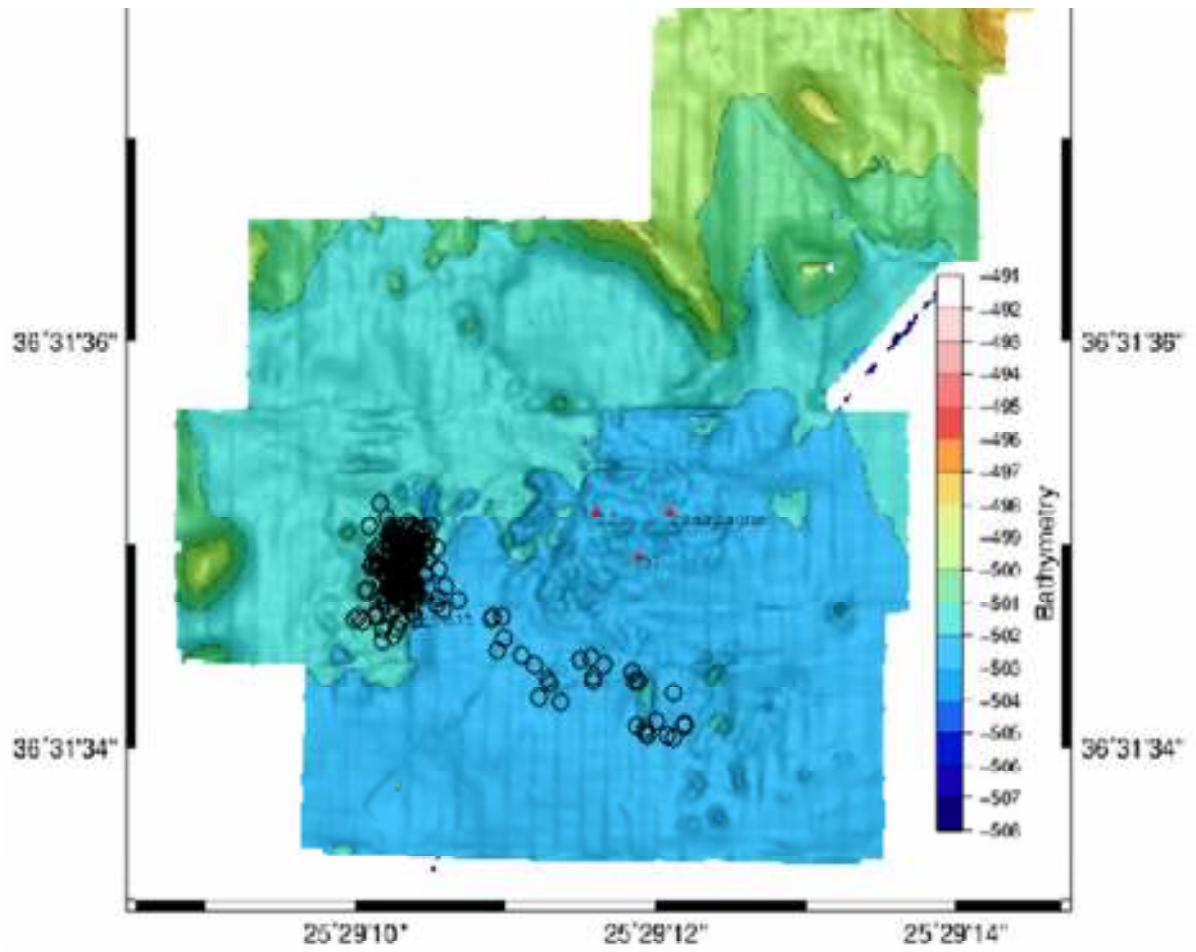


Fig. 5.28 Correlation between salinity & conductivity (31/07/2010, 18.00 p.m.)



*Fig. 5.29 Black dots indicate the sampling locations above the hydrothermal vent field as recorded by ROV Hercules (31/07/2010, 19.00 p.m.)*

Scanning at Kolumbo site / 31.07.2010

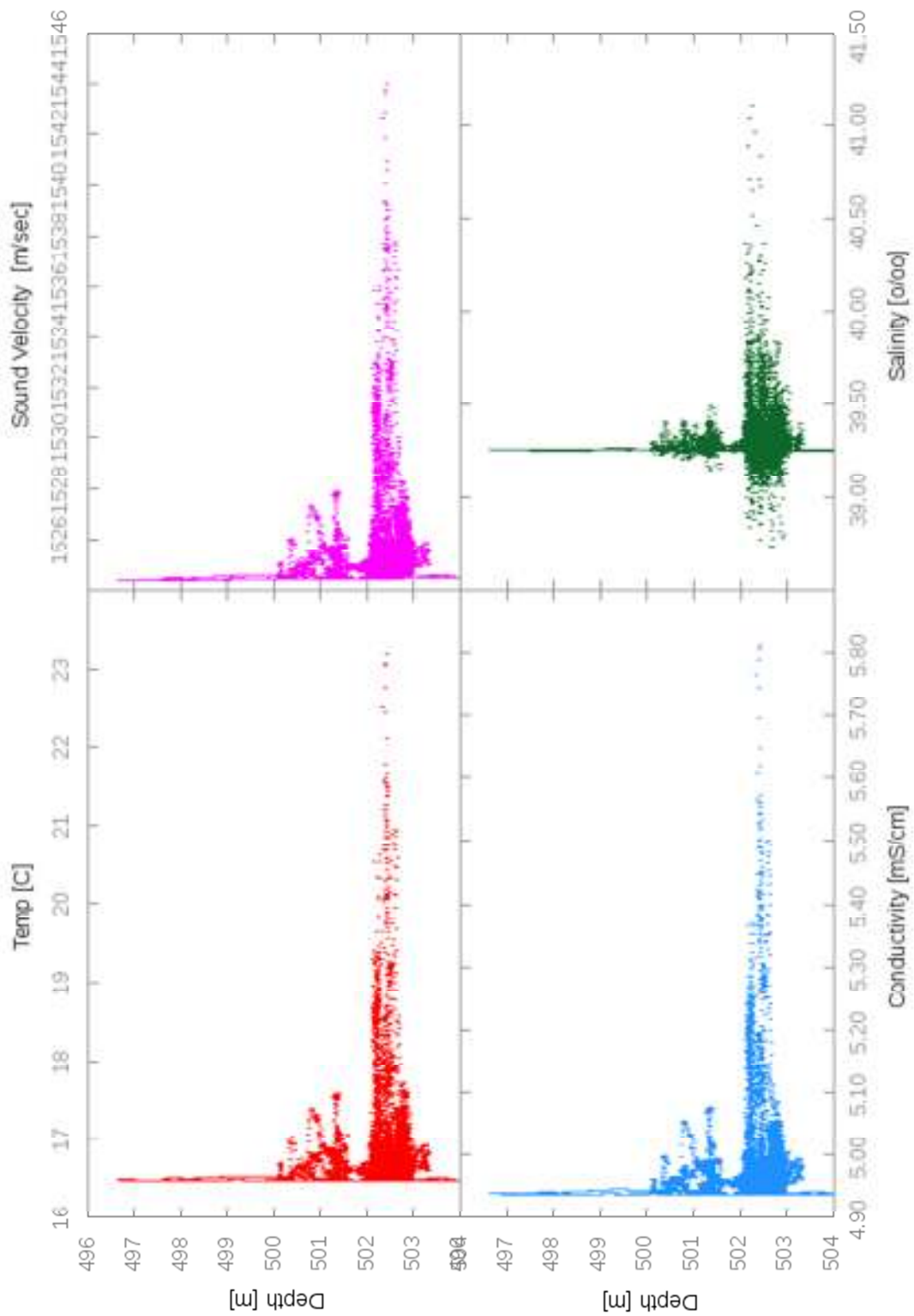


Fig. 5.30 Parameters distribution with the depth (31/07/2010, 19.00 p.m.)

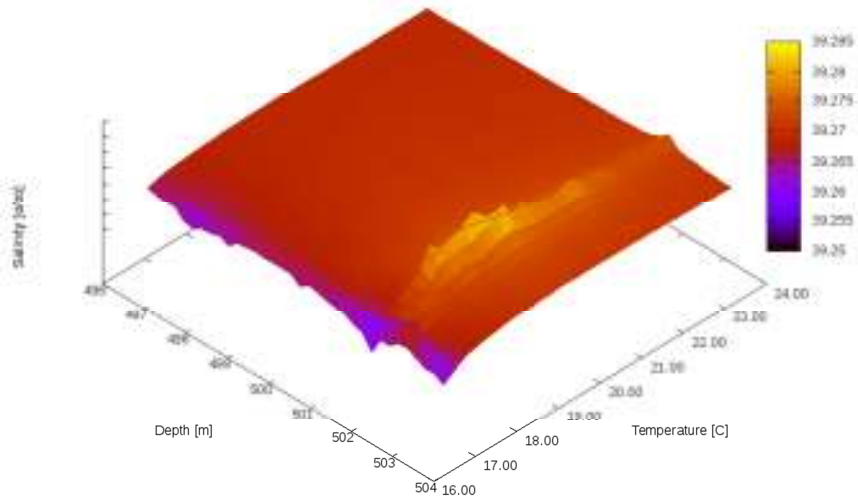


Fig. 5.31 3D correlation of temperature salinity & depth (31/07/2010, 19.00 p.m.)

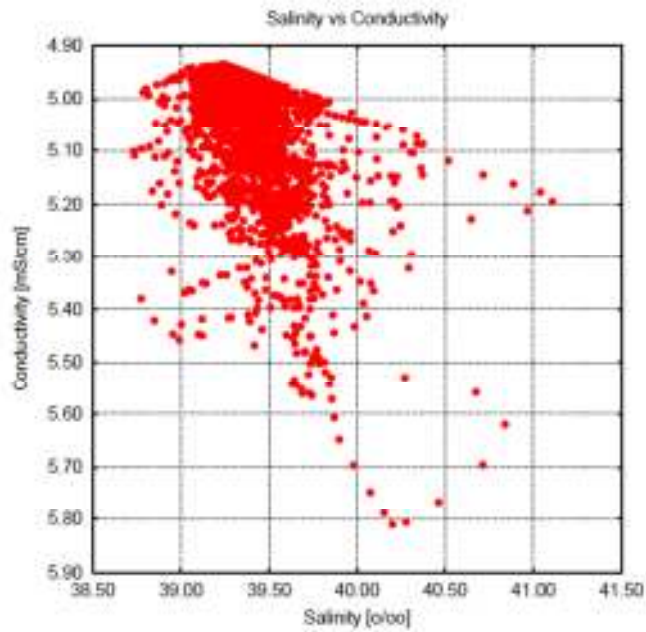
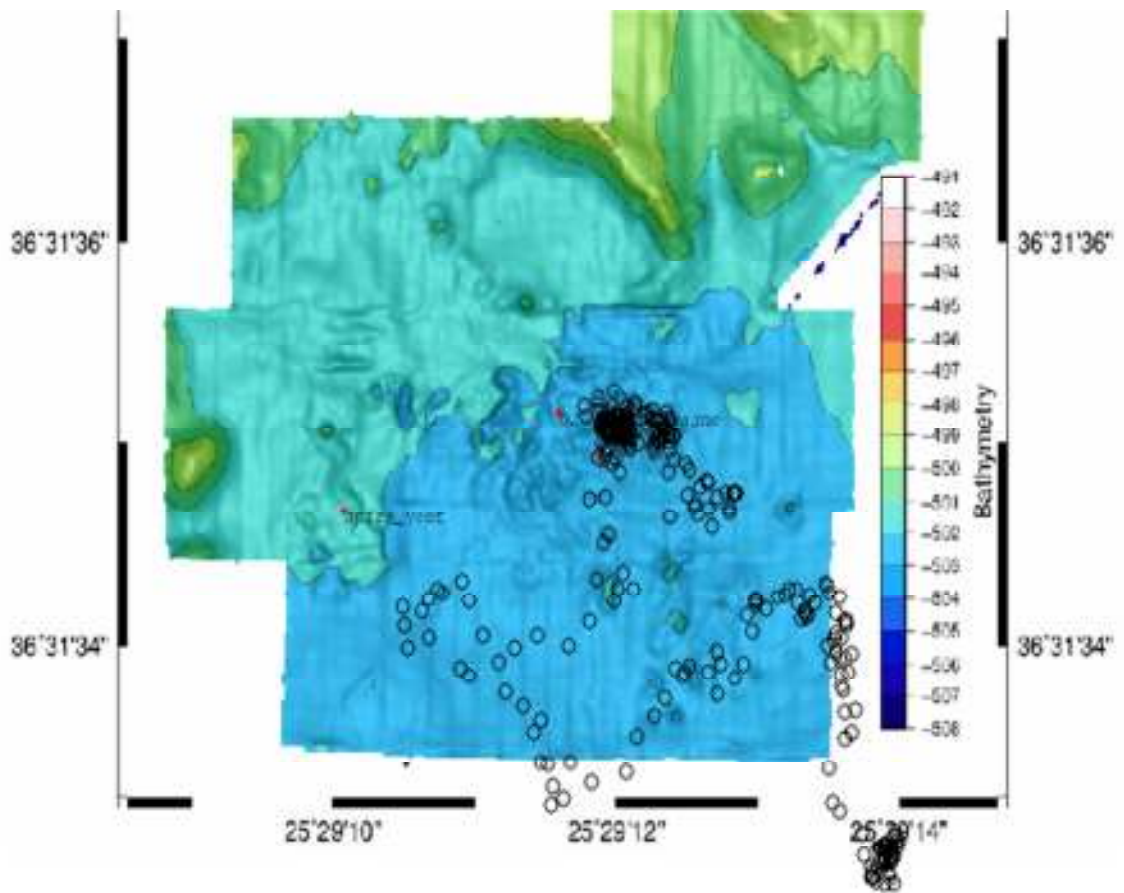


Fig. 5.32 Correlation between salinity & conductivity (31/07/2010, 19.00)



*Fig. 5.33 Black dots indicate the sampling locations above the hydrothermal vent field as recorded by ROV Hercules (31/07/2010, 20.00 p.m.)*

Scanning at Kolumbo site / 31.07.2010

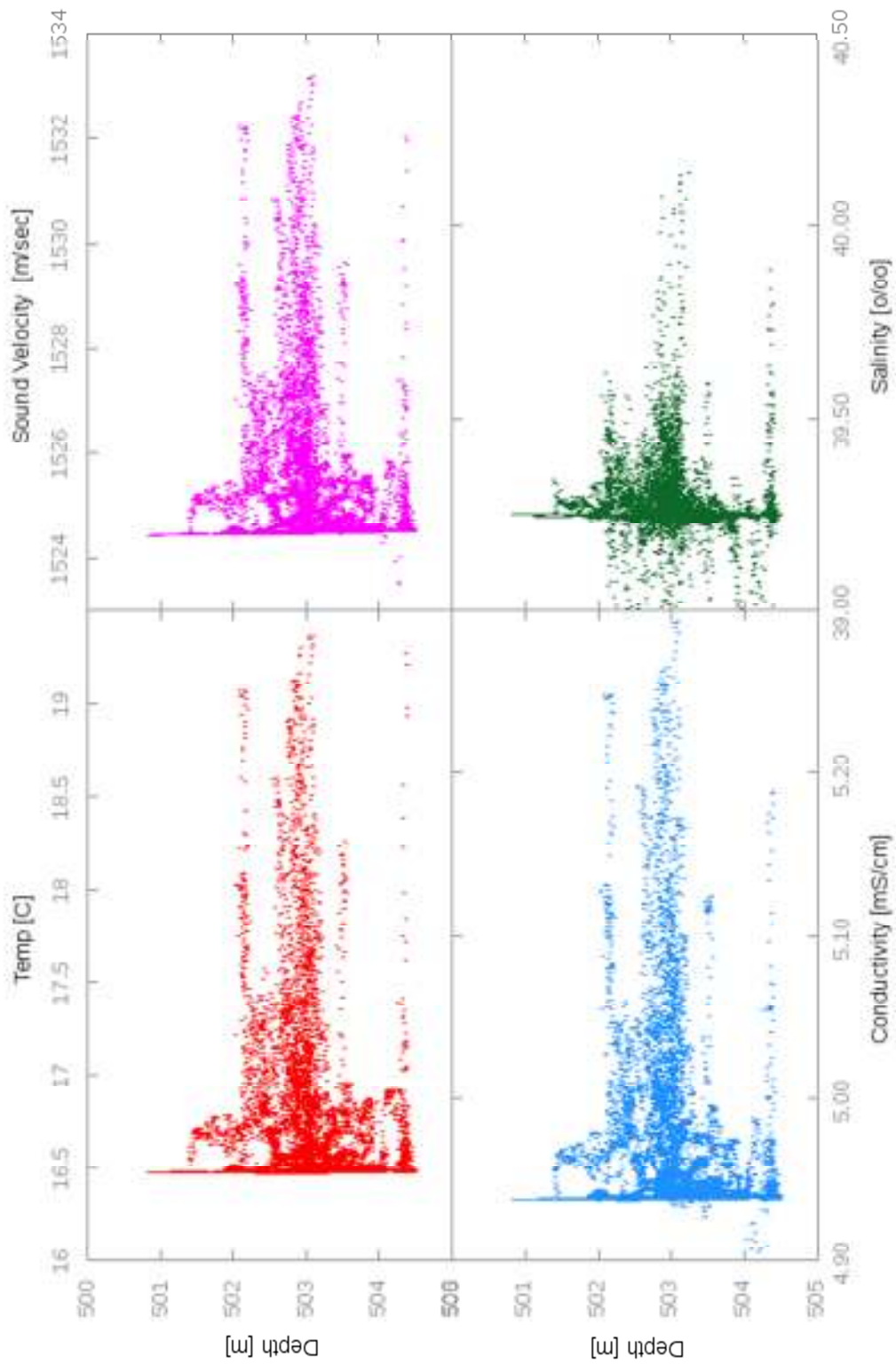


Fig. 5.34 Parameters anomalies over the hydrothermal vent field (31/07/2010, 20.00 p.m.)

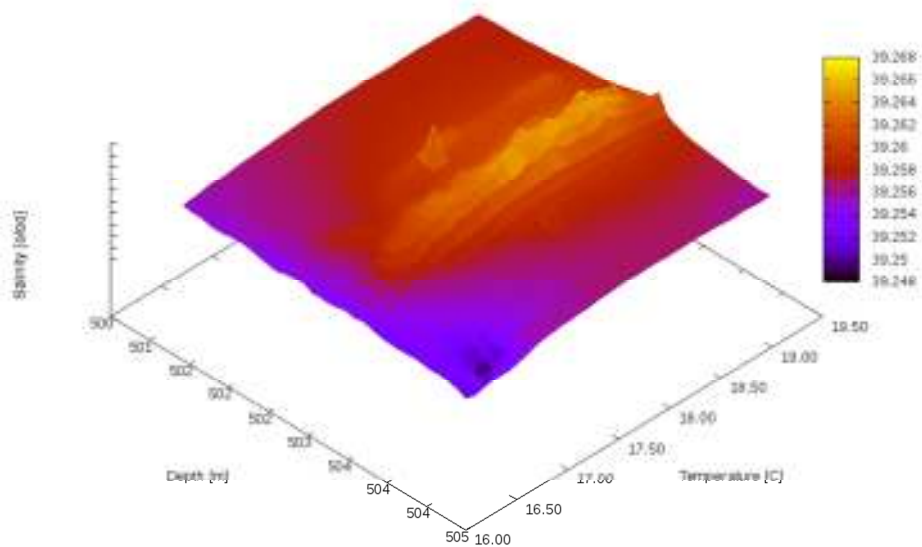


Fig. 5.35 3D correlation of temperature salinity & depth (31/07/2010, 20.00 p.m.)

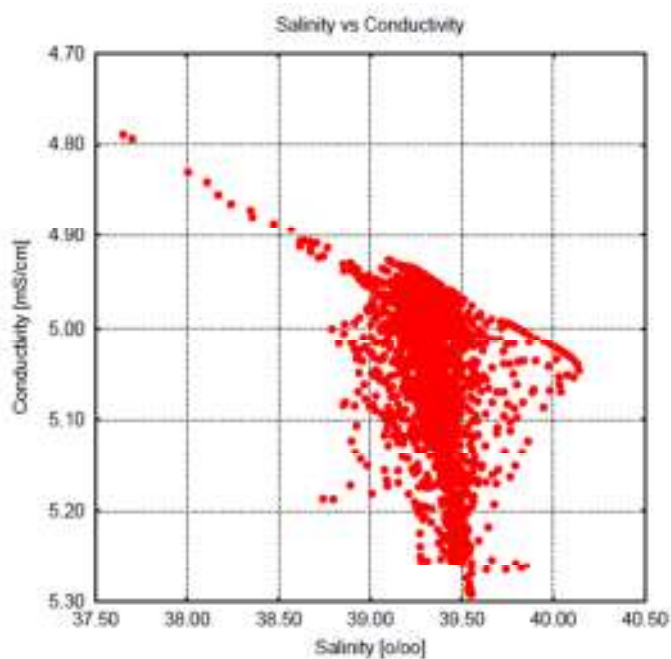
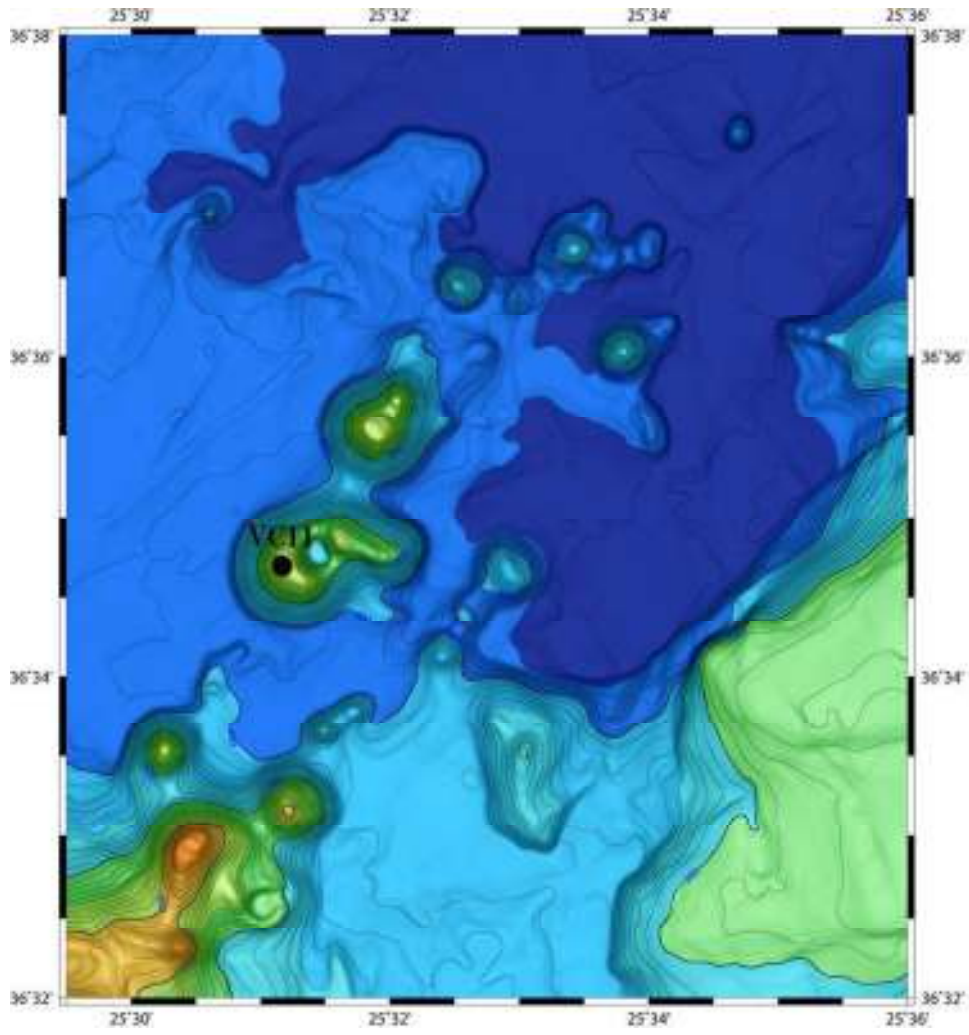


Fig. 5.36 Correlation between salinity & conductivity (31/07/2010, 20.00 p.m.)



*Fig. 5.37 Cones extending NE of Kolumbo where measurements have been conducted*

Scanning at Kolumbo sire / 01.08.2010

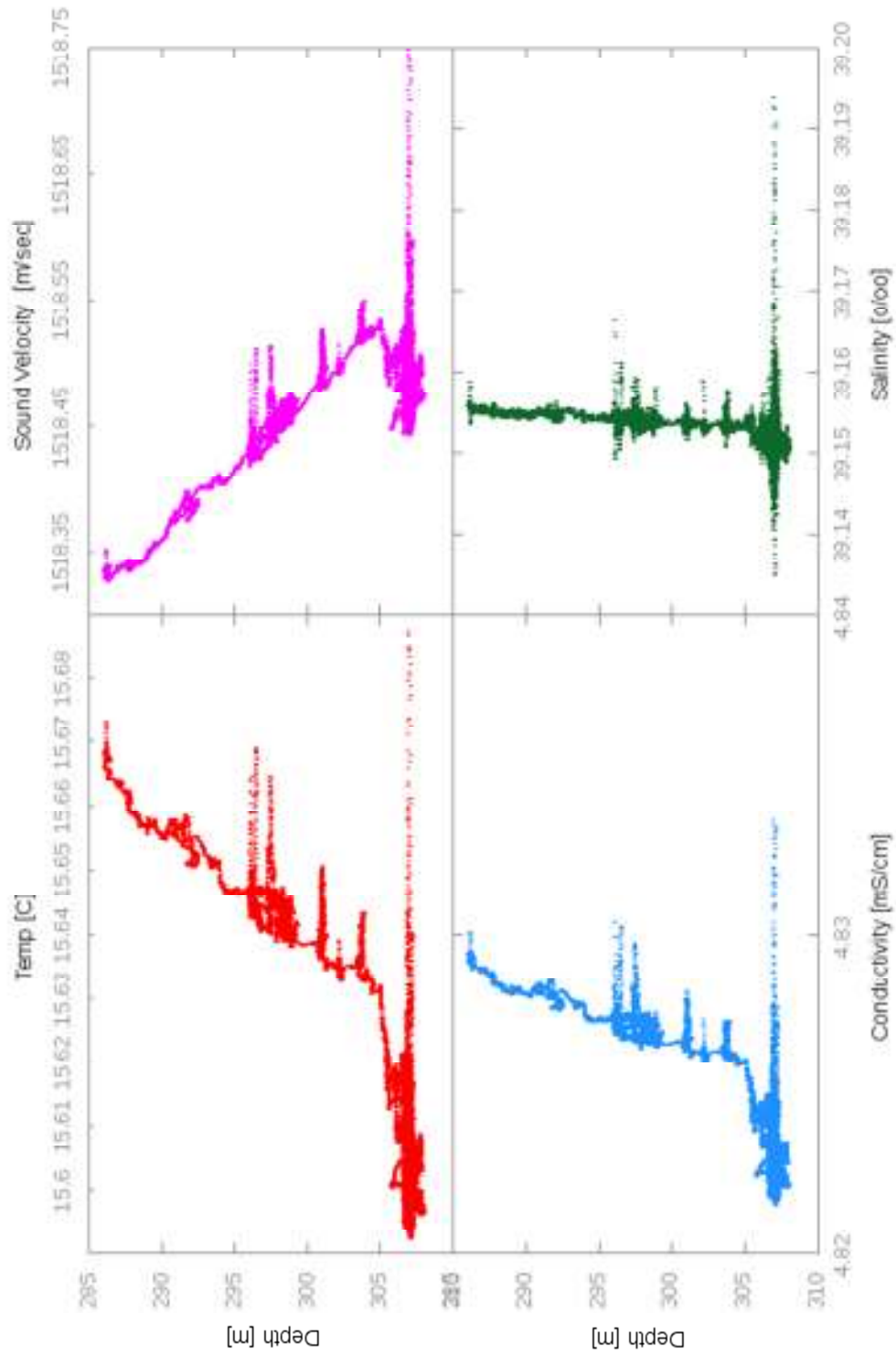


Fig. 5.38 Parameters distribution with the depth at VC11 (01/08/2010, 03.00)

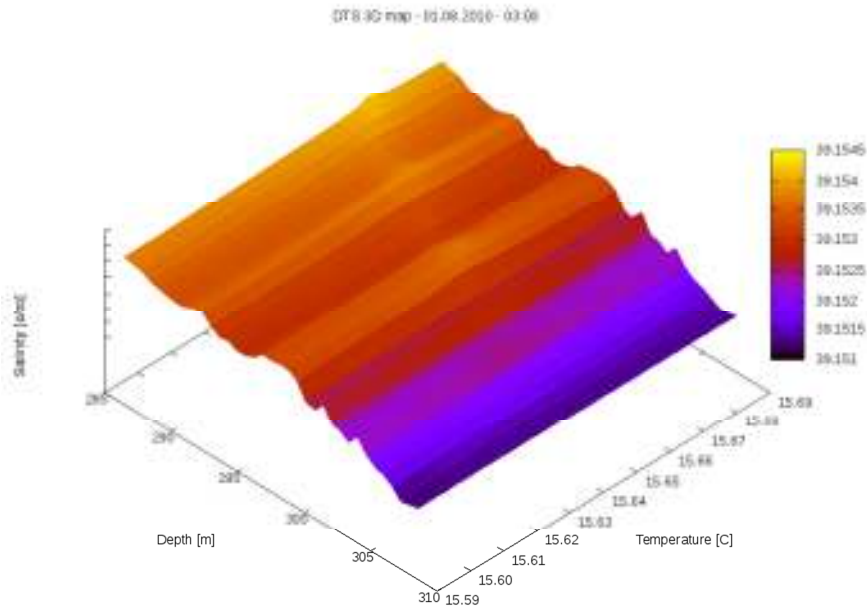


Fig. 5.39 3D correlation of temperature salinity & depth at VC11 (01/08/2010 03.00 a.m.)

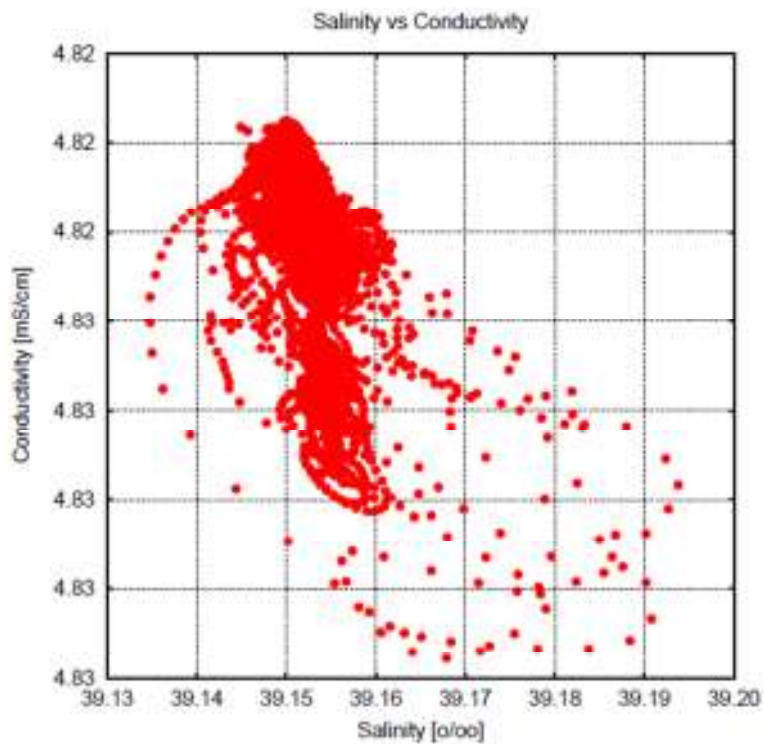
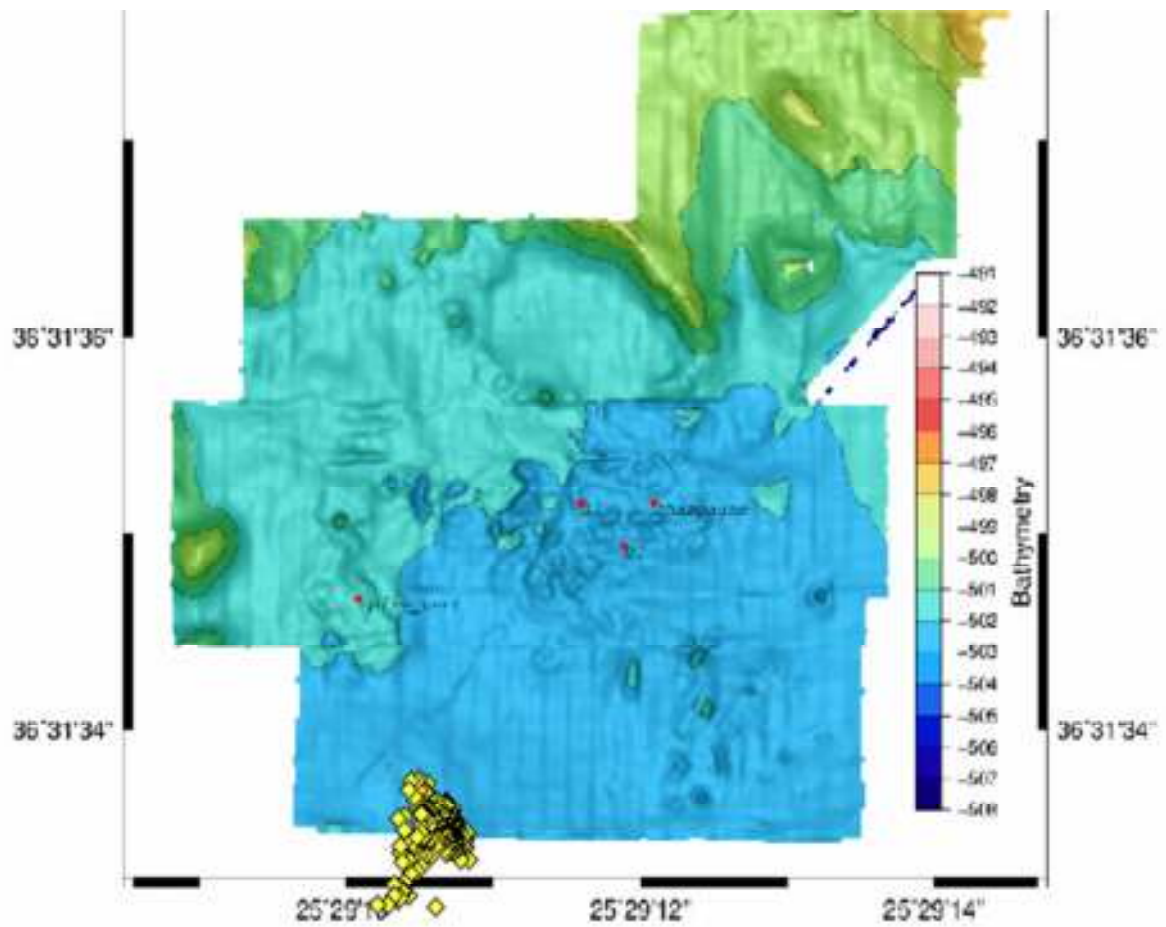


Fig. 5.40 Correlation of salinity & conductivity (01/08/2010, 03.00 a.m.)

## 5.2 NA011 RESULTS



*Fig. 5.41 Yellow dots indicate the sampling locations above the hydrothermal vent field as recorded by ROV Hercules (03/10/2010, 20.00 p.m.)*

Scanning at Kolumbo site / 03.10.2010

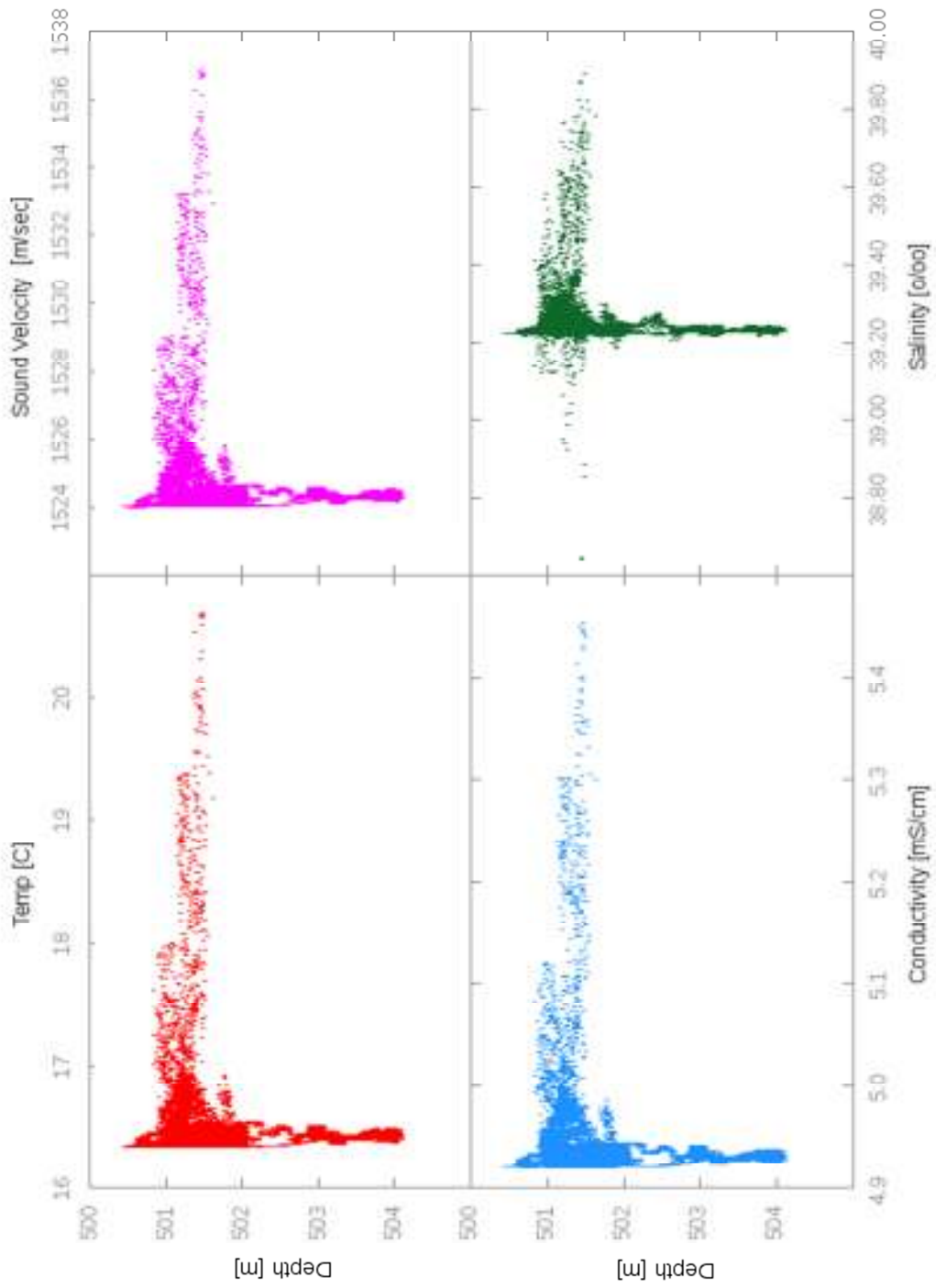


Fig. 5.42 Parameters anomalies over the hydrothermal vents (03/10/2010, 20.00 p.m.)

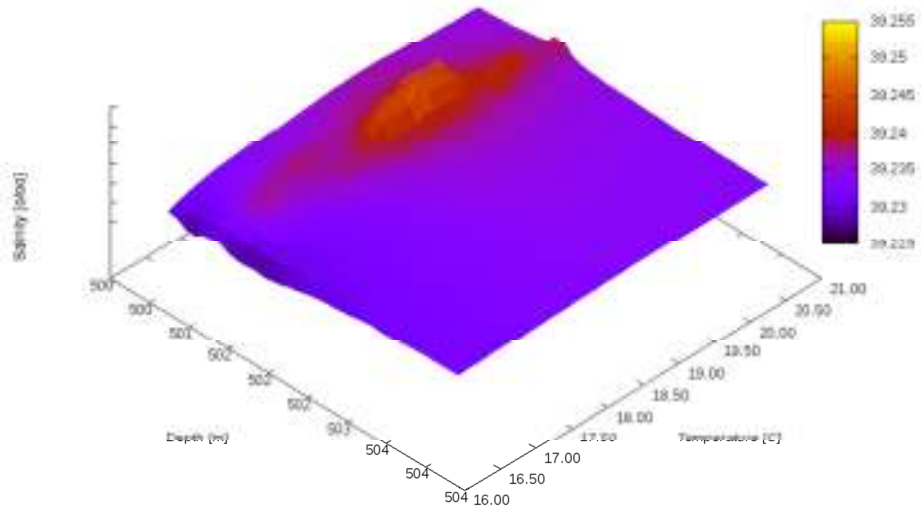


Fig. 5.43 3D correlation of temperature salinity & depth (03/10/2010, 20.00 p.m.)

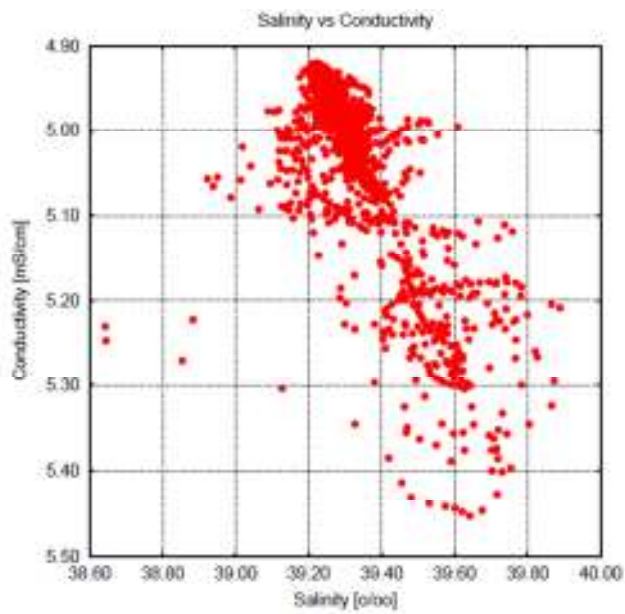
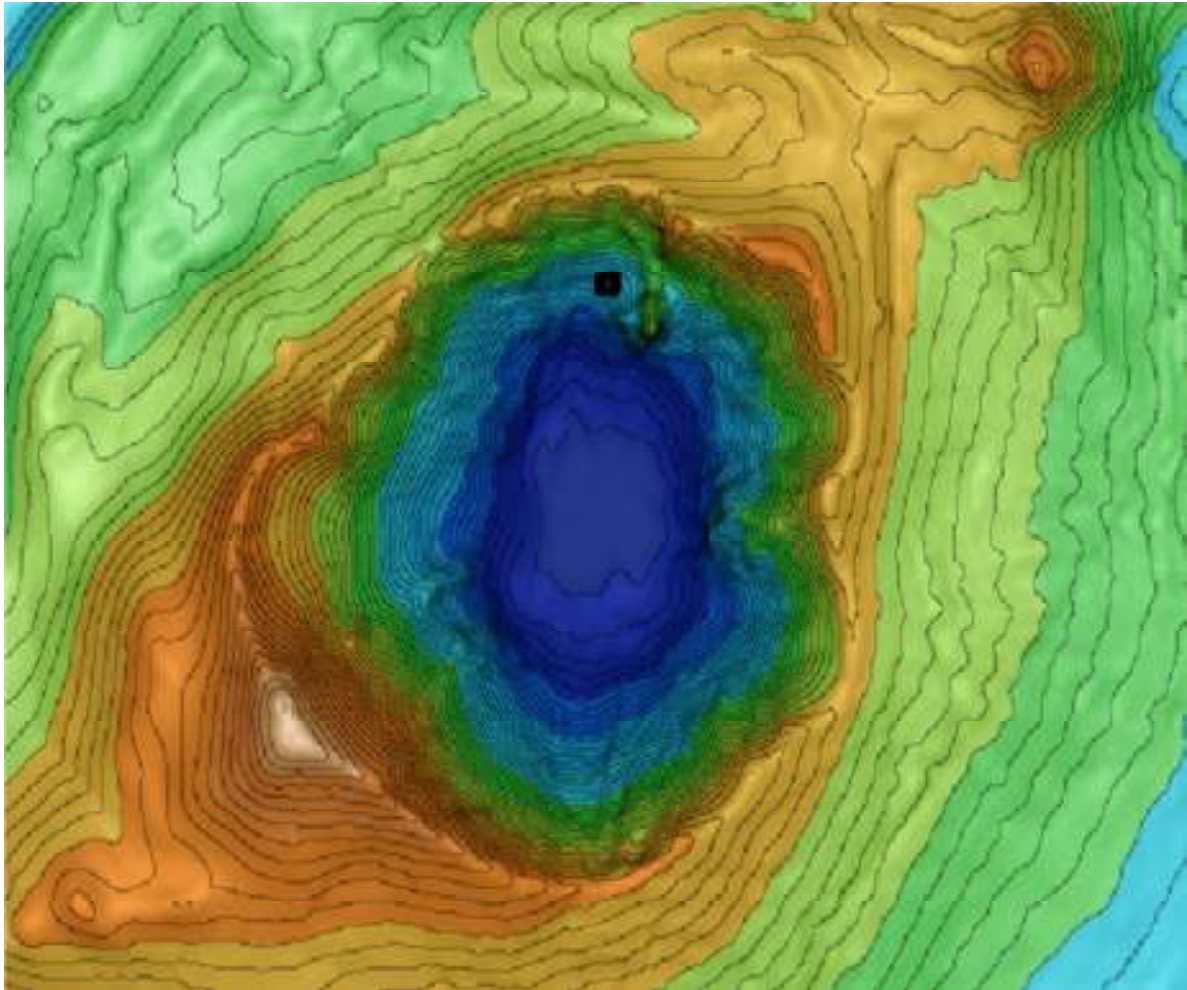


Fig. 5.44 Correlation between salinity & conductivity (03/10/2010, 20.00 p.m.)

### 5.3 NA014 RESULTS



*Fig. 5.45 Location of measurements during the NA014 cruise at the northern part of the hydrothermal vent field*

Scanning at Kolumbo site / 01.09.2011

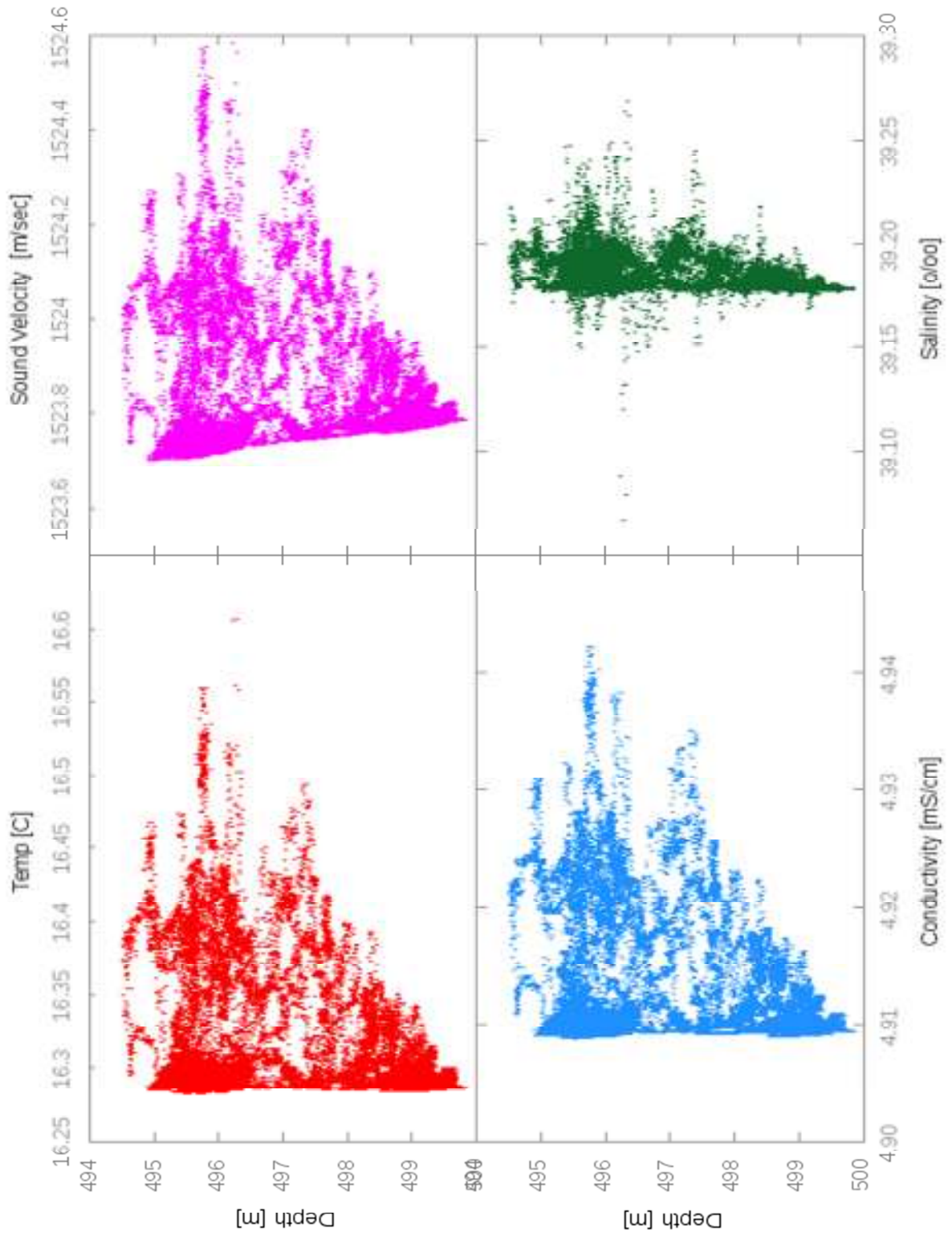


Fig. 5.46 Parameters distribution with the depth (01/09/2011, 20.00 p.m.)

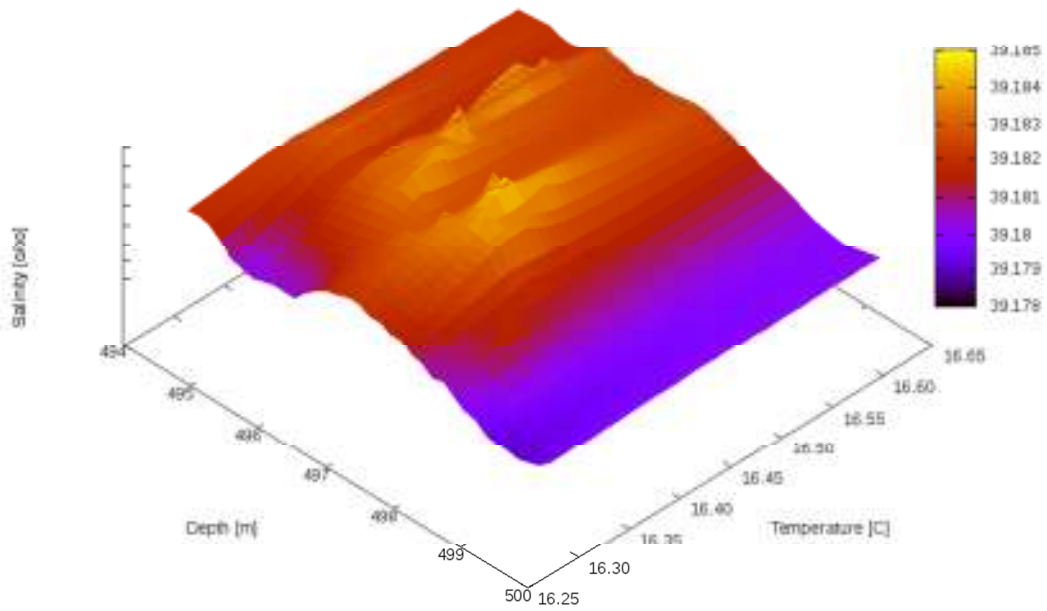


Fig. 5.47 3D correlation of temperature salinity & depth (01/09/2011, 20.00 p.m.)

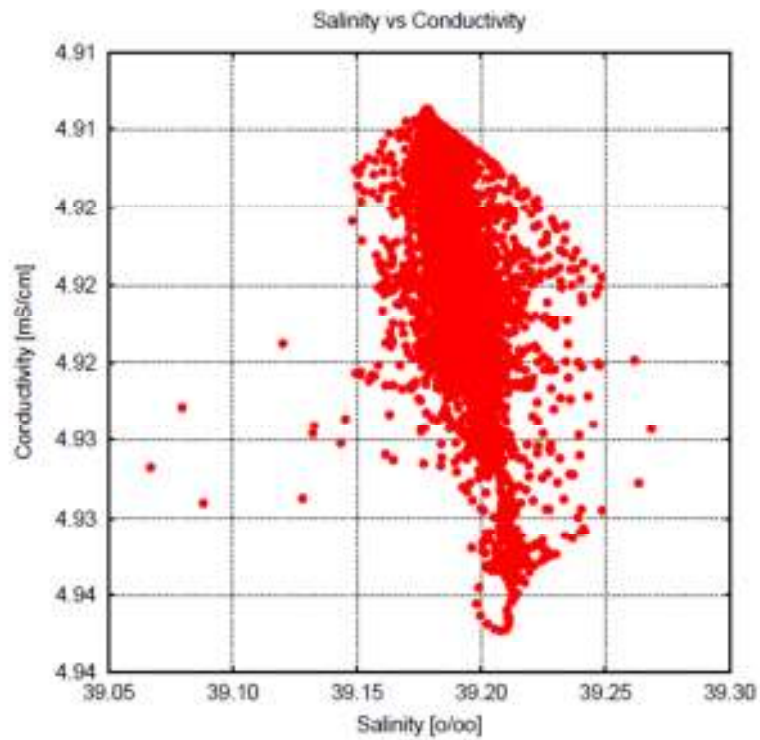
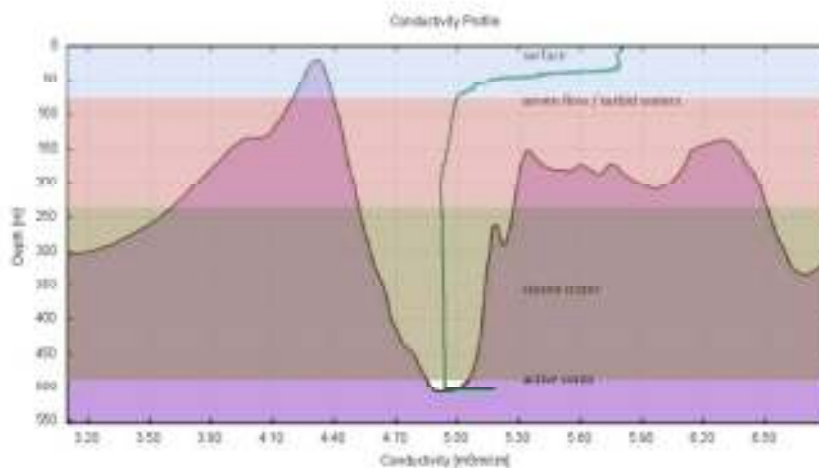


Fig. 5.48 Correlation between salinity & conductivity (01/09/11, 20.00 p.m.)

## 5.4 CORRELATION MORPHOLOGY-VERTICAL PARAMETERS DISTRIBUTION

Following plotting of the physicochemical parameters depth distributions, a visual inspection suggest a strong correlation between each one of them and the cone's morphology. Thus, four distinct zones of the cone were identified that correspond to the variation of seawater parameters. In the profiles below, the relationship between the cone's morphology and the parameter's distribution is presented and the four zones are depicted by different colors. The light blue zone extends from the surface to about 80 m and corresponds to the open sea conditions (thermocline). The pink zone extends from 80 m to about 230 m, where a turbid flow is observed. Turbidity is due to the height difference between the shallowest and the deeper rim of the crater that induces a gradient in normal water flow. The light brown zone extends from 230 m to about 497 m; the profile seems to be constant due to the undisturbed, almost isolated environment of the crater. The white zone, finally, extends from 497 m to 504 m, where the activity of the hydrothermal vent field causes all parameters to present an anomaly simultaneously.



*Fig. 5.49 Vertical profile Depth-Conductivity; Four distinct zones in the cone (1: 0-80 m, 2: 80-230 m, 3: 230-497 m, 4:497 m504m)*

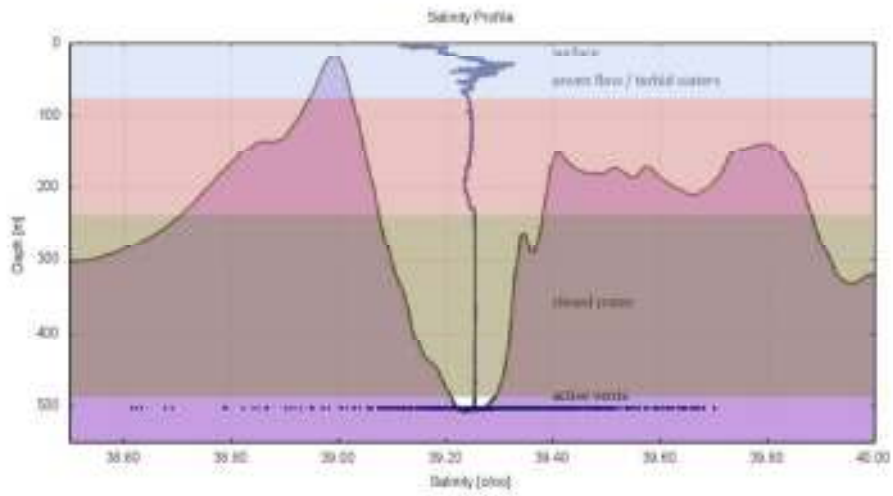


Fig. 5.50 Vertical profile Depth-Salinity; Four distinct zones inside the cone(1: 0-80 m, 2: 80-230 m, 3: 230-497 m, 4:497 m504m)

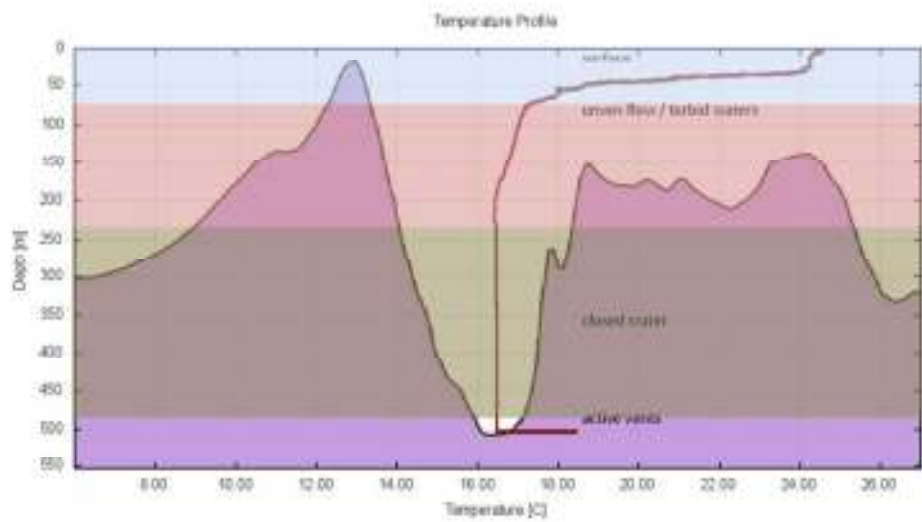


Fig.5.51 Vertical profile Depth-Temperature; Four distinct zones in the cone (1: 0-80 m, 2: 80-230 m, 3: 230-497 m, 4:497 m504m)

## **5.6 GENERAL REMARKS**

On 31/7/2010 the measurements were conducted inside the crater of Kolumbo and specifically over the hydrothermal vent field. The graphic 5.6 (14:00-15:00) is a surface-to-bottom profile. The overall variation of the parameter with depth shows that at surface the values are normal (Stewart, 2008), while a variation is observed as the dive goes deeper. In figures 5.49, 5.50, 5.51 four distinct zones of the cone can be identified. The first one extends from the surface to ~80 m. The predominant conditions are those of the open sea (Stewart, 2008). The second part extends from 80 m to about 230 m. At that point, turbulence is observed due to moving masses of water that hit the crater wall at the NNW part. The turbulence causes small anomalies in the parameter's values. At the third part, we enter the closed caldera from 230 m to approximately 495 m where salinity, conductivity and temperature values are stable, while sound velocity increases proportionally with the depth. The mean value of salinity inside the crater is 39.2528‰ (average between depths 250-400), which is higher than Mean Mediterranean Salinity ~39‰ (Millero, 1996). The fourth part of the morphology correlated with the variation of the physicochemical parameters, is from 495 m to about 504 m where active hydrothermal vents exist. At that point there is a simultaneous steep increase of all the parameter's values.

For the rest of the day the measurements were performed right over the hydrothermal vents on the crater floor. The anomalies of the parameters values observed are due to the hydrothermal activity that is taking place at the location. Salinity's value is higher than the mean value inside the crater (39.2528‰) as a result of hydrothermal activity. The highest measured value of salinity is 40.20‰ which is an increase of 5%. This is an immense change of salinity that can only be explained by the hydrothermal activity. Temperature values show similar behavior. Inside the cone the values remain stable while over at the depth of 500-504 m there is an increase of approximately 4 °C. The Temperature sensor is a few meters (4-5 m) far from the vents so the temperature value is not as high as it is in the vent (220 °C). Salinity is correlated with conductivity, which is expected as salinity is measured by conductivity. (Millero, 1996). The plumes are depicted in the graphics as steep increases (anomalies) of temperature, salinity and conductivity. This is a strong evidence of hydrothermal activity, because, otherwise values should have been stable at that depth. That is an

indicator of material flushing in. Time-series indicate that hydrothermal activity takes place during one hour.

On 29/7/10 the vessel carried out the measurements at the volcanic cone 3 (see Fig. 2.9) which is a symmetric, circular shaped cone NE of Kolumbo, with a presence of crater at a depth of 350 m. At volcanic cone 3 the conditions are the same as we expect in the open sea. That means that normal distributions of the parameters are observed something that suggests that there is no activity present at the cones. The highest summit of the cone is at 115 m and the deepest is at the depth of 235 m. The strongest evidence of no hydrothermal activity is that there is no simultaneous increase of salinity and temperature.

On 1/8/10 the vessel carried out the research at the volcanic cone 11, which is a cone with steep slopes and absence of crater at a depth of 415 m. The CTD profiles are similar to VC3. No anomalies have been observed in any of the nineteen (19) cones NE of Kolumbo (see Fig. 2.9).

On 03/10/10 the vessel carried out measurements in the crater of Kolumbo and the results indicate that hydrothermal activity is still present inside the crater. Salinity and temperature increase in parallel with depth and the plumes are perceived over the vents as the anomalies on the graphics at depths around 500m (*See Fig.5.42, 5.43*). In addition, conductivity is correlated with salinity which is expectable as Millero (1996) has mentioned.

During cruise NA014, E/V Nautilus was at the area of Kolumbo volcano from 01/09/2011 to 04/09/2011, and the measurements conducted on the northern part of the hydrothermal vent field where the vents do not discharge hydrothermal fluids. The operation revealed that there is a small variation, but not as steep as above the central active hydrothermal field. Thus, there is a layer of sea water at the crater floor where there is a small variation of the values due to the diffuse flow.

## 5.7 IN COMPARISON WITH OTHER HYDROTHERMAL VENT FIELDS

The hydrothermal vent field in the crater floor of Kolumbo volcano is a natural laboratory for CO<sub>2</sub> degassing and ocean acidification comprehension (Brewer et al., 2013).

Kolumbo's hydrothermal vent field uniqueness attributed to shallow depth, large amounts of released CO<sub>2</sub> gas and special morphology.

Milos, an island in the middle of the Hellenic Volcanic Arc with some 35 km<sup>2</sup> of geothermally active seabed (Dando et al., 1999; Dando et al., 1995), is one of the best-studied hydrothermal areas in the Aegean. Milos has heterogeneously scattered strongly degassing vents and most probably concentrated at intensively fractured regions. South of Milos two different plumes were found. The plume to the SW is characterized by slightly reduced pH and salinity, contrary to the Kolumbo's field, which has higher salinity. The second one is a bottom plume of water enriched in methane, 10-30 m above the seabed. Kolumbo's main gases are CO<sub>2</sub> (Carey et al., 2013a, 2013b) and it has very low concentrations of methane and other gases. Even though the Milos vents are shallower than Kolumbo's (70-100m depth) they lay on the seafloor and not in a closed volcano cone, thus there is no gas accumulation as in Kolumbo. Additionally, epifaunal diversity is particularly high with over 200 species recorded at the shallow Milos vents (Dando et al., 1999) contrary to the Kolumbo's lack of macrofauna (Kilias et al., 2013).

Sea-floor operations between 1996 and 2005 probed hydrothermal activity in Brothers Volcano along the Kermadec Arc in New Zealand (Baker et al., 2012). Compared with Kolumbo the active chimneys lie deeper and are more in number. The results showed some 100 active or inactive chimneys in depths of 1545 and 1690 m. Chimneys occur on the crater walls and on the cones; sulfur chimneys are scattered among mounds of native sulfur as in Kolumbo. Venting seems exclusively low-temperature except for a single white smoker (122° C). High temperature fluids contain dissolved metals that precipitate immediately as metal sulfides or gradually as oxyhydroxides upon mixing with seawater, creating a sensitive indicator of hydrothermal emissions (Baker et al., 2012).

Compared to Lake Nyos and Monoon in Cameroon, many similarities in comparison with Kolumbo are detected. At Lake Nyos, CO<sub>2</sub> still accumulates below 180 m depth and

at Lake Monoon CO<sub>2</sub> is present below a depth of 60 m, only 25 m below the saturation depth. The diffusion of gas bubbles increases the density of the ambient water. Surveys in Lake Nyos showed that temperature and conductivity profiles have a large decrease in the epilimnion, with limited change at mid-depths and a significant increase towards the lake bottom. That is similar to Kolumbo's conditions even though the hydrothermal vents are in greater depth. pH values decrease greatly from high surface values (pH>8) to pH 5.4 at a depth of 45 m. Below 140 m values stay almost constant at pH 5.2 and present a minimum close to pH 5.0 at depths between 190 and 200 m following to a sharp rise toward the bottom to pH>5.2. That is a difference between Nyos and Kolumbo and that may happen due to the mixing of low pH bottom water with relatively high pH pore water in contact with sediments rich in clay minerals (Kusakabe et al., 2000).

The Mid-Atlantic Ridge is part of a system of slow-spreading mid-ocean ridges that constitute about 40% of the global ridge length (Baker and German, 2004). In South Atlantic the strongest plumes consist of methane together with particle helium, hydrogen and iron at a depth of about 3 km (Keir et al., 2008).

On the Mariana and Kermadec arcs, which are the most completely surveyed, hydrothermal plumes have been found above one-third of the submarine volcanoes (Hannington et al., 2005; de Ronde et al., 2003). The nature of the hydrothermal activity responsible for all of the plumes is not yet well characterized. Some are related to high-temperature hydrothermal venting and black smoker activity (e.g., 3 of the 12 plumes on the Mariana arc) unlike Kolumbo where no black smokers occur, but many appear to be due to passive degassing or quiescent eruptions rather than high temperature hydrothermal activity (Hannington et al. 2005; Massoth et al., 2003).

## 5.8 FUTURE WORK

CO<sub>2</sub> is the signature molecule of 21<sup>st</sup> century and detailed knowledge of its geochemistry is a requirement for scientists. Concerns that CO<sub>2</sub> emissions contribute to climate change makes CO<sub>2</sub> a subject of high importance. Hydrothermal vent fields are a significant source of CO<sub>2</sub> in the environment and their study is necessary for the comprehension of their processes. CO<sub>2</sub> discharge affects several parameters in water column and is the main reason of ocean acidification. Continuing detection and measurements of the hydrothermal vent field processes are indispensable to manage future hazards.

Sea currents effect on CO<sub>2</sub> discharge must be appreciated because of their significant effect on hydrothermal vents that lie in the open sea and not within a volcano cone.

## REFERENCES

- Alexandri M.**, Papanikolaou D., Nomikou P., Ballas D., (2001). Geological structure of the Myrtoon Basin (Aegean Sea) based on swath bathymetry, 36<sup>th</sup> Ciesm Congress Proceedings, Vol. 36, Monte Carlo
- Alexandri M.**, Papanikolaou D. & Nomikou, P. (2003). Santorini volcanic field - new insights based on swath bathymetry. Abstracts IUGG, 30 June-11July 2003, Sapporo, Japan.
- Aliani S.**, Bortoluzzi G., Caramanna G., Raffa F. (2010): Seawater dynamics and environmental settings after November 2002 gas eruption off Bottaro (Panarea, Aeolian Islands, Mediterranean Sea). *Continental Shelf Research*, 30, 1338-1348.
- Baker E.T.**, German C.R., Elderfield H. (1995): Hydrothermal plumes over spreading-center axes: Global distributions and geological inferences. *Sea floor Hydrothermal Systems: Physical, Chemical, Biological, and Geological Interactions*, Geophys. Monogr. Ser., 91, pp. 47-71, AGU
- Baker, T.B.**, & German, C.R. (2004): On the Global Distribution of Hydrothermal Vent Fields. *American Geophysical Union*. 245-266.
- Baker, E.T.**, Walker, S.L., Embley, R.W., de Ronde, C.E.J. (2012): High-Resolution Hydrothermal Mapping of Brothers Caldera, Kermadec Arc. *Society of Economic Geologists*. V 107, pp 1583-1593
- Bejelou K.**, (2013), Tectonic Analysis of the volcanic field around the Kolumbo Volcano, Master thesis, University of Athens
- Bell K.L.C.**, Nomikou P., Carey S., Stathopoulou E., Polymenakou P., Godelitsas A., Roman C. and Parks M. (2012): Continued Exploration of the Santorini Volcanic Field and Cretan Basin, Aegean Sea. In K.L.C. Bell, K. Elliott, C. Martinez and S.A. Fuller eds 2012. *New Frontiers in Ocean Exploration: The E/V Nautilus and NOAA Ship Okeanos Explorer 2011 Field Season*. *Oceanography* 25.1:30-31, supplement, 68pp.
- Camilli R.**, D. Sakellariou, B. Foley, C. Anagnostou, A. Malios, B. Bingham, R. Eustice, J. Goudreau, K. Katsaros (2007). Investigation of hydrothermal vents in the Aegean Sea using an integrated mass spectrometer and acoustic navigation system onboard a human occupied submersible. In: *Proceedings 38th CIESM, Congress, 9-13 April 2007, Istanbul*
- Cantner K.**, Carey S, Sigurdsson H, Vougioukalakis G, Nomikou P, Roman C, Bell K, Alexandri M (2010) re-eruption pressure, temperature and volatile content of rhyolite magma from the 1650 AD eruption of Kolumbo submarine volcano, Greece. In: *Fall Meeting, AGU, San Francisco*, pp 13–17
- Cantner K.**, Carey S., Nomikou P. (2014) Volcanological and petrological analysis of the 1650 AD eruption of Kolumbo submarine volcano, Greece. *Journal of Volcanological and Geothermal Research*
- Carey, S.N.**, (2000). Volcaniclastic sedimentation around island arcs. In: Sigurdsson, H., Houghton, B., McNutt, S.R., Rymer, H., Stix, J. (Eds.), *Encyclopedia of Volcanoes*. Academic Press, San Diego, pp. 627–642.

**Carey S.**, Bell KLC, Nomikou P, Vougioukalakis G, Roman C, Cantner K, Bejelou K, Bourboulis M, Martin Fero J (2011) Exploration of the Kolumbo volcanic rift zone. "New frontiers in ocean exploration" The E/V Nautilus 2010 field season. March 2011, *Oceanography*, Vol 24, no 1, supplement, pp 24-25.

**Carey S.**, Nomikou P., Croff Bell K., Lilley M., Lupton J., Roman C., Stathopoulou E., Bejelou K., Ballard R. (2013a): CO<sub>2</sub> Degassing from Hydrothermal Vents at Kolumbo Submarine Volcano, Greece and the Accumulation of Acidic Crater Water. *Geology*. September 2013, Volume 41, Number 9, 1035-1038

**Carey, S.**, Nomikou, P., Croff Bell, K., and Ballard, D. (2013b): Exploration of the Santorini volcanic group, southern Aegean Sea: *Oceanography* (Washington, D.C.), v. 26, no. 1, supplement, p. 44-49

**Carritt D.E.**, and J.H. Carpenter. 1959. The composition of sea water and the salinity-chlorinity-density problems. National Academy of Sciences-National Research Council, Report 600: 67-86.

**Dando, P. R.**, Hughes, I. A., Leahy, Y., Niven, S. J., Taylor, L. J., and Smith, C., Gas venting rates from submarine hydrothermal areas around the island of Milos, Hellenic Volcanic Arc. *Cont. Shelf Res.*, 15, 913-929, 1995a.

**Dando, P.R.**, Aliani, S., Arab, H., Bianchi, C.N., Brehmer, M., Cocito, S., Fowler, S.W., Gundersen, J., Hooper, L.E., Kolbl, R., Kuever, J., Linke, P., Makropoulos, K.C., Meloni, R., Miquel, J.-C., Morri, C., Muller, S., Robinson, C., Schlesner, H., Sievert, S., Stohr, R., Stuben, D., Thomm, M., Varnavas, S.P., and Ziebis, W. (1999): Hydrothermal studies in the Aegean Sea. *Phys. Chem. Earth (B)*, Vol. 25, No. 1, pp 1-8.

**Dittmar W.** (1884). Report on researches into the composition of ocean water, collected by the HMS Challenger. *Challenger Reports, Physics and Chemistry* 1.

**Dushaw B.D., P.F.** Worcester, B.D. Cornuelle, and B.M. Howe. (1993). On equations for the speed of sound in sea water. *Journal of the Acoustical Society of America* 93: 255-275.

**Druitt, T.H.**, Mellors, R.A., Pyle, D.M., Sparks, R.S.J., (1989). Explosive volcanism on Santorini, Greece. *Geological Magazine* vol. 2 (126), 95-126.

**Druitt, T.H.** et al. (1999). Santorini Volcano. *Geological Society Memoir* no. 19. The Geological Society of London.

**Dohiaritis** (1947) Fiction anthology of folk. vol A, Ranou Publications, Athens

**Dominey-Howes D.T.M.**, Papadopoulos G.A, Dawson A.G (2000) Geological and historical investigation of the 1650 Mt. Columbo (Thera Island) eruption and tsunami, Aegean Sea, Greece. *Nat Hazards* 21(1): 83-96

**Edwards, K.J.** et al. (2011) Ultra-diffuse hydrothermal venting supports Fe-oxidizing bacteria and massive uranium deposition at 5000 m off Hawaii. *ISME J.* 5, 1748-1758

**E/V Nautilus**, expedition NA007 & NA011, report, 2011

**E/V Nautilus**, expedition NA014 report, 2012

**Fouque, F.**, (1879). Santorin et ses Iruptions. Masson et Cie, Paris.

**Fouquet, Y.** et al.(1993) Metallogenesis in back-arc environments: the Lau Basin example. *Economic Geology* 88, 2154-2181.

**Friedrich, W.**, (2000). Fire in the Sea, The Santorini Volcano: Natural History and the Legend of Atlantis. Cambridge University Press, Cambridge

**Friedrich, W.**, Kromer B., Friedrich M., Heinemeier J., Pfeiffer T., Talamo S., (2006): Santorini Eruption Radiocarbon Dated to 1627-1600 B.C., *Science*, Vol. 312 no. 5773, p 548.

**Forster, M.A.** & Lister, G.S. (1999) Detachment faults in the Aegean core complex of Ios, Cyclades, Greece. In: Exhumation Processes: Normal Faulting, Ductile Flow and Erosion, (eds, Ring, U., Brandon, M.T., Lister, G.S., & Willett, S.D.). *Geol. Soc. London Spec. Publ.* 154, 305-324.

**Fytikas, M.**, Guliani, O., Innocenti, F., Marinelli, G., Mazzuoli, R., (1976). Geochronological data on recent magmatism of the Aegean sea. *Tectonophysics* 31, 29–34.

**German, C.R.**, Baker E.T., & Klinkhammer G. (1995): The regional setting of hydrothermal activity. *Hydrothermal Vents and processes*. *Geol. Soc. Spec., Pub. No 87*, 3-15.

**Hannington, M.** et al. (2001) First observations of high-temperature submarine hydrothermal vents and massive anhydrite deposits off the north coast of Iceland. *Marine Geology* 177, 199-220.

**Hannington, M.**, de Ronde, C., Petersen., S. (2005): Sea-Floor Tectonics and Submarine Hydrothermal Systems. *Society of Economic Geologists. 100<sup>th</sup> Anniversary Volume*, pp 111-141.

**Harrison D.E.** and N.K. Larkin (1998). El Nino-Southern Oscillation sea surface temperature and wind anomalies, 1946–1993. *Reviews of Geophysics* 36 (3): 353–399.

**Holden, J.F.**, Breier, J.A., Rogers, K.L., Schulte, M.D., Toner, B.M. (2012) Biogeochemical processes at hydrothermal vents: Microbes and minerals, bioenergetics, and carbon fluxes. *Oceanography* 25(1), 196-208.

**JPOTS Joint Panel on Oceanographic Tables and Standards.** (1981). The practical salinity scale 1978 and the international equation of state of seawater 1980. Paris: unesco Technical Papers in Marine Science 36: 25.

**Keir R.,** Schmale O., Walter M., Sultenfuss,J., Seifert,R., Rhein,M., (2008) .Fluxan dispersion of gases from the “Drachenschlund’ ’hydrothermal vent at 81180S, 131300W ontheMid-AtlanticRidge.EarthPlanet.Sci.Lett.270, 338–348.

**Kilias, S.,** Nomikou, P., Papanikolaou, D., Polymenakou, P.N., Godelitsas, A., Argyraki, A., Carey, S., Gamaletsos, P., Mertzimekis, T.J., Stathopoulou, E., Goettlicher, J., Steininger, R., Bejelou, K., Livanos, I., Christakis, C., Croff Bell, K., & Scoullou, M. (2013). New insights into hydrothermal vent processes in the unique shallow-submarine arc-volcano, Kolumbo (Santorini), Greece. *SCIENTIFIC REPORTS*

**Kusakabe, M.,** Tanyileke, G.Z., McCord, S.A., Schladow, S.G. (2000): Recent pH and CO<sub>2</sub> profiles at Lakes Nyos and Monoun, Cameroon: implications for the degassing strategy and its numerical simulation. *Journal of Volcanology and Geothermal Research* 97, 241-260.

**Le Pichon, X. & Angelier, J.** (1979) The Hellenic Arc and Trench system: A key to the neotectonic evolution of the Eastern Mediterranean area. *Tectonophysics* 60, 1–42

**Lewis E.L.** (1980). The Practical Salinity Scale 1978 and its antecedents. *IEEE Journal of Oceanic Engineering* oe-5: 3–8.

**MacKenzie K.V.** (1981). Nine-term equation for sound speed in the ocean. *Journal of the Acoustical Society of America* 70: 807–812.

**Millero F.J.** (1996). *Chemical Oceanography* (2nd ed). New York, CRC Press.

**Millero F. J.,** R. Feistel, et al. (2008). The composition of Standard Seawater and the definition of the Reference-Composition Salinity Scale. *Deep Sea Research Part I: Oceanographic Research Papers* 55 (1): 50–72.

**Massoth, G.J.,** de Ronde, C.E.J., Lupton, J.E., Feely, R.A., Baker, E.T., Lebon, G.T., and Maenner, S.M., (2003) Chemically rich and diverse submarine hydrothermal plumes of the southern Kermadec volcanic arc (New Zealand): *Geological Society of London Special Publication* 219, p. 119–139.

**Munk W.,** P. Worcester, and C. Wunsch. (1995). *Ocean Acoustic Tomography*. Cambridge: University Press.

**Nomikou P.** (2003): Santorini and Nisyros: Similarities and differences between the two calderas of the modern Aegean Volcanic Arc. *CIESM Workshop on “Human records of recent geological evolution in the Mediterranean Basin-historical and archaeological evidence” Santorini 22-25 October 2003, Greece. CIESM Workshop Monographs* n24, p.103-108.

**Nomikou, P.,** Papanikolaou, D., Alexandri, S., Ballas, D., (2004). New insights on the Kos– Nisyros volcanic field from the morphotectonic analysis of the swath bathymetric map. *Rapp. Comm. Int. Mer. Medit.*, 37, p. 60.

**Nomikou, P. &** Papanikolaou, D. (2010): The morphotectonic structure of Kos- Nisyros-Tilos volcanic area based on onshore and off shore data. – Proc. XIX Congr. Carpathian-Balkan Geol. Assoc., Thessaloniki, Greece, 23–26 September 2010, spec. vol. 99: 557–564.

**Nomikou P.,** Carey S., Papanikolaou D., Croff Bell K., Sakellariou D., Alexandri M., Bejelou K. (2012a): Submarine Volcanoes of the Kolumbo volcanic zone NE of Santorini Caldera, Greece. *Global and Planetary Change* 90-91 135-151.

**Nomikou P.,** Carey S., Croff Bell K., Papanikolaou D., Bejelou K., Cantner K., Sakellariou D., Perros I. (2012b): Tsunami Hazard Risk of a future volcanic eruption of Kolumbo submarine volcano, NE of Santorini Caldera, Greece: *Natural Hazards*.

**Nomikou P.,** Papanikolaou D., Alexandri M., Sakellariou D., Rousakis G. (2013a): Submarine volcanoes along the Aegean Volcanic Arc. *Tectonophysics* 507-508, 123-146.

**Nomikou P.,** Carey S., Croff Bell K.,L., Papanikolaou D., Bejelou K., Alexandri M., Cantner K., Martin J. F. (2013b): Morphological analysis and related volcanic features of the Kolumbo submarine volcanic chain (NE of Santorini Island, Aegean Volcanic Arc), *Zeitschrift für Geomorphologie* Vol. 57 , Suppl. 3, 029-047

**Ono K.,** Ohshima K.I., Kono T., Katsumata K., Yasuda I., Wakatsuchi M., (2013): Distribution of vertical diffusivity in the Bussol' Strait: A mixing hot spot in the North Pacific, *Deep-Sea Research I*, 79, 62-73

**Papanikolaou, D.,** Lykousis, V., Chronis, G., Pavlakis, P. (1988). A comparative study of neotectonic basins across the Hellenic Arc: The Messiniakos, Argolikos, Saronikos and Southern Evoikos Gulfs. *Basin Research*, 1/3, 167-176.

**Papanikolaou D.,** Chronis G., Lykousis V., Pavlakis P., Roussakis G., Siskakis D., (1989): Submarine Neotectonic map of Saronic Gulf, Scale 1/100.000, EPPO, HCMR, University of Athens.

**Papanikolaou, D.** (1993). Geotectonic evolution of the Aegean. *Bull. Geol. Soc. Greece*, XXVII, 33-48.

**Papanikolaou D. &** Nomikou P. (2001): Tectonic structure and volcanic centres at the eastern edge of the Aegean Volcanic Arc around Nisyros Island. *Bull. Geol. Soc. of Greece*, Vol. XXXIV/1, 289-296.

**Papanikolaou, D. J. &** Royden, L. H. (2007): Disruption of the Hellenic arc: Late Miocene extensional detachment faults and steep Pliocene-Quaternary normal faults or what happened at Corinth? – *Tectonics* 26: TC5003, doi:10.1029/2006TC002007.

**Papastamatiou, I.** (1958). The age of Crystalline Limestones of Thira. *Bull. Geol. Soc. Greece* 3 (1), 104-113.

**Pavlakis, P.,** Lykousis, V, Papanikolaou, D, Chronis, G. (1990). Discovery of a new submarine volcano in the western Saronic Gulf: The Paphsanias Volcano. *Bulletin of the Geological Society of Greece* 24, 59–70

**Phillips, B.,** Newman, J., Gregory, T., 2011. E/V Nautilus vehicles. “New Frontiers in Ocean Exploration” The E/V Nautilus 2010 Field Season. March 2011: *Oceanography*, Vol.24, No. 1, Supplement, p. 9.

**Pyle D.M.,** (1990). New estimates for the volume of the Minoan eruption. Pp. 113-121. In: Hardy D.A et al. (eds), *Thera and the Aegean World III vol.2 (Earth Sciences)*, The Thera Foundation, London.

**Pyle D.M. & Elliott J.R.** (2006) Quantitative morphology, recent evolution, and future activity of the Kameni Islands volcano, Santorini, Greece. *Geosphere* 2 (5), pages 253-268, doi:10.1130/GES00028.1

**Reynolds R.W.,** and T.M. Smith. 1995. A high-resolution global sea surface climatology. *Journal of Climate* 8 (6): 1571–1583.

**Roman, C. et al.** The development of high-resolution seafloor mapping techniques: In Bell, K.L.C., Elliott, K., Martinez, C. & Fuller, S.A. eds 2012. *New Frontiers in Ocean Exploration: The E/V Nautilus and NOAA Ship Okeanos Explorer 2011 Field Season.* *Oceanography* 25(1), 42-45 (2012).

**Ronde, C.E.J.,** Massoth, G.J., Baker, E.T., and Lupton, J.E., 2003, Submarine hydrothermal venting related to volcanic arcs: *Society of Economic Geologists Special Publication* 10, p. 91–109.

**Royden, L.H., & Papanikolaou, D.J.** (2011): Slab segmentation and late Cenozoic disruption of the Hellenic arc. *Geochemistry Geophysics Geosystems*, Volume 12, Number 3, 1525-2027

**Sakellariou D.,** Sigurdsson H., Alexandri M., Carey S., Rousakis G., Nomikou P., Georgiou P. and Ballas D. (2010): Active tectonics in the Hellenic Volcanic Arc: the Kolumbo submarine volcanic zone. *Bull. Geol. Soc. of Greece*, Vol. XLIII/2, 1056-1063.

**Schmid M.,** Halbwachs M., Wuest A. (2006): Simulation of CO<sub>2</sub> concentrations, temperature, and stratification in Lake Nyos for different degassing scenarios, *Geochemistry Geophysics Geosystems*, Volume 7, Number 6, 1525-2027

**Searcy, C.,** Dean, K., Stringer, W., 1998, PUFF: A Lagrangian Trajectory Volcanic Ash Tracking Model, *Journal of Volcanology and Geothermal Research* (80) 1-16

**Sigurdsson, H.,** S. Carey, M. Alexandri, G. Vougioukalakis, K. L. Croff, C. Roman, D. Sakellariou, C. Anagnostou, G. Rousakis, C. Ioakim, A. Gogou, D. Ballas, T. Misaridis, and

P. Nomikou (2006). Marine investigations of Greece's Santorini volcanic field. EOS, 87(34):337, 342.

**Southam, G.** & Saunders, J.A. (2005) The geomicrobiology of ore deposits. Economic Geology 100, 1067-1084 .

**Stewart R.H.**, (2008): Introduction to Physical Oceanography, Texas A & M University, September 2008 Edition

**Stoffers, P. et al.** (2006) Submarine volcanoes and high-temperature hydrothermal venting on the Tonga arc, southwest Pacific. Geology 34, 453-456.

**Sverdrup H.U.**, M.W. Johnson, and R.H. Fleming. (1942). The Oceans: Their Physics, Chemistry, and General Biology. Englewood Cliffs, New Jersey: Prentice-Hall

**Tataris, A.** (1965). The Metamorphic basement (Hocene) of Thira. Bull. Geol. Soc. Greece 6, 232-238.

**Tivey, M.** (2007) Generation of seafloor hydrothermal vent fluids and associated mineral deposits. Oceanography 20, 50-65.

**Varnavas, S.P.**, Cronan, D.S., (2005). Submarine hydrothermal activity off Santorini and Milos in the Central Hellenic Volcanic Arc: A synthesis. Chemical Geology 224 (1-3), 40-54.

**Walter M.**, Mertens C., Stober U., German C.R. Yoerger D.R., Sultenfub J., Rhein M., Melchert B., Baker E.T. (2010): Rapid dispersal of a hydrothermal plume by turbulent mixing, Deep-Sea Research I, 57, 931-945.

**Wilson W.D.** (1960). Equation for the speed of sound in sea water. Journal of the Acoustical Society of America 32 (10): 1357.

## WEBPAGES

- <http://www.whoi.edu/main/topic/hydrothermal-vents>
- <http://oceanservice.noaa.gov/facts/vents.html>
- [http://www.hcmr.gr/gr/listview3\\_el.php?id=1051](http://www.hcmr.gr/gr/listview3_el.php?id=1051)
- <http://www.pmel.noaa.gov/eoi/PlumeStudies/WhatIsACTD/CTDMethods.html>
- <http://www.seabird.com/products/CTDProfilers.htm>